School of Physics and Astronomy

UNIVERSITY OF LONDON

Microstructure of Fe-based and NiFe nanowires encapsulated by multiwalled carbon nanotube radial structures

Submitted in partial fulfilment
of the requirements of the Degree of
Doctor of Philosophy

Muhammad Ibrar
PhD Student

Supervisors: Mark Baxendale and David Dunstan

Abstract

The crystalline iron-based nanowires encapsulated by multiwalled carbon nanotubes have been the subject of numerous studies owing to the range of potential applications. The presence of α-Fe (bcc)/γ-Fe(fcc) junctions offers the possibility of exploitation of the exchange bias effect, an interfacial magnetic phenomenon that plays a major role in magnetocaloric cooling, spintronic and high-density magnetic storage devices. This work is concerned with the synthesis and microstructural characterization of Fe-based and NiFe nanowires encapsulated by multiwall carbon nanotube radial structures. The known attributes of these structures are well matched to the magnetocaloric application. The primary aim of this work was to determine the unknown microstructural details of the encapsulated nanowire that are of relevance to the magnetocaloric application (junction types, location and orientation relative to the nanotube axis). The secondary aim was to explore the modification of the synthesis route to promote desirable attributes. This is the first report of α-Fe/γ-Fe sequential junctions and α-Fe/Fe_3C concentric junctions in encapsulated Fe-based nanowires. The presence of α-Fe/γ-Fe junctions was inferred from the observation of α-Fe nanowires terminated by a $\sim$100 nm length γ-Fe crystallites of larger diameter. The α-Fe/Fe_3C junctions exhibit the Bagaryatski orientation relationship: $[110]_{bcc} \| [100]_{orth}$. The degree of substrate roughness was found to be a means of tailoring details of the structure and composition of the encapsulated nanowires. NiFe encapsulated nanowires were found to contain crystallites of α-NiFe, γ-NiFe and Ni_3Fe and the sequential junctions γ-NiFe/Ni_3Fe and α-NiFe/γ-NiFe junctions.

Contents

List of Figures

List of Tables

Statement of orignality

I, Muhammad Ibrar, confirm that the research included within this thesis is my own work or that where it has been carried out in collaboration with, or supported by others, that this is duly acknowledged below and my contribution indicated. Previously published material is also acknowledged below.

I attest that I have exercised reasonable care to ensure that the work is original, and does not to the best of my knowledge break any UK law, infringe any third partys copyright or other Intellectual Property Right, or contain any confidential material.

I accept that the College has the right to use plagiarism detection software to check the electronic version of the thesis.

I confirm that this thesis has not been previously submitted for the award of a degree by this or any other university. The copyright of this thesis rests with the author and no quotation from it or information derived from it may be published without the prior written consent of the author.

.....

Muhammad Ibrar ..... September 22, 2017

The electron microscopy experiments included in this research work were carried out in collaboration with NanoVision Centre Queen Mary University of London and EMAT University of Antwerpen.

Publications

F.S. Boi, R. M. Wilson, G. Mountjoy, M. Ibrar, and M. Baxendale, Boundary layer chemical vapour synthesis of self-organised ferromagnetically filled radial-carbon-nanotube structures, Faraday Discussion, vol. 173, no. 0, pp. 67-77, 2014.

Acknowledgement

This piece of research work would not have been possible without the support of the following institutions and people. I acknowledge the financial support of Queen Mary University of London, United Kingdom, Islamia College Peshawar, Pakistan, and the Higher Education Commission of Pakistan.

I am really grateful to my supervisor Dr. Mark Baxendale whose patience, guidance and support made me able to address the outstanding questions in the field of carbon nanotube science. Not only that, he also introduced me to the interesting science of inside the cylindrical cavity of the carbon nanotubes and kept me motivated. I would like to say thanks to my co-supervisor Professor David Dunstan for his support and encouragement.

I am also thankful to Professor Martin Dove for fruitful discussions on phase transition of the encapsulated phases of iron and Dr. Gavin Mountjoy for useful comments, George Neville for preparing quartz substrates, and Dr. Ken Scott for technical support. Special thanks to Dr. Nadezda V. Tarakina for consistent support in conducting transmission electron microscopy investigations and interpretation, and Dr. Rory M. Wilson for conducting X-ray diffraction experiments and help in data analysis. Also, thanks to Russell Bailey for providing assistance in scanning electron microscopy experiments.

I would like to say thanks to Dr. Mert Kurttepeli, Professor Sara Balls and Professor Gustaaf Van Tendeloo from EMAT, University of Antwerpen for their help and support with conducting HRTEM experiments. Thanks to Dr. Richard Thorogate and Dr. Laura Bovo for help in carrying out the SQUID magnetization measurements at London Centre

for Nanotechnology. I am very thankful to Dr. Filippo S. Boi for helping in synthesis experiments in my first year of PhD and to Dr. Anthony Phillips and Dr. Helen Duncan for helping in Rietveld analysis using GSAS program. Its a great moment would like to thank my friends and fellows Taze Peci, Manting Qiu, Prashantha, Viswanathan Mohandoss, Serena Ada Maugeri, Osman Ersoy, Kemal Keseroglu, Dr. Yuan peng and Dr. Yuan Li.

Many thanks to Dr. Terrance Arter for the software installations and IT support which was really helping to do the work easily, and thanks to John Sullivan and all admin staff of the school. I had a great time with all of them.

Really say thanks and love to my wife Sadia Rehman, my little sweet angels Ammara Affaf and Fatima Affaf. I would also like to say many thanks to Ikram Ullah and his wife for their support while living in London. At the end, I will say thanks to my father and my mother (late) for their continuous support in my education and I would have never been to this point without their consistent efforts.

Chapter 1

Introduction

1.1 Nanowires encapsulated by carbon nanotubes

A carbon nanotube (CNT) is a tubule-like structure of carbon atoms having a diameter in the order of nanometers and length in micrometers. A single-walled nanotube (SWCNT) can be visualized as a rolled-up single graphene sheet (single layer of carbon atoms) to form a hollow cylinder [26], while multiwalled carbon nanotubes (MWCNTs) can be visualized as concentric graphene cylinders of different diameters [27]. Since discovery by Sumio Iijima in 1991 [27], CNTs have extensively been investigated in different fields of fundamental and applied science, owing to their exceptional structural diversity, thermal, elastic, mechanical and electrical properties [28, 29]. The cylindrical cavity of CNT offers a remarkable opportunity for encapsulating nanoscale materials. The possible encapsulation of transition metals Fe, Ni and Co, including their alloys, by weakly diamagnetic MWCNTs advantageously prevents oxidation and mechanical degradation of the encapsulated magnetic nanowire, thus ensuring long-term stability of the metallic core [1, 30–32].

For more than a decade, iron-based nanowires encapsulated by MWCNTs have been intensively investigated by many research groups due to their remarkable structural and magnetic properties [1, 10, 33, 34]. The commonly observed crystalline phases in Fe-

based nanowires are α-Fe (bcc), Fe_3C (orthorhombic), and the unexpected metastable phase γ-Fe (fcc). Much effort has been devoted in realising continuous, single-phase ferromagnetic nanowires and tuning of the magnetic response through the magnetocrystalline and shape anisotropies [33, 35–37]. At the same time, encapsulation of NiFe alloy nanowires has attracted significant interest owing to potential usefulness of the crystalline γ-NiFe (fcc) phase [34, 38, 39]. The γ-NiFe phase due to its low thermal expansion is not only interesting but also showing soft magnetic properties with enhanced saturation magnetization, low coercivity (hysteresis loss) and tunable Curie temperatures render it one of the most promising candidates for near room temperature magnetocaloric refrigeration, microwave absorption and magnetic hyperthermia cancer therapy applications [1, 34, 38, 40].

1.2 Carbon nanotube radial structures

The production of carbon nanotube radial structures using boundary layer chemical vapour synthesis has recently been reported [10]. The microstructural analysis of this particular structure and the nanowires composition distinguish this work from the previously reported work on carbon nanotubes and encapsulated nanowires. A typical example of an individual carbon nanotube radial structure is shown in Figure 1.1 (A), and example of an encapsulated nanowire which is typically continuous for several micrometres is shown in Figure 1.1 (B) [1]. Detail description of boundary layer chemical vapour synthesis and the radial structure formation is provided in Chapter 2 section 2.3.

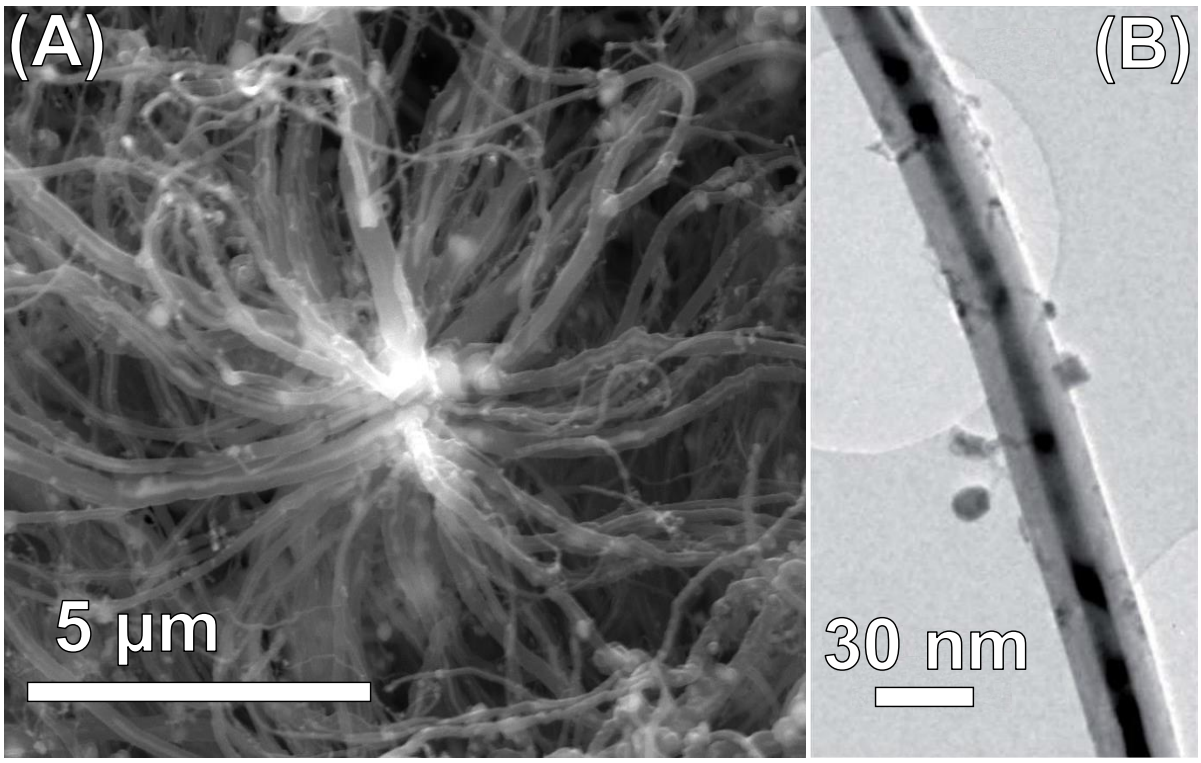

Figure 1.1: Scanning electron micrograph of a typical individual radial structure comprising Fe-based nanowires encapsulated by multiwalled carbon nanotubes. (B) Transmission electron micrograph of an individual encapsulated nanowire typically continuous for several micrometres [1].

1.3 α-Fe/γ-Fe junctions

The spatial distribution of phases in encapsulated Fe-based nanowires may result in the formation of junctions. Junctions between the ferromagnetic phases, α-Fe and Fe_3C, and a possible antiferromagnetic phase of γ-Fe, within a single nanowire offers the possibility of exploitation of the exchange bias effect, an interfacial magnetic phenomenon characterized by sensitivity of the magnetic moment to external field [41]. Its signature, a shifted hysteresis loop, was observed in Fe-based nanowires encapsulated by carbon nanotubes by Prados *et al.*; these authors concluded the exchange coupling between α-Fe/γ-Fe, ferromagnetic/antiferromagnetic junctions [33, 42]. However, a later study attributed the

shifted hysteresis loop to the presence of disordered surface spins in the nanowires [35]. Two types of interfacial arrangement of the junctions relative to the nanotube axis have been identified by these studies: (i) sequential crystallites along the axis of the nanowire, and (ii) concentric cylinders of α-Fe, γ-Fe, and Fe_3C with axes parallel to that of the nanotube [33, 37, 43, 44]. It is important to mention that, the distribution model proposed by Prados *et al.* and Marco *et al.*, which is inferred from Mössbauer spectroscopy and magnetization measurements, comprises α-Fe core surrounded by γ-Fe and finally by a Fe_3C outer layer in contact with the graphitic walls of the nanotube [33, 43]. To the best of our knowledge, no microscopic studies of the junctions between the phases in the encapsulated nanowires have been reported.

The magnetic state of γ-Fe at room temperature is uncertain although an antiferromagnetic state below 100 K was inferred by Prados *et al.* and Marco *et al.* [33, 42, 43]. It is also worth to point out that the magnetic nature of γ-Fe is strongly dependent on its lattice parameter, which can be affected by the dilute carbon alloying [45–47]. Therefore, controlling the γ-Fe lattice parameter is an important factor for the applications where antiferromagnetic γ-Fe is the ultimate requirement. Theoretically, γ-Fe with lattice parameter $a < 3.6$ Å is antiferromagnetic [45]. Surprisingly, reports of the antiferromagnetic state of γ-Fe do not also report the lattice parameter [33, 42, 43].

At standard atmosphere pressure (100 kPa), bulk γ-Fe is stable only in the temperature range 912 °C to 1394 °C [11]. The unexpected presence of γ-Fe in encapsulated nanowires at room temperature has been attributed to the suppression of the $\gamma \rightarrow \alpha$ phase transition by confinement within the highly elastic graphitic walls of the carbon nanotube (elastic modulus *circa* 1 TPa) [33, 43, 48, 49]. Using Gibbs free energy arguments, Kim *et al.* suggested the presence of γ-Fe is due to a 1.5 GPa pressure exerted on the nanowire by the nanotube resulting from a 9% volume expansion that accompanies the $\gamma \rightarrow \alpha$ phase transition in iron [49, 50]. The presence of this internal pressure has been assumed

without experimental justification [14, 15].

1.4 Motivation

Growing energy demands and threat to the global environment is a vital challenge to cope with. The waste disposal of chlorofluorocarbon (CFC) and freon refrigerators, based on air to air vapor-compression cooling systems are certainly one of the major causes of the environmental pollution and particularly ozone degradation [51–53]. Moreover, the solid phase magnetic refrigerant material is expected to be highly environment-friendly, rendering better energy efficiency to the refrigeration systems with producing much better cooling [51–53]. Therefore, the search for economical nanoscale materials with promising structural attributes and potential magnetic features for exhibiting magnetocaloric properties near room temperature is essential. This will enable the current refrigeration systems to switch toward a new magnetic refrigeration technology. Materials exhibiting magnetocaloric properties are mainly concerned with the thermal response (heating or cooling) to an applied varying magnetic field, which results due to the ordering of magnetic moments within the material with the help of an external magnetic field [51–53]. Figure 1.2 shows a schematic diagram of the magnetic refrigeration cycle showing the heat-transfer from the heat load to its surroundings based on the adiabatic demagnetization phenomenon. In this phenomenon the ordering of magnetic domains causes a decrease in the magnetic entropy which is a component of the total entropy [54]. This decrease in magnetic component is compensated by an increase in the other components of the total entropy to produce magnetic cooling. Detailed discussion on thermodynamics of magnetocaloric refrigeration is presented in Ref. [54].

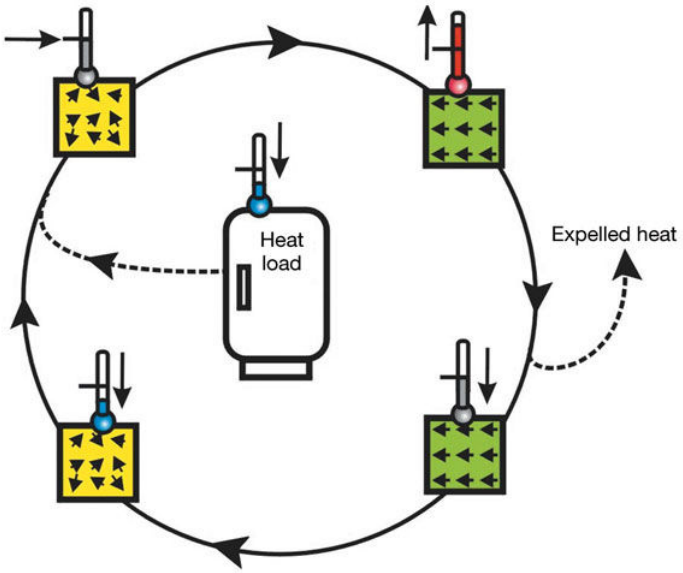

Figure 1.2: Schematic diagram of a magnetic-refrigeration cycle, which transfers heat from the heat load to its surroundings. Yellow and green depict the magnetic material in low and high magnetic fields, respectively. Initially randomly oriented magnetic moments are aligned by a magnetic field, resulting in heating of the magnetic material. This heat is then removed from the material to its surroundings by a heat-transfer medium. On removing the field, the magnetic moments randomize, which leads to cooling of the magnetic material below the ambient temperature. Heat from the system to be cooled can then be extracted using a heat-transfer medium. Depending on the operating temperature, the heat-transfer medium may be water (with antifreeze) or air, and for very low temperatures, helium [2].

Until now, Gadolinium (Gd) and its composites are the best magnetic refrigerant materials, which exhibit magnetocaloric properties near room temperature [51–53, 55]. The magnetic and thermodynamics Gd-based composites are influenced by the crystal structure of these materials [51]. The significantly high cost of these materials offer hindrance to switch toward new refrigeration technology on commercial basis.

Our interest in studying encapsulated Fe-based and NiFe nanowires was motivated due to the fact that these nanoscale materials are the most economical and our synthesis method has the up-scaling potential to easily produce several grams of these materials. Furthermore, the motivation for the radial structures synthesis and their microstructural characterization is rooted in the inherent tendency of micrometer long encapsulated Fe-

based nanowires to have the spatial distribution of α-Fe/γ-Fe junctions. These junctions are promising for the exchange coupling between the two phases α-Fe and γ-Fe when γ-Fe is in the antiferromagnetic state [33, 42, 43]. Therefore, they have potential usefulness for demonstrating novel functionalities at the nanoscale, which either of the individual iron phases is unable to exhibit. In addition, high density of α-Fe (ferromagnetic)/γ-Fe (antiferromagnetic) junctions are important to observe an obvious shift in hysteresis loop referred to as exchange bias effect (Figure 1.3).

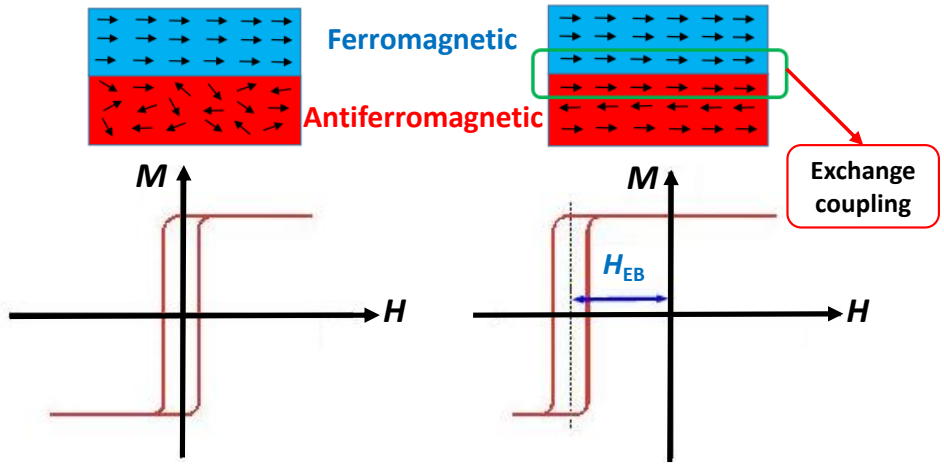

Figure 1.3: A schematic diagram showing a horizontal shift of hysteresis loop due to exchange coupling between ferromagnetic and antiferromagnetic spins at the junction (interface) [3].

The observation of this phenomenon is reported below 100 K indicating the existence of antiferromagnetic γ-Fe at very low temperatures [33, 42, 43]. Room temperature γ-Fe in the antiferromagnetic state can make this phenomenon possible to occur at room temperature. The radial morphology facilitates the access to individually encapsulated nanowire and also provides sufficient surface area for heat dissipation.

High density of α-Fe/γ-Fe junctions is the mean to increase the sensitivity of the moment to the external magnetic field which could also be useful for the magnetocaloric and microwave absorption applications. In addition, the magnetic properties of the encapsulated junctions will be helpful in understanding the implications and origin of magnetic

anisotropies in exchange bias effect.

Previously, non-encapsulated NiFe alloy nanoparticles have been identified to exhibit low curie temperature and its usefulness for magnetocaloric refrigeration application has been envisaged [40]. The magnetic properties of NiFe nanowires encapsulated by MWCNTs can be tuned by relative concentration of Ni into Fe [56]. Concentration dependent tunability features of NiFe nanowires can make this nanoscale material promising for microwave absorption at a wide spread frequency.

1.5 Aim

The primary aim of this work was to determine the unknown microstructural details of the encapsulated Fe-based and NiFe nanowires that of relevance to the magnetocaloric application. These details include; spatial distribution of encapsulated phases, location and junction types, and magnetic state of γ-Fe and accurate measurement of its lattice parameter. The secondary aim was to explore modification of the synthesis route to promote the desirable attributes of the radial structures.

1.6 Thesis outline

This thesis is organized as follows:

Chapter 1 is an introduction to the overall content of this thesis.

Chapter 2 is a literature review of the synthesis methods, properties and applications of Fe-based and NiFe nanowires encapsulated by multiwalled carbon nanotube structures.

Chapter 3 is a brief description of the experimental methods, techniques, physical principles and chemicals used in this study. The first part of this chapter focuses on the

boundary layer chemical vapor synthesis, the second part on the details of the characterization techniques used in this study.

Chapter 4 contains the experimental results and discussion. This section focuses on attempts made to achieving high content γ-Fe and the subsequent observation of α-Fe/γ-Fe junctions contained in Fe-based nanowires encapsulated by multiwalled carbon nanotube radial structures. The role of substrate roughness in boundary layer synthesis is also studied. The synthesis and microstructural study of NiFe nanowires encapsulated by multiwalled carbon nanotube radial structures is also presented in the same chapter. Magnetization measurements of Fe-based nanowires are also provided in this chapter.

Chapter 5 contains the overall conclusions that follow from this work.

Chapter 6 contains suggestions for future work.

Chapter 2

Literature review

In this chapter, a brief literature review of the various concepts related to carbon nanotubes, growth mechanism, structural and magnetic properties of the encapsulated nanowires is presented.

2.1 Carbon nanotubes

The lattice configuration of an individual SWCNT can be described with reference to Figures 2.1 and 2.2. SWCNTs are characterised by the way the graphene wall is wrapped in the direction of chiral vector $\mathbf{C}_h = n\mathbf{a}_1 + m\mathbf{a}_2$, where $\mathbf{a}_1$ and $\mathbf{a}_2$ are the graphitic Bravais lattice vectors and n and m are integers [57]. $\mathbf{T}$ is the translation vector parallel to the axis and the chiral angle θ is in between $\mathbf{a}_1$ and $\mathbf{C}_h$. The chiral vector $\mathbf{C}_h$ determines the circumference of the nanotube and differing values of n and m lead to different types of nanotube structures. For $m = 0$, the nanotubes are labelled zigzag. If $n = m$, the nanotubes are labelled armchair. Otherwise, they are labelled chiral. In terms of chiral angle, $\theta = 0^\circ$ for zigzag tubes and $\theta = 30^\circ$ for armchair tubes (see Figure 2.2). A turbostratic stacking of graphene sheets has been suggested for MWCNTs [58]. The reported wide d_{002} spacing, 0.34 nm, is due to the fact that adjacent graphitic sheets are parallel to each other but translational and rotational correlations between walls are

random [58].

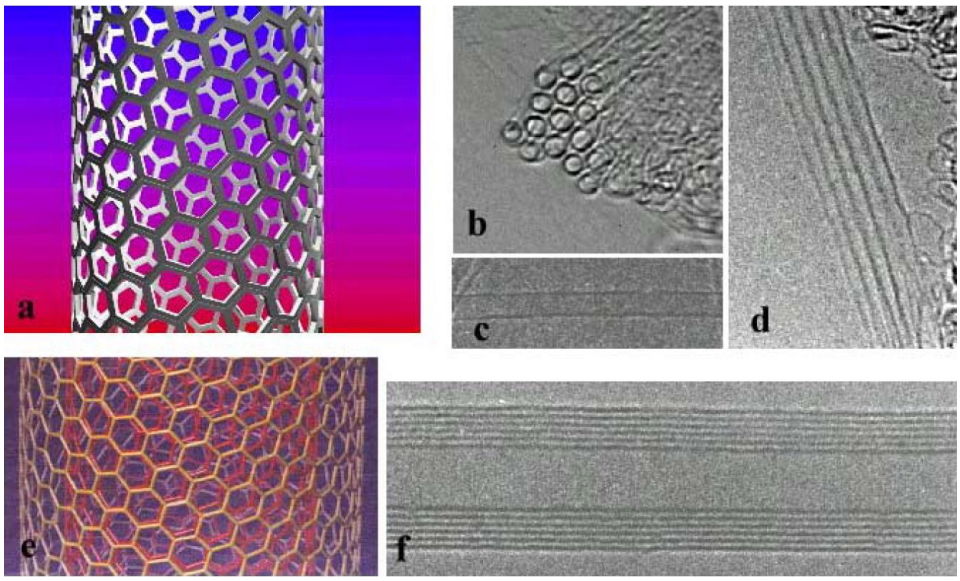

Figure 2.1: Structure of single-walled carbon nanotubes (a-d) and multiwalled carbon nanotubes (e,f). (a) shows a schematic of an individual chiral SWCNT. (b) shows a cross-sectional view (TEM image) of a bundle of SWNTs [transverse view shown in (d)]. Each nanotube has a diameter of $\sim$ 1.4 nm, the tube-tube distance in the bundles is 0.315 nm. (c) Shows a high-resolution TEM micrograph of a 1.5 nm diameter SWCNT. (e) is the schematic of a MWCNT and (f) shows a high resolution TEM image of an individual MWCNT. The distance between horizontal fringes (layers of the tube) in (f) is 0.34 nm (close to the interlayer spacing in graphite) [4].

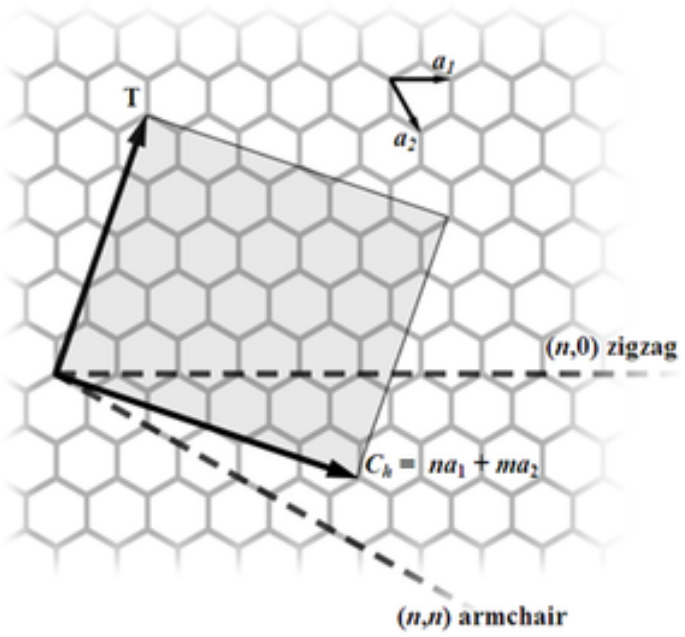

Figure 2.2: Detail of the SWCNT structure showing translation vector **T**, chiral vector $\mathbf{C}_h$, and Bravais lattice vectors $\mathbf{a}_1$ and $\mathbf{a}_2$ [5].

2.2 Chemical vapour deposition of transition-metal nanowires encapsulated by multiwalled carbon nanotubes

Chemical vapour deposition (CVD) is a widely used method for the production of nanowires encapsulated by carbon nanotubes. The reaction process can be initiated by heat (in thermal CVD), UV radiation (photo-assisted CVD) or plasma (plasma enhanced CVD) [59]. Previously, other synthesis methods have also been employed for synthesis of CNTs, such as arc discharge [60] and laser ablation [61]. These methods were aiming to synthesize pure and gain fine control over the properties of CNTs with the ability to produce at large scale. But soon all these methods were dominated by the CVD due its low cost, simplicity, higher level of control, purity of the yield and its potential for upscaling to commercial manufacturing prospects [62, 63].

CVD can be used to synthesise MWCNTs encapsulating nanowires of the elemental phases, alloys, or carbides of the transition metals. Essentially the synthesis method is similar to that of the hollow carbon nanotubes (single or multiwalled). In both cases, synthesis involved the decomposition of hydrocarbon as a precursor at high temperatures (700 °C to 1000 °C) and delivering the carbon over a transition-metal catalyst particle [64].

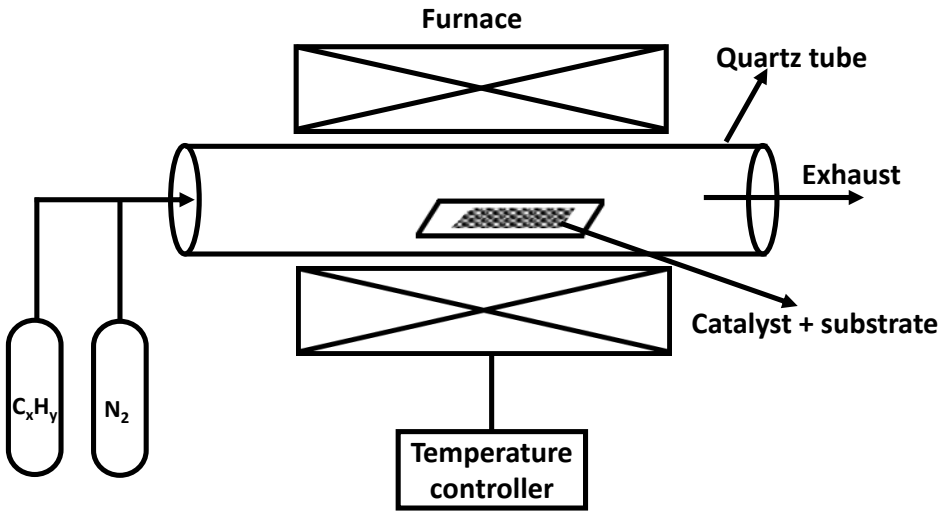

Figure 2.3: Schematic diagram of a typical CVD reactor used for the growth of empty carbon nanotubes

The catalyst is either located on a substrate (Si or SiO_2) or is delivered via gas phase along with the decomposed hydrocarbons using argon (Ar) or nitrogen (N_2) as a carrier gas (see Figure 2.3). The former can be used for the deposition of hollow carbon nanotubes which only requires hydrocarbons (methane, ethane or others). While the later is known as a floating catalyst process useful for the growth of carbon nanotubes encapsulating long nanowires realised by the use of organometallic compounds (metallocenes). Metallocenes ($M(C_5H_5)_2$) contain transition metal (M = Fe, Ni and Co) and carbon (C) in a fixed ratio of 1:10 with a sandwich-like molecular structure having metal at the centre between two cyclopentadienyl rings. These compounds include ferrocene, cobaltocene and nickelocene,

and possess a range of convenient temperature for sublimation as well as for thermal decomposition [9]. The molecular structure of ferrocene as a representative of metallocene is given in Figure 2.4.

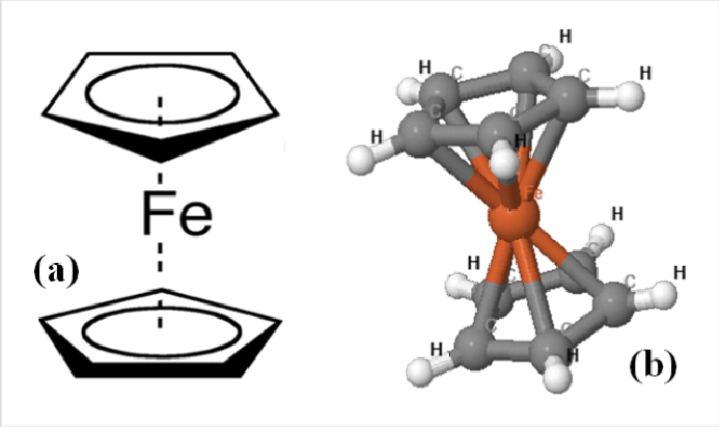

Figure 2.4: (a) Sandwich-like molecular stucture of ferrocene (b) and its view as 3D model [6].

Transition-metal nanowires encapsulated by MWCNTs are conventionally produced using two known CVD methods: solid-source CVD (SSCVD) [9, 32, 37, 65, 66] and liquid-source CVD (LSCVD) [9, 32, 65]. In SSCVD, a solid powder precursor (ferrocene or other metallocenes) is used, and in LSCVD a liquid precursor hydrocarbon (benzene, toluene and xylene etc.) in which often metallocenes are dissolved [9, 32, 37, 65–67]. In both cases, a two-zone horizontal CVD reactor is used. However, LSCVD is not suitable for the production of transition-metal nanowires encapsulated by MWCNTs owing to the high excess of carbon during the reaction which predominantly favour hollow carbon nanotubes encapsulating spherical catalyst nanoparticles (often Fe_3C) but no long nanowires [9].

In the following, we will only focus on SSCVD method for the production of transition-metal nanowires encapsulated by MWCNTs. In this method, metallocene powder in a quartz boat is sublimated in the preheater zone at a compound-specific temperature (e.g. for ferrocene, temperature range: 100 °C to 200 °C). The sublimated metallocene vapour is transferred in the main reaction zone by a controlled flow of a carrier gas (usually Ar

or N_2), where the decomposition of the metallocene and the subsequent growth of CNTs encapsulating transition-metal nanowires occurs [9].

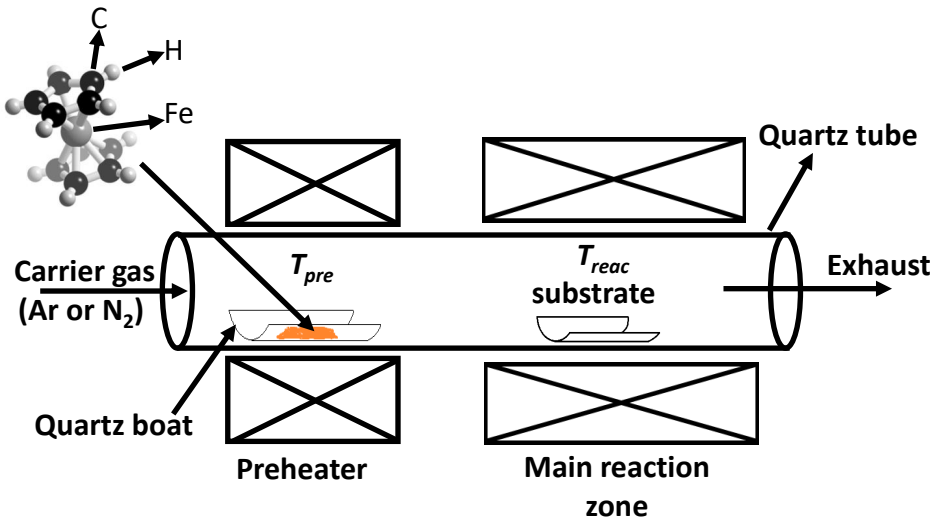

Figure 2.5: Setup for solid-source CVD system. Ferrocene is sublimated in the preheater zone and is transported via carrier gas to the main reaction zone where precursor decomposes and the formation of carbon nanotubes occurs.

It has been proposed that the decomposition of the metallocenes into transition metal (M) e.g. elemental iron (Fe), hydrocarbon and hydrogen species inside a quartz tube reactor initiates near 550 °C [9].

$$M(C_5H_5)_2 \longrightarrow M + H_2 + CH_4 + C_5H_6 + ... \tag{2.1}$$

The choice of sublimation temperature is vital to determine and regulate the sublimation rate in combination with amount of metallocene transferred into the reaction zone using the carrier gas flow. The growth temperature for Fe-based nanowires encapsulated by MWCNTs typically varies between 750 °C and 1100 °C [64].

For the synthesis of NiFe nanowires encapsulated by MWCNTs, LSCVD method have been mostly employed. Usually, a mixture of power ferrocene ($Fe(C_5H_5)_2$) and nickelocene ($Ni(C_5H_5)_2$) dissolved in a solvent (benzene, xylene etc.) and is transferred to

the reaction zone via aerosol spray using Ar or H_2 as a carrier. The transferred vapour thus contains two catalyst (Fe and Ni) instead of a single catalyst (Fe) for synthesis of encapsulated NiFe alloys nanowires [34, 38, 68].

The growth mechanism of the nanowires encapsulated by carbon nanotubes is a phenomenological description deduced from the experimental observations to explain different types of observed carbon nanotube structures and composition of the encapsulated nanowires [9]. Therefore the knowledge and understanding of growth mechanism is under continuous development and several modifications were discussed during the last two decades. However, the widely-accepted selected features of growth mechanism often explained in terms of adhesion force between the catalyst particle and the substrate, are useful for understanding the synthesis of nanowires encapsulated by carbon nanotubes by the CVD method [69–73].

There are two major growth mechanisms used to describe the catalytic growth process of CNTs [7, 8, 74–76]: (i) tip growth and (ii) base growth (Figure 2.6 (a) and (b)). In tip growth mechanism, the catalyst particle is located at the tip of the growing nanotube (Figure 2.6 (a)) and in base growth mechanism, the catalyst particle resides at the bottom of the growing nanotube in contact with the substrate (Figure 2.6 (b)).

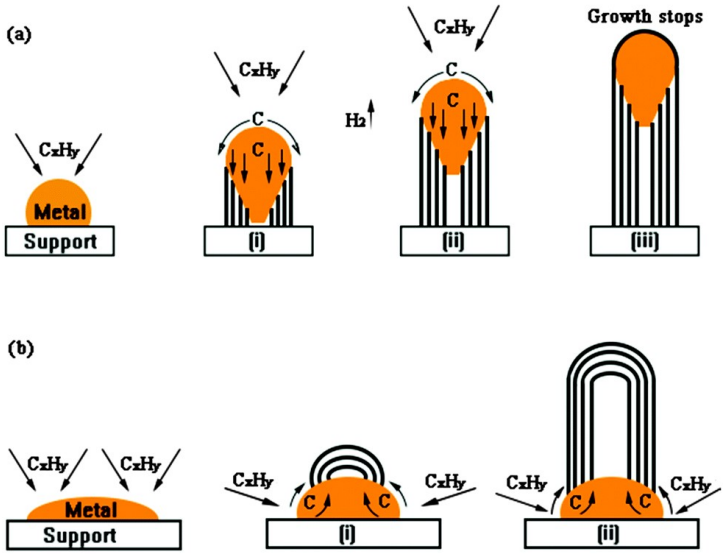

Figure 2.6: Schematic diagrams of growth mechanism for CNTs [7, 8]. (a) Shows the tip growth mechanism in which catalyst particle has weak adhesion with the substrate surface and catalytic decomposition of hydrocarbons occurs under an exothermic process at the upper surface of the metal particle. The increase in temperature and carbon concentration at the top of the particle deforms and subsequently detaches it from the substrate during this process. The carbon now diffuses to the colder side of the particle and precipitates to form the CNT shells. (b) Shows the base growth mechanism in which catalyst particle has strong adhesion with the substrate surface and initial catalytic decomposition of hydrocarbons and carbon diffusion occurs similar to the tip growth case, but the carbon precipitation fails to push the metal particle up; so the graphitic shells are compelled to emerge out from the metal's apex and the particle remains attached to the substrate.

In view of the above growth mechanisms, closely-packed aligned arrays of Fe-based nanowires encapsulated by MWCNTs self-organise on flat inert substrates when exposed to a steady flow of the products of ferrocene ($Fe(C_5H_5)_2$) pyrolysis at high temperature in a conventional CVD reactor. The thermally decomposed ferrocene comprises elemental iron, hydrocarbon species, and hydrogen [9]. The iron particles nucleate on the substrate and catalyse the decomposition of the hydrocarbon species, the released carbon then dissolves in the iron particles and provides the graphitic surface coating upon saturation from which the carbon nanotube grows. The continuous supply of vapour feedstock to the base of the structure or the open tip or both, facilitates the simultaneous growth of both nanowire and nanotube (see Figure 2.7 and 2.8). Such a growth process is based on heterogeneous nucleation, that occurs at the catalyst particle/substrate interface. The

most commonly observed single crystal phases in the encapsulated iron-based nanowires are Fe_3C, α-Fe and γ-Fe [9, 10, 33, 77, 78].

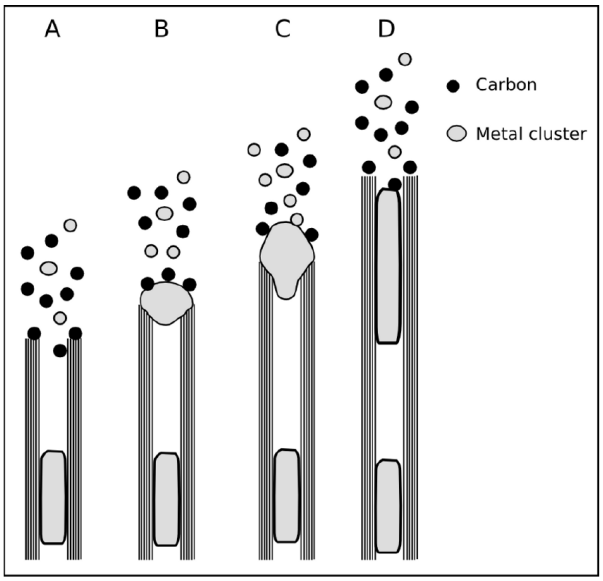

Figure 2.7: Schematic diagram showing simultaneous growth process of both nanowire and the nanotube. (A) shows a slow growth stage. The graphitic walls at the open tip react with carbon from the vapour feedstock. In (B) a bigger catalyst particle comes in contact with the open tip and the fast growth stage is initiated. (C) The CNT grows fast and the pressure caused by the graphitic walls deforms the catalyst particle to encapsulate. In stage (D) an encapsulated section is formed. If the catalyst material supply stops then the slow growth stage continues [9].

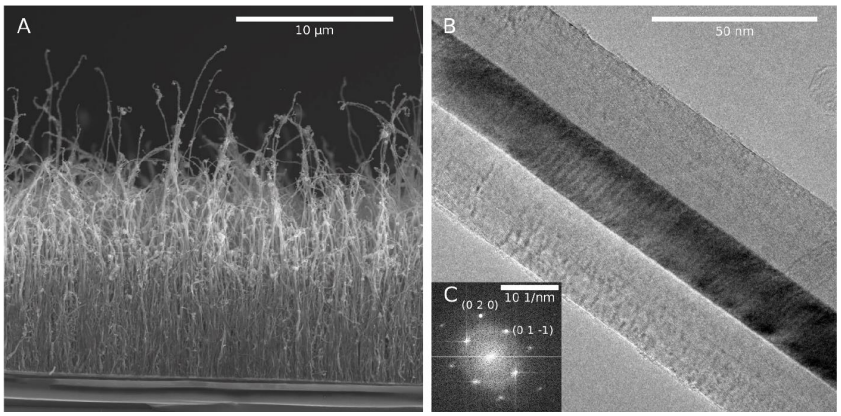

Figure 2.8: (A) Scanning electron micrograph showing surface-grown vertically-aligned arrays of iron-based nanowires encapsulated by MWCNTs. (B) Transmission electron micrograph showing the central nanowire encapsulated by MWCNTs. (C) The corresponding fast Fourier transform taken from the micrograph [9].

Here it is important to mention that the main advantage of the catalytic CVD is the

selective growth conditions, enabling the use of different types of substrates with complex morphologies, e.g. smooth quartz substrates [79], patterned substrates [80], and roughened substrates [10], which is not the case for arc discharge [60] and laser ablation [61]. Therefore, the use of roughened quartz substrate in a conventional horizontal CVD method led to the development of a new synthesis method for production of carbon nanotube radial structures, and is covered in the next section.

2.3 Boundary layer chemical vapour synthesis of Fe-based nanowires encapsulated by multiwalled carbon nanotube radial structures

Recently, Boi *et al.* demonstrated vapour-phase, homogenously nucleated equivalent structures through the use of intentionally roughened quartz substrates to produce powders of Fe-based nanowires encapsulated by multiwalled carbon nanotube structures radially departed from a central particle [10]. This method, coined boundary layer chemical vapour synthesis (BL-CVS), is a simple modification of the conventional CVD method in which the nucleating iron particles are formed in a layer of randomly fluctuating vapour produced by flowing over a roughened substrate [10, 59]. Consequently, the vapour feedstock is driven to the growth front from all directions therefore a radial structure is produced. These structures comprise multiwalled carbon nanotubes encapsulating iron-based nanowires departing from a central core which is an agglomeration of spherical Fe_3C nanocrystals individually encapsulated by graphitic shells (see Figure 2.9) [10].

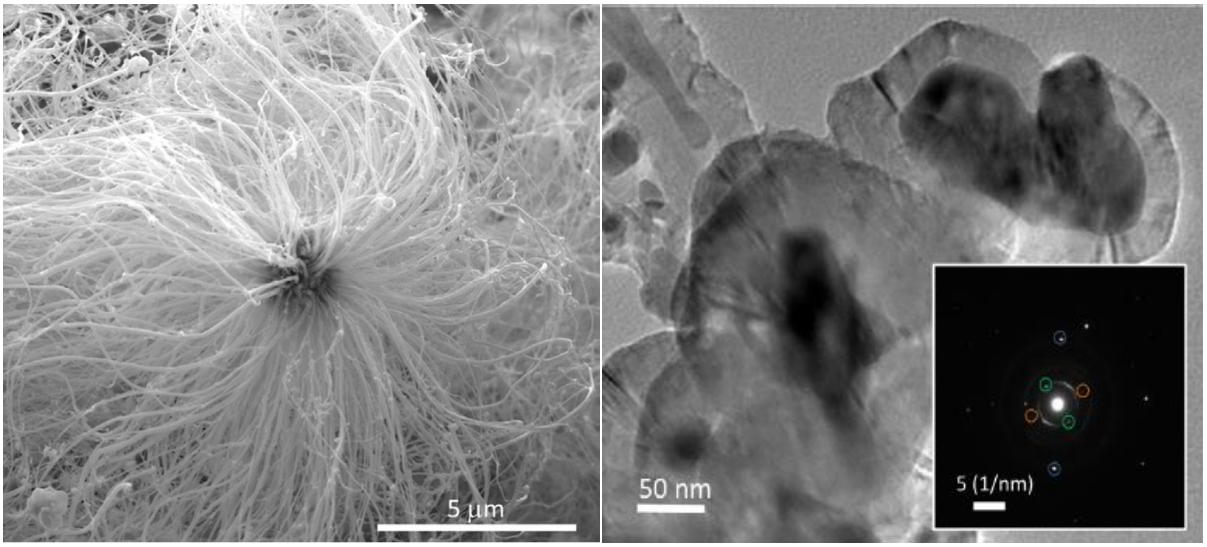

Figure 2.9: (left): Scanning electron micrograph of an individual radial structure comprising Fe-based nanowires encapsulated by multiwalled carbon nanotubes departing from a central particle, (right): Transmission electron micrograph of small particles observed in the central particle of the radial structure. Inset: selective area electron diffraction pattern obtained from one of the spherical particles. The orange circles indicate a lattice spacing of 0.25 nm corresponding to the (200) plane of Fe_3C with space group ($Pnma$). The blue circles indicate a lattice spacing of 0.11 nm corresponding to the (303) plane of Fe_3C with space group ($Pnma$). The green circles indicate the spots corresponding to the (002) lattice planes of graphite with spacing 0.33 nm [10].

Thus, the growth mechanism in BL-CVS is initialized by homogeneous nucleation, which is the principal advantage of BL-CVS over the conventional CVD method to prevent the catalyst particles from the contamination of the substrate material by avoiding iron/substrate contact. Therefore, the powder comprises of ensemble of the radial structures are of higher purity, and achieving better continuity of the encapsulated Fe-based nanowires than that observed with surface-grown structures in the same reactor conditions [10]. The radial structures are the dominant product and the reaction conditions are self-sustaining [10]. Recently, we also reported a successful demonstration of NiFe nanowires encapsulated by carbon nanotube radial structures using a SSCVD, in which a mixture of solid powders of $Fe(C_5H_5)_2$ and $Ni(C_5H_5)_2$ is sublimated in a quartz boat (maximum temperature of $\sim$ 180 °C) and is transferred via Ar into the reaction zone at 990 °C [1].

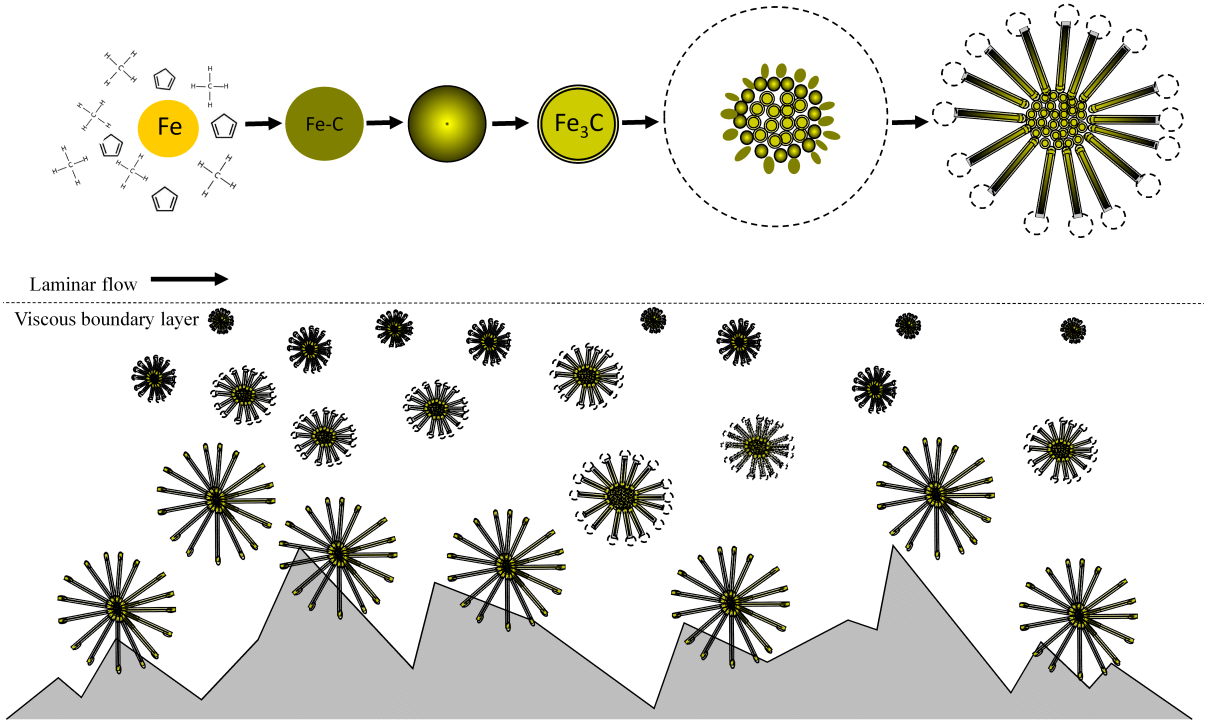

Figure 2.10: A schematic diagram describing the sequence of the radial structure formation in boundary layer chemical vapor synthesis; the pyrolysed metallocene flow is horizontal over the rough substrate using Ar-gas with flow rate of 12.5 ccm; spherically encapsulated nanocrystals rapidly nucleate and agglomerate at the boundary between laminar and viscous flow (dotted black lines represent the symmetry of diffusion gradients); peripheral nanocrystals are elongated by supply of feedstock species from the incoming vapour, these nucleate the growth of the radial nanotubes; the growth of the radial structure is driven by the diffusion gradient at the nanotube tips; the growth time in the boundary layer is determined by the competition between attractive forces from the substrate and thermophoresis; growth is halted by contact with the isothermal substrate [10].

Boi *et al.* proposed a growth model of the complete radial structure formation (Figure 2.10) [10]:

(i) The random fluctuations in the boundary layer create thermodynamic conditions for spontaneous formation of metal or metal-carbon particle in the vapour.

(ii) The carbon feedstock is driven to the particle by the resultant diffusion gradient and the subsequent dissolution of carbon in the particle occurs.

(iii) Formation of the graphitic carbon shells is initiated when the rate of arrival of the

carbon feedstock exceeds the rate of dissolution.

(iv) Subsequently the diffusion of internal carbon is driven to the surface by endothermic formation of the graphitic shells but it ceases when the stable Fe_3C spherical nanocrystal composition is reached.

(v) These spherical encapsulated Fe_3C nanostructures rapidly agglomerate to ease the formation of the central core by creating an inward spherically symmetrical diffusion gradient for the vapour feedstock (example concentration contours are given by the dashed lines in Figure 2.10). Peripheral Fe-C particles elongated by the spherical diffusion gradient provide the instability points from which radial nanotube and iron-based nanowire growth departs; vapour feedstock is now driven to the growth front at the tips of the nanotube by a thermal diffusion gradient created by the proximate endo- and exo-thermal processes.

The reactions were found to be self-sustaining, this has been explained as follows [10]:

(i) The rough surface creates randomly fluctuations in the boundary layer between the roughened surface and the laminar vapour flow.

(ii) The uniform diameter of the central agglomeration and radial structure suggests that nucleation occurs at the laminar-viscous interface since this is the realm of weak fluctuations and uniform feedstock supply from the global flow; after nucleation, the spherically symmetric diffusion gradients define the local feedstock supply to the nanotubes which serve to damp the local fluctuations in the boundary layer, subsequent radial structure formation in the boundary layer is therefore uniform. Attractive forces on the radial structure due to the proximity of the rough surface are greater than the thermophoretic forces so the structure migrates to the rough surface. The period of migration therefore dictates the diameter of the radial structure. Once the radial structure comes in contact with the surface, the growth

process switches-off because the isothermal surface equilibrates the temperature gradients at the tips. The roughness of the radial-structure deposits replicate the pristine rough surface and consequently the growth conditions are reproduced.

2.4 Volume expansion and stability of γ-Fe

As discussed in section 2.2 that the commonly observed single-crystal phases in the encapsulated iron-based nanowires are Fe_3C (orthorhombic), α-Fe (bcc) and γ-Fe (fcc) [9, 10, 33, 77, 78]. The unexpected presence of γ-Fe at room temperature has been attributed to the suppression of the $\gamma \rightarrow \alpha$ phase transition by confinement within the highly elastic graphitic walls of the carbon nanotube (elastic modulus circa 1 TPa) [33, 43, 49]. At one standard atmosphere pressure (100 kPa), bulk γ-Fe is stable only in the temperature range 912 °C to 1394 °C [11]. Kim *et al.* used Gibbs free energy approximation arguments to suggest that the presence of γ-Fe in the encapsulated nanowire is due to a 1.5 GPa pressure exerted on the nanowire by the nanotube resulting from a 9% volume expansion that accompanies the $\gamma \rightarrow \alpha$ phase transition in iron [49, 50]. The presence of this internal pressure has been assumed without experimental justification but this unexpected presence of γ-Fe phase at room temperature is generally attributed to the pressure-induced encapsulation by the MWCNTs [14, 15, 81]. In addition, the details of the 9% volume expansion associated with the $\gamma \rightarrow \alpha$ phase transition in the Fe-based nanowires have not been provided by Kim *et al.* [49, 50]. In bulk this expansion is less than 1% at transition temperature of 912 °C (see Figure 2.11 and Table 2.1) [11, 25].

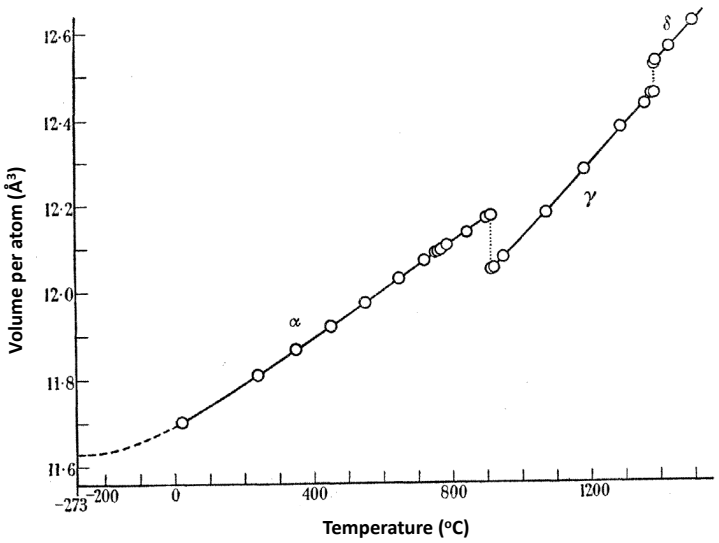

Figure 2.11: Volumeteric expansion of pure iron [11].

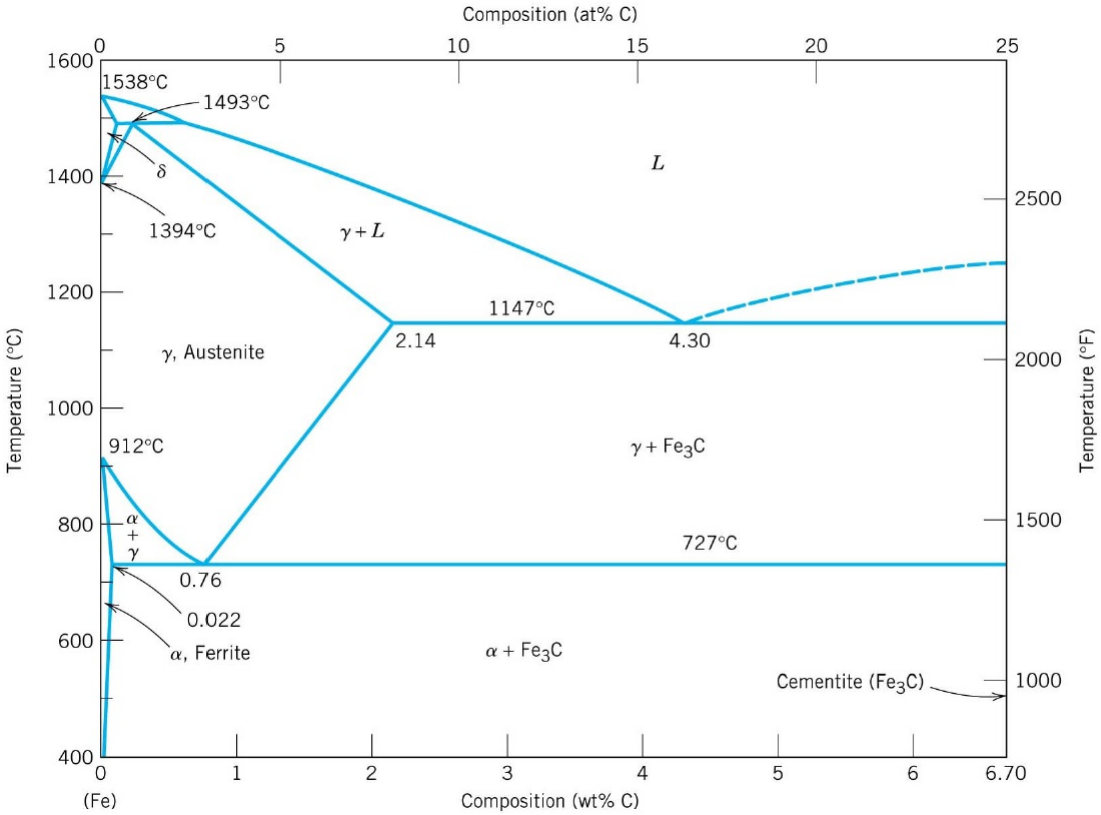

Figure 2.12: The Fe-C phase diagram [12].

According to the iron-carbon phase diagram (see Figure 2.12), α-Fe (bcc) is stable below 727 °C. The transition of α-Fe (bcc) to γ-Fe (fcc) starts at $\sim$ 727 °C and is complete at

temperatures $\sim$ 1000 °C. This means that if the synthesis is performed at temperatures $\sim$ 1000 °C, the main phases involved in the CNTs nucleation and growth will be γ-Fe and Fe_3C. However during the cooling process, the majority of the γ-Fe (fcc) phase will revert to the α-Fe (bcc) and Fe_3C (orthorhombic) phase (at room temperature), while the metastable Fe_3C could decompose into α-Fe and and graphitic carbon in a slow process, which is thermodynamically stable at room temperature [12, 25, 37, 77, 82]. In contrast, Heresanu *et al.* suggested the use of rapid cooling process to freeze the Fe_3C crystals inside the MWCNTs [83].

	$\alpha \rightarrow \gamma$(912°C)		
	α	γ	Change (%)
Lattice parameter, a (Å)	2.895	3.637	+26
Shortest distance, $2R$ (Å)	2.507	2.572	+2.6
Volume per atom (Å^3)	12.13	12.03	−0.9

Table 2.1: Changes of the lattice parameter, the shortest interatomic distance and the specific volume (i.e. volume per atom) for pure iron upon the transition α-Fe (bcc) $\rightarrow$ γ-Fe (fcc) at 912 °C and at standard pressure ($\approx$1 atm) [25].

The ability of carbon to alloy with γ-Fe is high owing to the large diameter of the octahedral interstices (0.52 Å) where carbon atoms can be introduced [84, 85]. Dilute carbon alloys of γ-Fe are stable at room temperature [86]. The physical properties of carbon-free γ-Fe at room temperature can be extracted by extrapolating the carbon concentration dependence to zero solute content [86]. The lattice parameter for γ-Fe at room temperature extracted in this way is 3.556 Å (atomic volume 11.241 Å^3). Interstitial carbon does not significantly influence the magnetic moment of bulk γ-Fe but does affect surface anisotropy [87]. But carbon incorporation does impact on the overall magnetic properties through an increase in the lattice parameter and the volume per atom relative to unalloyed γ-Fe [86]. Although the magnetic phenomena associated with carbon incorporation are well-known, there has been no discussion in the context of Fe-based nanowires encapsulated by carbon nanotubes. The dilute carbon alloying concentration can be estimated

by using Vegard's law; a linear relationship between the lattice parameter and carbon concentration given below

$$a = 3.556 + 0.044x \tag{2.2}$$

where x= wt. % carbon, and a is the γ-Fe lattice parameter [46, 47].

2.5 Magnetic properties and applications of Fe-based nanowires encapsulated by multiwalled carbon nanotubes

The magnetic properties of Fe-based nanowires encapsulated by multiwalled carbon remained a central focus of research for more than a decade owing to the envisaged potential applications such as magnetic hyperthermia cancer therapy, magnetocaloric refrigeration, microwave absorption, magnetic sensors, probes for magnetic force microscopy and many others [1, 9, 10, 32, 33, 35]. The encapsulation of the Fe-based nanowires by the weakly diamagnetic MWCNTs is to isolate an individual nanowire, to ensure the long-term chemical and mechanical stability [1, 30–32, 88]. However, the metal-carbon interface influences the structural and magnetic properties of the nanowire [33, 89]. Various reports have shown that the magnetic properties of the nanotube encapsulated Fe-based nanowires differ from those of bulk samples or other low-dimensional systems such as small spherical particles and thin films [9, 10, 32, 33, 35]. The commonly observed encapsulated phases inside the Fe-based nanowire includes; ferromagnetic α-Fe (bcc) and Fe_3C (orthorhombic), and the possible antiferromagnetic γ-Fe (fcc) [9, 10, 32, 33, 35].

The magnetic properties of Fe-based nanowire are dependent on crystal anisotropy along certain preferential directions. The magnetic properties of α-Fe, which is ferromagnetic in nature, strongly depends on the axial shape anisotropy [90] while, that of Fe_3C are strongly dependent on the magnetocrystalline anisotropy [90, 91]. The graphitic layers of

the MWCNT are weakly diamagnetic at T<50 K [92]. The coercivity of these nanostructures appears to be strongly dependent on the alignment [37], the magnetocrystalline anisotropy [17, 90, 91, 93], the nanowire diameter, and the spatial-distribution of the encapsulated phases inside the nanotubes [33, 43]. The saturation magnetization of a powder comprising of MWCNT encapsulating α-Fe, γ-Fe (fcc) and Fe_3C are dependent mainly on the content of α-Fe [37, 66].

Recently, Kumari *et al.* reported Fe_3C encapsulated by MWCNTs as permanent cylindrical nanomagnets exhibiting exotic magnetic properties [94]. Whereas Guo *et al.* reported the observation of large coercivity (1400 Oe) in the Fe_3C nanowires encapsulated by MWCNT radial structures [95].

The γ-Fe (fcc) was inferred as antiferromagnetic due to the observation of a shifted hysteresis loop, which led the authors to conclude the existence of α-Fe (ferromagnetic)/γ-Fe (antiferromagnetic) junctions in their sample [33, 42, 43]. This shift in hysteresis is a signature of an interesting phenomena called an exchange bias effect, Figure 2.13 [13, 33, 41, 96, 97]. This effect was first reported by Meiklejohn and Bean in 1956 [13]. Afterwards, different theoretical models have been so far proposed for the understanding of this effect [13, 41, 96, 97].

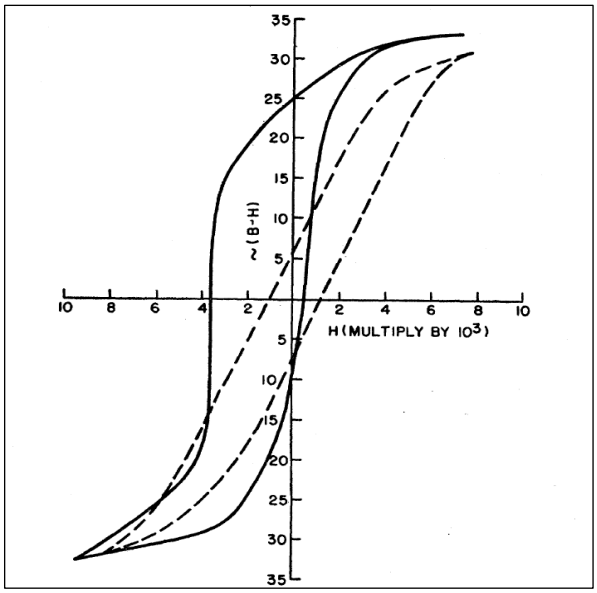

Figure 2.13: A shifted hysteresis observed by Meiklejohn and Bean showing the Exchange bias phenomenology resulted due to antiferromagnetic and ferromagnetic coupling at 77 K [13].

On the other hand, Karmakar *et al.* investigated the randomly oriented samples of Fe-based nanowires encapsulated by MWCNTs containing a negligible fraction of γ-Fe, and concluded that γ-Fe may not be the only antiferromagnetic component causing exchange bias effect, rather this effect has been attributed to the presence of disordered surface spins [35]. In contrast, Mühl *et al.* observed no shift in the hysteresis loop even with the presence of a large γ-Fe content along with α-Fe in their sample of aligned Fe-based nanowires encapsulated by MWCNTs. Their study suggested negligible coupling between α-Fe and γ-Fe at low-temperature [89]. γ-Fe has been reported to be antiferromagnetic at low temperature below 100 K [33], and paramagnetic state at room temperature was inferred from Mössbauer spectroscopy [44, 98, 99].

Moreover, a theoretical study of bulk γ-Fe by Kaufman *et al.* in the 1960s pointed to the possibility of two different possible magnetic states: the low spin (antiferromagnetic state) and the high spin (ferromagnetic state) dependent on the lattice parameter and atomic volume (volume per atom). This study predicted lattice parameters of 3.54 Å (atomic volume 11.090 Å^3) associated with the antiferromagnetic state (0.5 μ_B/atom)

and 3.64 Å (atomic volume 12.057 Å^3) with the ferromagnetic state (2.8 μ_B/atom) at room temperature [45]. Another study, using local-spin-density approximation conducted two decades later, predicted γ-Fe to be antiferromagnetic, ferromagnetic, or nonmagnetic depending on lattice parameters, crystallite size, and surface atom coordination [100].

2.6 Spatial distribution of encapsulated phases

Two types of spatial distribution of encapsulated phases along the nanotube axis have been inferred from Mössbauer spectroscopy and magnetization measurements: (i) sequential, and (ii) concentric [33, 37, 42–44].

A concentric model was proposed by Prados *et al.* and Marco *et al.* in which α-Fe single crystals act like a core that is surrounded by γ-Fe and then Fe_3C single crystals [33, 42, 43]. This model provides sufficient surface contact of α-Fe and γ-Fe for the expectation of a significant shift in hysteresis due to strong exchange coupling. Leonhardt *et al.* proposed a different model in which γ-Fe concentrations were found to be higher near the tips of the nanotubes and this is the similar result obtained by Ruskov *et al.* which showed that γ-Fe was near the nanowire surface [37, 44]. Müller *et al.* also reported the microscopic observation of γ-Fe located at the tip of the nanotube (see Figure 2.14 (b)).

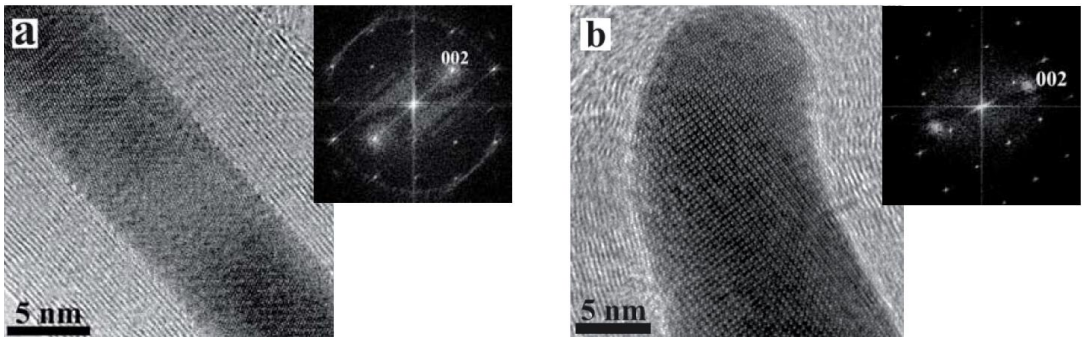

Figure 2.14: High-resolution transmission electron micrographs of single crystals iron-based nanowires encapsulated by multiwalled carbon nanotubes. (a) The lattice fringes of α-Fe and the corresponding fast Fourier transform. (b) Showing the encapsulated γ-Fe located at the tip of the nanotube and fast Fourier transform of the high-resolution TEM image [14].

In contrast to Prados *et al.*, Karmakar *et al.* observed a small fraction of γ-Fe with a spatial distribution and suggested that such fraction of γ-Fe and configuration may not be enough to understand exchange bias effect [35]. Recently, Boi *et al.*, reported the presence of a small fraction of γ-Fe at the tips of the radial structured MWCNTs inferred from the saturation magnetisation [10]. This is also in agreement with the reports of Leonhardt *et al.*, Müller *et al.* and Ruskov *et al.* [14, 37, 44]. While studying the atomic structure of the encapsulated Fe-nanowires, Golberg *et al.* reported the existence of atypical crystallites of γ-Fe nanowires. The crystal planes exhibited exact orientation relative to the nanotube axis but this orientation is not specific. A variety of γ-Fe crystal planes parallel to the nanotube walls, such as (111), (331), (220), was found to exist (Figure 2.15) [15].

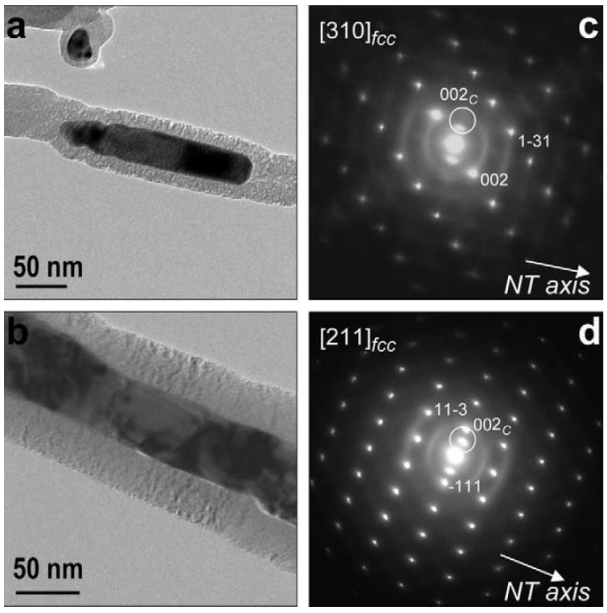

Figure 2.15: (a,b) TEM images and (c,d) corresponding selected area electron diffraction pattern depicting the existence atypical γ-Fe nanowires inside CNTs at room temperature. The identified zone axis in SAED patterns (c) and (d) are indexed as those seen along the [310] and [211] directions of the γ-Fe lattice. The (002) spots is originated from the shielding graphitic layers of the nanotubes [15].

Zhang *et al.* reported the observation of single crystal γ-Fe nanowires encapsulated by MWCNTs [16]. The (002) crystal planes of γ-Fe are being oriented parallel to the

nanotube axis (Figure 2.16) [16].

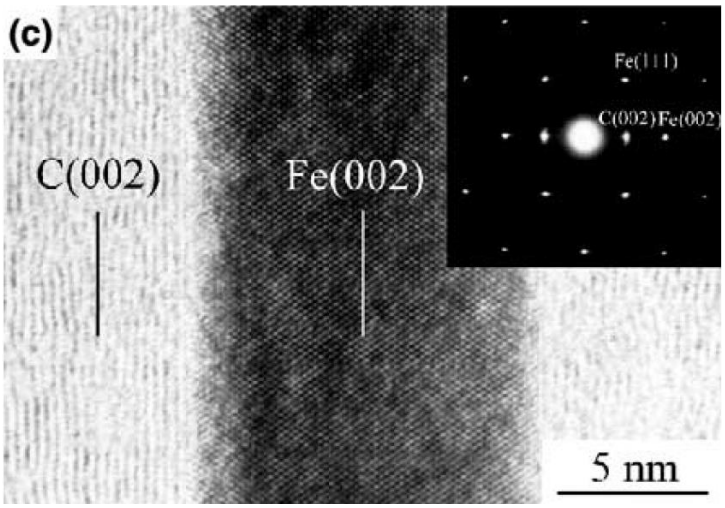

Figure 2.16: High-resolution transmission electron micrograph of a crystalline Fe-based nanowire encapsulated by MWCNTs and the corresponding selective area electron diffraction pattern (top right inset), showing single crystal γ-Fe and the (002) lattice planes of γ-Fe are parallel to the tube axis [16].

A microscopic observation reported by Morelos-Gómez *et al.*, in which splitting or doubling of the diffraction spots (see Figure 2.17) was attributed to the existence of concentric (coaxial) volumes of α-Fe and Fe_3C [17]. However, this effect could be resulted from the contact between sequential crystallites over an area that is a significant fraction of that of the probing electron beam.

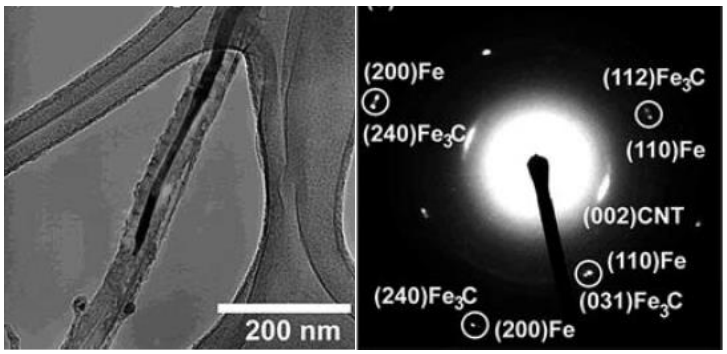

Figure 2.17: α-Fe/Fe_3C concentric (coaxial) junction in Fe-based nanowires encapsulated by multiwalled carbon nanotubes [17].

2.7 Microstructure and applications of NiFe nanowires encapsulated by multiwall carbon nanotubes

Nickel-iron alloys are of great commercial interest owing to their soft magnetic and thermal expansion properties. The understanding of microstructure of the crystalline NiFe alloys is not only important due to their presence in meteorites and also in the core of earth but they are economically advantageous compared to other materials considered for magnetocaloric refrigeration applications [101, 102]. A decade ago, these alloys have been identified for temperature compensator applications due to their low Curie temperature [18]. Therefore, efforts have been devoted to investigate the microstructural properties of these alloys [38, 39, 68, 103–105].

In particular, metastable γ-NiFe (fcc) alloy have attracted the attention of the researchers as an alternative candidate for the room temperature magnetocaloric refrigeration applications owing to its high efficiency and reduced cost aiming to lessen and eliminate dependence on rare-earth materials [38, 39, 68, 103–105]. In order to achieve this goal, alloys of transition metals (Fe, Ni and Co) have been investigated to replace the rare-earth metals [103]. The economic viability of NiFe alloys and its potential for scalable production along with the competitive magnetocaloric properties make it a promising candidate for the magnetocaloric refrigeration applications.

Miller *et al.* and McNerny *et al.* investigated γ-NiFe (fcc) nanostructures with tunable Curie temperatures down to 78 °C led the authors to conclude that γ-NiFe would impact applications requiring low-temperature range like magnetic hypothermia cancer therapy and polymer curing [104, 105]. In an overview on nanocrystalline γ-NiFe carried out by Ucar *et al.*, it has been pointed out that a good understanding of surfaces and interfaces is important for determining the role of exchange bias effect and will eventually impact on the magnetocaloric refrigeration applications near room temperature [102]. Recently, Ucar *et al.* reported the γ-NiFe alloy with tunable Curie temperatures exhibiting mag-

netocaloric properties near room temperature ($\approx$ 333 K) [40]. This provides a reasonable ground to emphasize on the microstructural analysis of the NiFe alloys and in particular the γ-NiFe.

Owing to the envisaged potential applications based on excellent structural and magnetic properties, NiFe alloy nanowires encapsulated by MWCNTs attracted significant interests of the researchers in the past decade [1, 34, 39]. The advantage of carbon nanotube encapsulation of NiFe nanowires, provides an effective shielding against oxidation and mechanical degradation, ensuring long-term stability to retain intrinsic crystalline properties of the nanowires [1, 30–32, 34, 56]. The commonly observed encapsulated phases reported in NiFe nanowires are α-NiFe (bcc) and γ-NiFe (fcc) [38, 39, 68]. The Curie temperature of NiFe alloys can be easily tuned by changing the relative concentration of Ni and Fe [106, 107].

Recently, the presence of Ni_3Fe alloy nanoparticles encapsulated by graphene nanocomposites exhibiting ferromagnetic magnetic properties have been reported [108]. In addition, radial structures comprising of FeCo nanowires have been produced using with multiple metallocene (ferrocene and cobaltocene) vapour in boundary layer chemical vapour synthesis [95].

According to the Ni-Fe phase diagram (Figure 2.18), Ni rich alloy Ni_3Fe formation takes place during the slow cooling process and at low temperatures, Figure 2.18. Ni_3Fe nanowires possess slightly larger magnetic moment compared to α-NiFe and γ-NiFe [86].

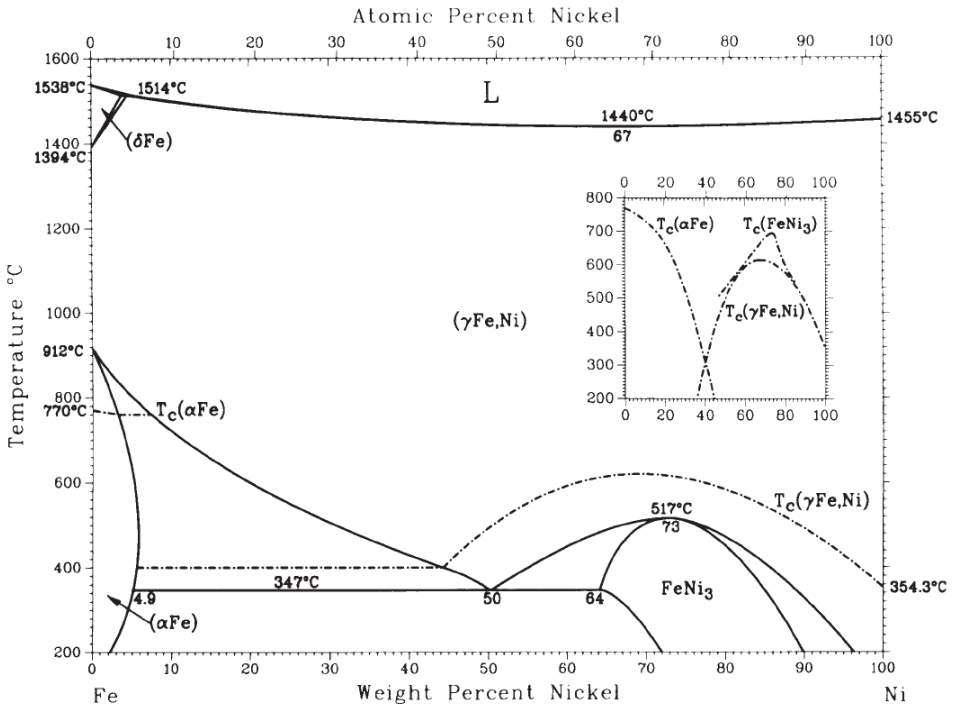

Figure 2.18: The nickel-iron (NiFe) binary phase diagram [18].

Crystalline nickel-iron alloy nanowires encapsulated by multiwalled carbon nanotubes are an important class of nanostructure materials of great technological importance owing to the already identified potential applications such as microwave absorption, magnetic shielding and a medium for hydrogen absorption due to their remarkable structural and magnetic properties [109–111].

In conclusion, little effort has been devoted to the microscopic studies of the encapsulated NiFe nanowires and a limited literature is available on the microstructural details of the α-NiFe and γ-NiFe. Therefore, we focused on the microstructural analysis of NiFe nanowires.

2.8 Conclusion

In conclusion, BL-CVS is a simple method based on a self-organized growth mechanism for carbon nanotubes. The principal reasons to consider radial structures for magnetocaloric refrigeration applications rather than surface-grown aligned nanotubes are;

(i) The method of synthesis is promising for mass production.

(ii) It does not require ultrafine-control over the synthesis parameters.

(iii) The nanowires are continuous on the scale $\sim$9 μm (at least one order of magnitude greater than can be achieved by conventional methods).

(iv) The proven alloying abilities of transition metals (Fe and Ni), an alternative route to tune the magnetic properties of the composite system.

(v) Have the greater possibility of creating multiple α-Fe/γ-Fe junctions.

(vi) The greater surface to volume ratio of radial structure morphology makes it a promising candidate for magnetocaloric refrigeration application.

Chapter 3

Experimental methods

In this chapter, a brief description of experimental methods and techniques used in this work is presented.

3.1 Synthesis

The BL-CVS method was used to synthesize Fe-based and NiFe nanowires encapsulated by MWCNT radial structures [10]. The radial structures were produced by flowing metallocene vapour over a roughened quartz substrate at an elevated temperature in a horizontal CVD reactor. The source and purity of metallocenes used: ferrocene 98%, $Fe(C_p)_2$ (Aldrich Prod. No. F408), and nickelocene 98%, $Ni(C_p)_2$ (Aldrich Prod. No. N7524), where C_p is the cyclopentadienyl ligand. A schematic diagram of the CVD reactor is provided in Figure 3.1. This quartz-tube reactor had the following dimensions; length: 2 m, outer diameter: 22 mm, inner diameter: 19 mm, wall thickness: 1.5 mm. The first part of the reactor is a preheater zone where 70-80 mg of metallocene powder was sublimated at a maximum temperature of 180 °C using a preheater coil and subsequently driven by argon to the main reaction zone of the furnace. The radial structures were produced with a very low flow rate of 12.5 ccm.

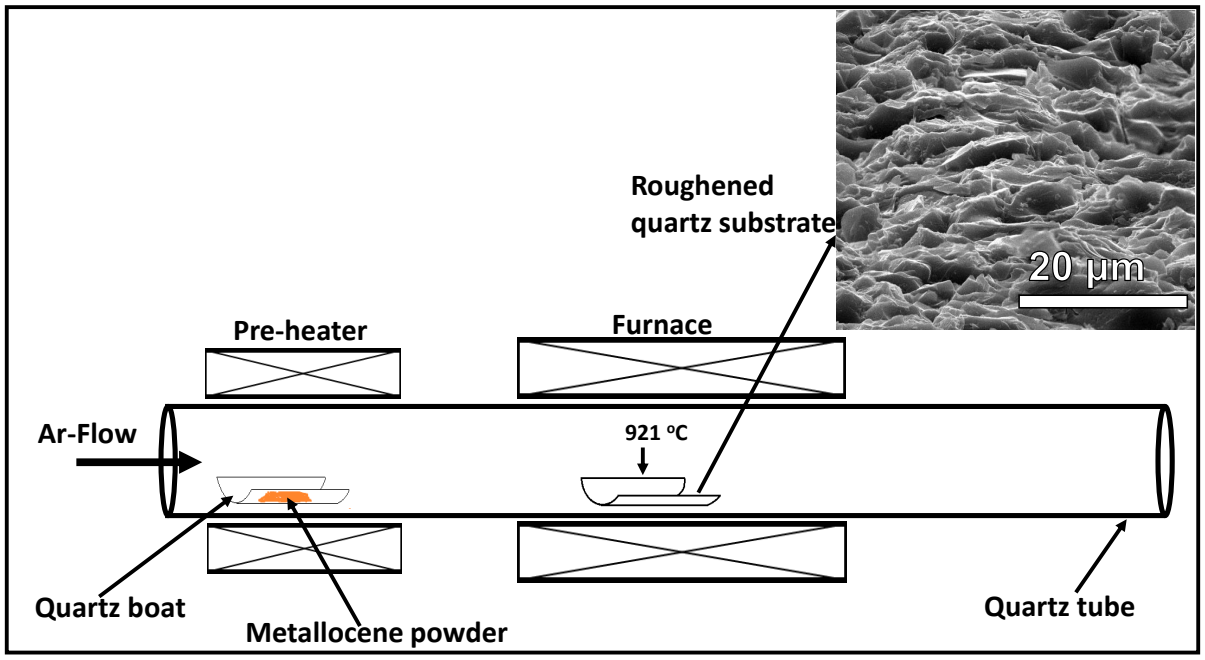

Figure 3.1: Schematic diagram of the horizontal CVD reactor used for the synthesis of the radial structures and scanning electron micrograph of a typical roughened quartz substrate.

A temperature profile measured inside the quartz tube for the first 30 cm from the entrance of the furnace is given in Figure. 3.2. A scanning electron micrograph of the multiscale roughened quartz substrate used to create randomly fluctuating vapour in the reaction zone is given at the top right of Figure. 3.1. The roughness with a peak-to-valley distance of ~ 100 μm was achieved using a conventional diamond-saw tool. The duration of the synthesis was typically three to five minutes measured from the switching on of the pre-heater to the complete sublimation of the metallocene powder.

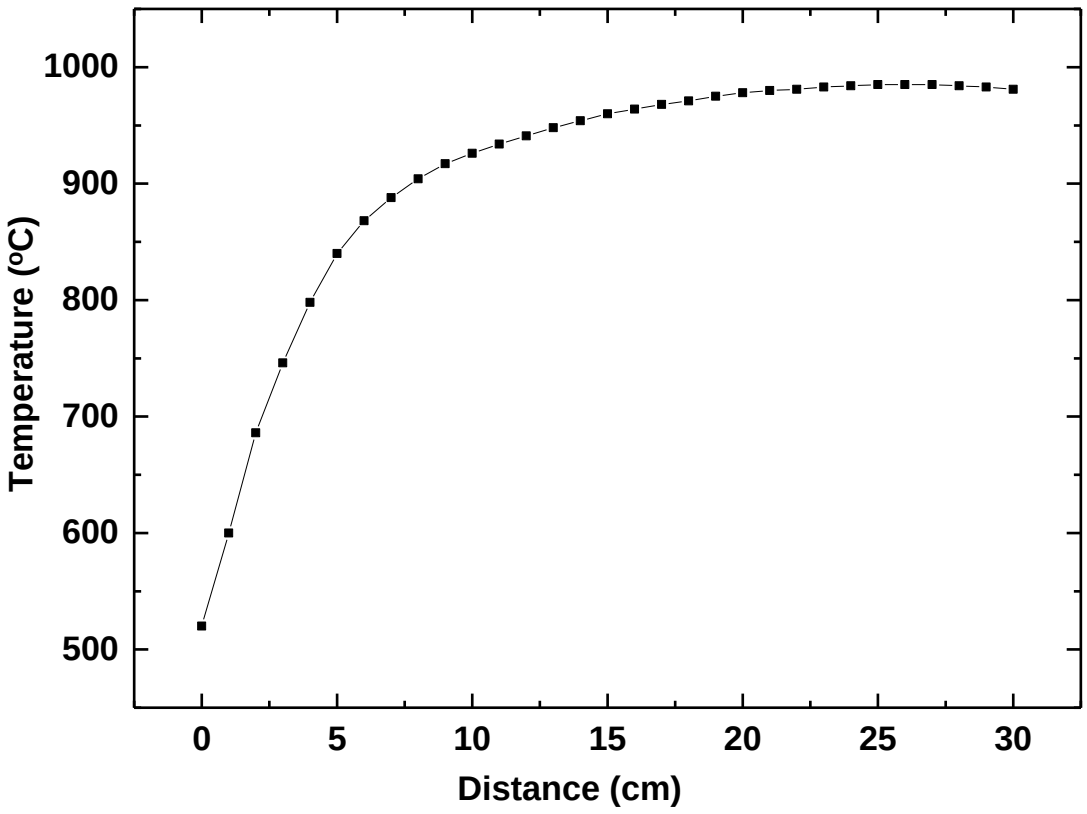

Figure 3.2: A temperature profile of the first 30 cm distance of the furnace measured from the entrance in the direction of the Ar flow.

3.1.1 Synthesis of high γ-Fe-content nanowires

For achieving high γ-Fe-content inside Fe-based nanowires encapsulated by multiwalled carbon nanotube radial structures, synthesis was performed by sublimating 70-80 mg of powder ferrocene only, creating a vapour flow over three sequentially arranged roughened quartz substrate at elevated temperatures in a horizontal CVD reactor given in Figure 3.3. The three roughened quartz substrates were placed at different locations within the reactor at corresponding temperatures of 878 °C, 921 °C and 944 °C (Figure 3.3). In this experiment, the optimum location for production of high γ-Fe-content nanowires was

found by a trial-and-error process. After the synthesis was completed the reactor was cooled to room temperature at the natural rate of the furnace (2 °C/min). The radial structures were found to have a weak adhesion with the substrates and could easily be removed magnetically or mechanically from the quartz substrates.

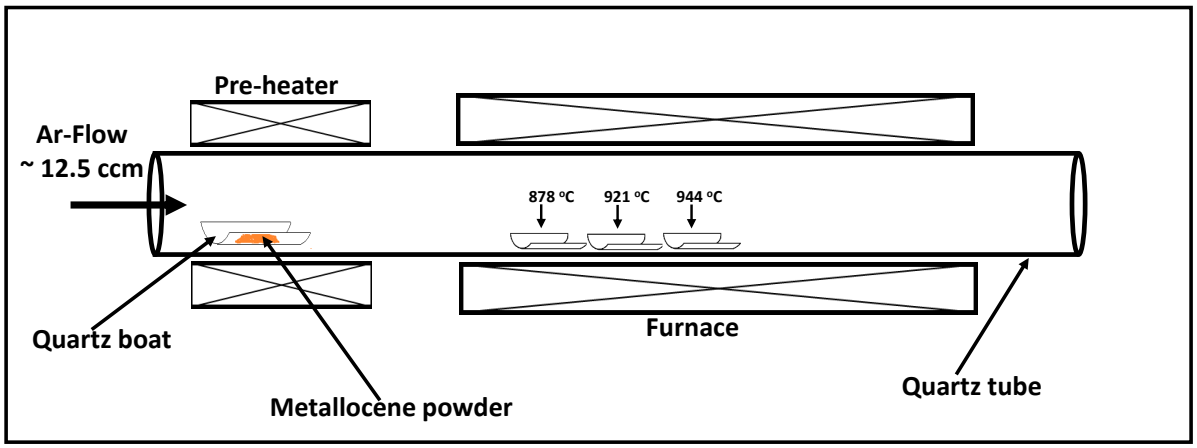

Figure 3.3: Schematic diagram showing the sequential arrangement and temperature of the roughened quartz substrates.

3.1.2 Substrate preparation and testing growth model

The influence of substrate roughness on the growth mechanism and microstructure of radial structures was investigated by a comparative study using quartz substrates low- and high-roughness (see Figure 3.4). Two types of roughened quartz substrates with multi-scale roughness were prepared to test the proposed growth model for radial structures formation. The high-roughness of the quartz substrate with a peak-to-valley distance of ~ 100 μm was achieved by using a conventional diamond-saw and the low-roughness of the quartz substrate with a peak-to-valley distance of ~ 25 μm was achieved by sand-blasting. These two low- and high-roughness quartz substrates (see Figure 3.4) have been exposed to the vapour flow of pyrolyzed ferrocene driven by Ar, at identical thermal locations ($T = 910$°C) in a horizontal CVD reactor in two separate experiments. Each time, 70 mg of the ferrocene was sublimated in the preheater zone ($T = 180$°C) to create the

vapour source and then transporting to the reaction zone using Ar flow at the rate of 12.5 ccm. The duration of the reactions was measured to be 3 minutes. The reactor was cooled to room temperature at the natural rate.

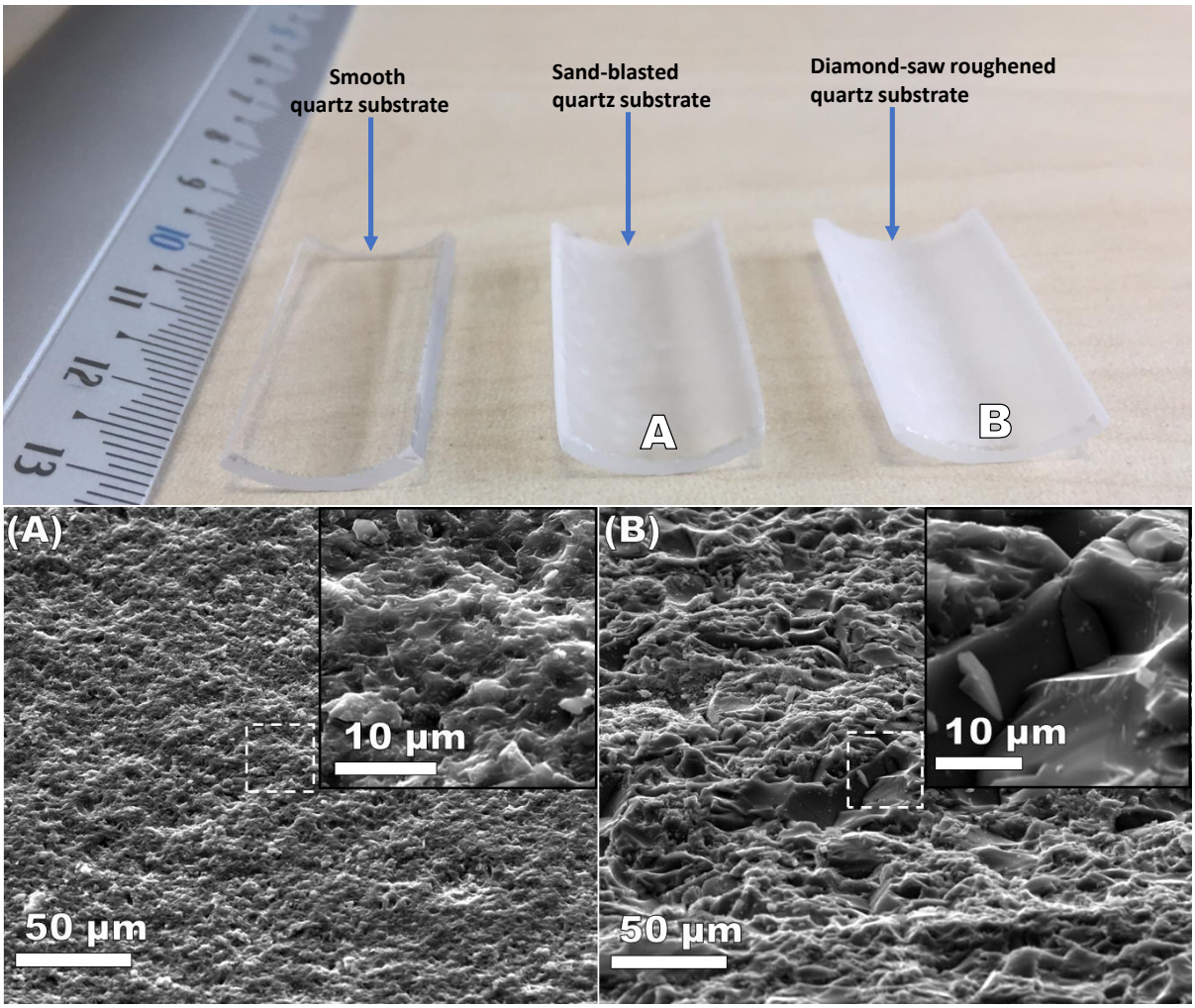

Figure 3.4: Scanning electron micrographs of the of the low- and high-multiscale roughness quartz substrates labelled A and B, receptively.

3.1.3 Synthesis of encapsulated NiFe nanowires

For the synthesis of encapsulated NiFe nanowires, a 100 mg mixture of powder ferrocene and nickelocene in the ratio (1:1) was sublimated to create an Ar driven vapour flow over a single roughened quartz substrate at an elevated temperature in horizontal CVD reactor

illustrated in Figure. 3.5 (A). The source and purity of metallocenes used: ferrocene 98%, $Fe(C_p)_2$ (Aldrich Prod. No. F408), and nickelocene 98%, $Ni(C_p)_2$ (Aldrich Prod. No. N7524), where C_p is the cyclopentadienyl ligand.

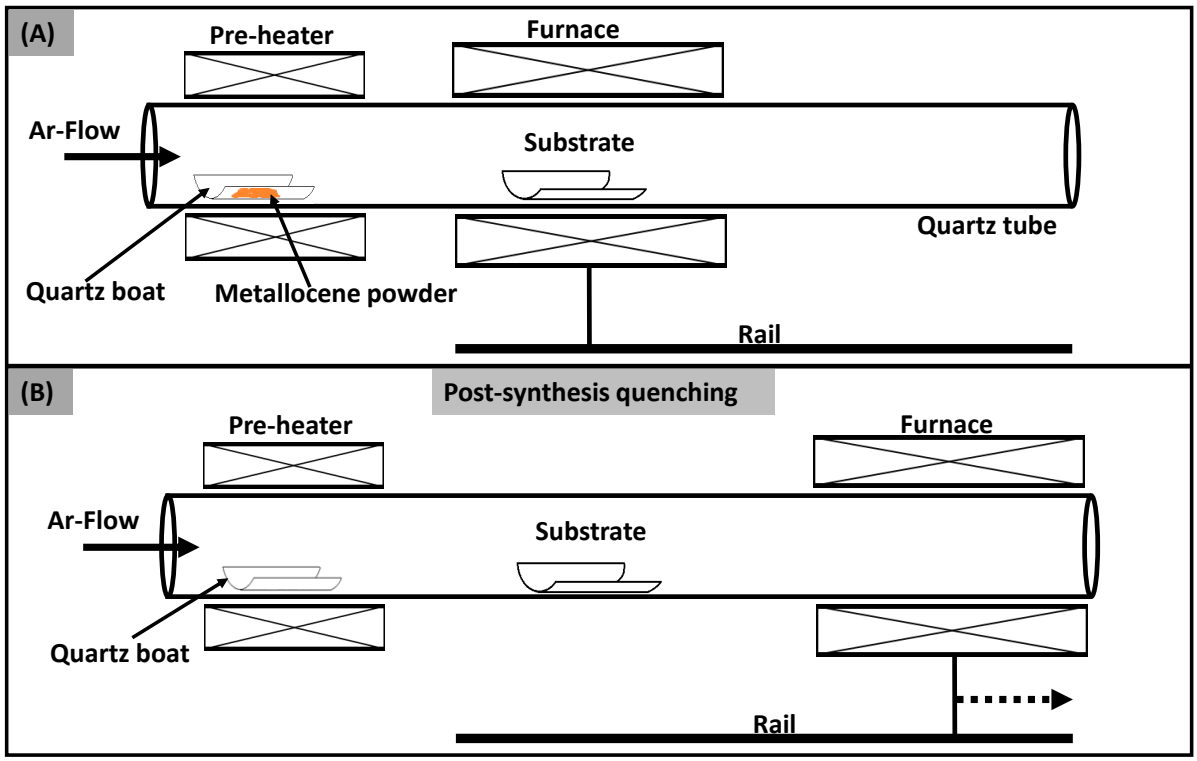

Figure 3.5: (A) Schematic diagrams of the horizontal CVD reactor used for the synthesis of NiFe radial structures and (B) shows the post-synthesis quenching process.

After synthesis, the reactor was cooled down to 700 °C at its natural rate and then annealed at this temperature for 1 hour followed by a quench (rapid cooling to room temperature) by sliding the furnace along its mounting rail in the direction of Ar flow (see Figure. 3.5 (B)).

3.2 Characterisation

Scanning electron microscopy (SEM), X-ray diffraction (XRD), transmission electron microscopy (TEM), aberration corrected (scanning) transmission electron microscopy

((S)TEM) were used to analyse the morphology, phase composition and microstructure of the Fe-based and NiFe nanowires encapsulated by MWCNTs. Energy dispersive X-ray spectroscopy (EDX) was used for chemical composition and acquiring elemental maps of the crystalline NiFe nanowires. A quantum design magnetic property measurement system (MPMS) magnetometer combined with superconducting quantum interference device (SQUID) was used for magnetic characterization.

3.2.1 X-ray diffraction

(i) Basic Principle

X-rays are high-energy electromagnetic radiation of wavelength range 0.01 to 10 nm. They are produced, when highly accelerated electrons hit a metal target acting as anode inside X-ray tube [112]. X-rays are diffracted by the atomic planes of a crystal and produce diffraction pattern because their wavelength λ is typically the same order of magnitude as the interplanar spacing d of a crystal.

X-ray diffraction is a standard technique to study and determine the atomic and molecular structure of a crystalline material. Therefore, it is widely used to identify various phases present in a material, relative abundances of these phases and their corresponding unit cell parameters. Every crystalline material has a distinct atomic structure and its probing with X-rays exhibit a characteristic diffraction pattern comprising of peaks. The peak positions are used to determine the unit cell parameters and the d values. These structural details are essential for identification of the elemental phases such as α-Fe (bcc) and γ-Fe (fcc).

Figure 3.6 is a schematic diagram showing Bragg's diffraction. X-rays of wavelength λ is incident on the atomic planes of a crystal with interplanar spacing d at an angle θ, the scattered X-rays serve as a mirror to the incident X-rays by a specific phase difference.

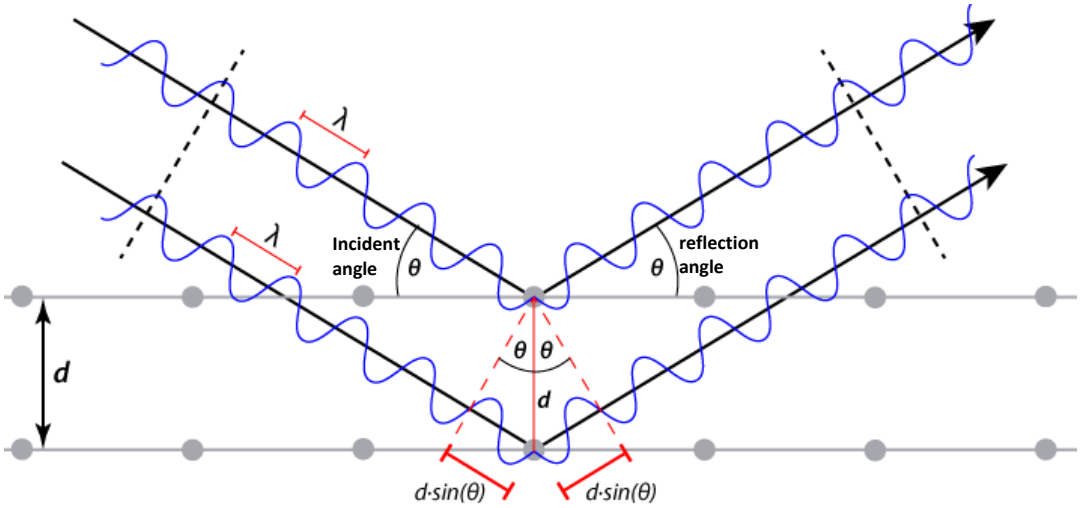

Figure 3.6: Schematic diagram showing Bragg's diffraction; Incoming X-rays of wavelength λ incident at an angle θ are diffracted from the atomic planes of a crystal with lattice spacing d and undergo constructive interference [19].

The waves elastically scattered from parallel atomic planes encounters a phase difference of multiple integer numbers of wavelengths. These waves mutually interfere constructively, and peaks formation take place in the diffraction pattern. In order to obtain a diffraction pattern as a result of constructive interference, the Bragg's condition must be satisfied:

$$2d\sin\theta = n\lambda \tag{3.1}$$

Where n is an integer and the other terms are shown in Figure 3.6.

(ii) Experimental setup and the Rietveld refinements

X-Ray powder diffraction was performed using Siemens (Karlsruhe, Germany) D5000 and Panalytical (Almelo, Netherlands) X′Pert-Pro diffractometers (both with Cu K_α radiation with $\lambda = 0.154$ nm) on powder directly extracted from roughened quartz substrates.

A schematic diagram of the diffractometer is shown in Figure 3.7. The powder material was filled in a small disc. The disc sample holder was then placed on the goniometer and

rotated by an angle θ while the X-Ray detector rotated around it on an arm at 2θ (Figure 3.7). Due to the randomly distributed crystallites in the powder material, ideally, every possible crystallographic orientation was present in equal amounts in the powder, and the resulting orientational averaging causes the three-dimensional reciprocal space to be projected in a one-dimensional 2θ-axis.

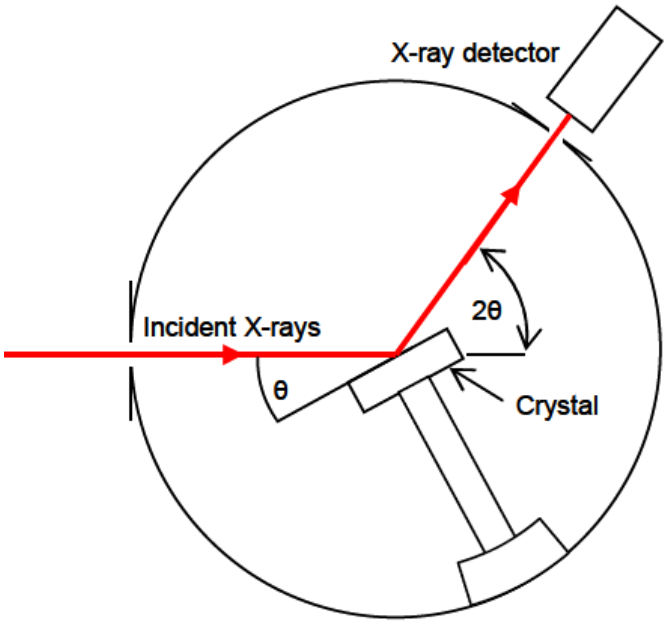

Figure 3.7: Schematic diagram of X-ray diffractometer, in which X-rays incident on the crystalline sample are Bragg reflected. The sample is rotated by θ on a goniometer and detected by the detector at 2θ [20].

Rietveld refinements [113] of the obtained X-ray diffraction data were performed using the General Structure Analysis System (GSAS) program [114] with the EXPGUI interface [115]. The GSAS program based on Rietveld refinement method, which uses the least-squares approach to fit a theoretical line profile to the diffractogram, was used to identify and estimate the relative abundances of the encapsulated phases from the area enclosed by the diffraction peaks.

The function type 1 (shifted Chebyshev polynomial) with 8-12 numbers of terms were used as background function. Also, the scaling and profile refinement were performed

to improve the quality of fit. The profile parameters were separately refined and then fixed. During the Rietveld refinement, the unit cell parameters were often refined to obtain the best possible fit and the lattice parameters values were extracted for individual encapsulated phase.

(iii) Difficulties and Limitations of Powder Diffraction

One of the characteristic features of powder diffraction is the collapse and projection of the three-dimensional reciprocal space of the individual crystallites on the one-dimensional 2θ-axis. There is a systematic overlapping of Bragg's peaks due to symmetry conditions, for example in cubic space groups. In addition, accidental overlapping also occurs due to limited experimental resolution [116]. Therefore, X-ray diffraction provides the averaged information of the crystal structure of a particular phase and cannot be used as a local probing technique such as selective area electron diffraction in TEM.

3.2.2 Electron microscopy

This subsection provides a brief description of the various electron microscopy techniques used in this work. The physical principles of these techniques are also briefly explained.

The electron microscope uses electron-beam instead of light to create an image of the specimen. In the electron microscope, a high-energy ($\sim$keV) electron-beam interacts with a thin specimen and a wide range of secondary signals are generated within the microscope column which after detection can give interesting information of the specimen (Figure 3.8). These indicated signals shown in Figure 3.8 can be detected in SEM or TEM depending on the sample thickness.

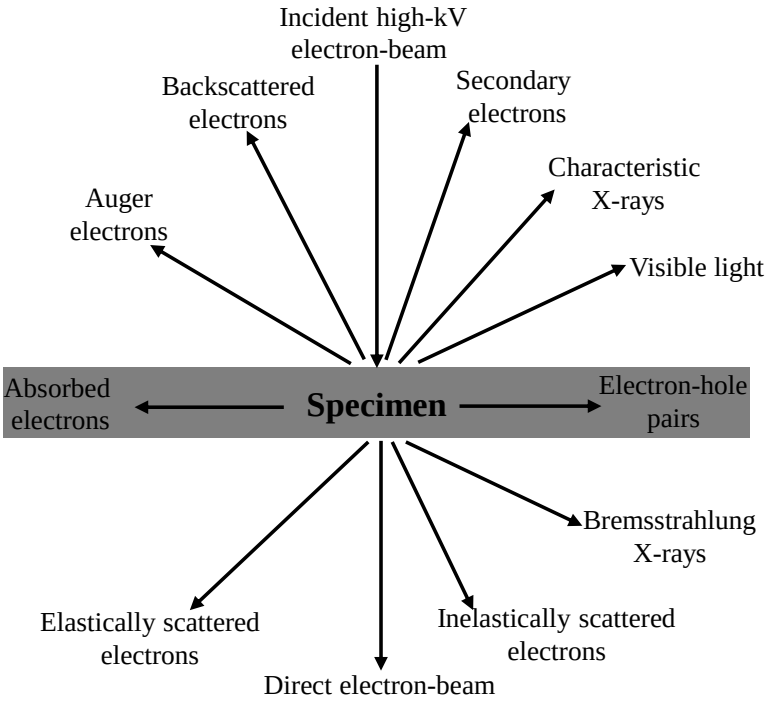

Figure 3.8: Overview of various signals generated when a high-energy electron beam interacts with a thin specimen inside an electron microscope. Most of these indicated signals can be detected in an SEM or TEM depending on the sample thickness.

For SEM investigations, the employed signals are mainly due to secondary electrons, backscattered electrons and the characteristic X-rays for energy dispersive X-rays spectroscopy. If the specimen of a complex material system is thin enough, the elastically scattered electrons can be used in a TEM to obtain not only structural information at atomic scale but also chemical and electronic information.

Scanning electron microscopy

(i) Physical principles

SEM is a technique which uses high-energy focused electron-beam. In SEM the electron-beam generated by field emission cathode- or thermal emission from heated tungsten filament is scanned over the specimen, which allows the imaging of the surface. The entire procedure is known as raster scanning and causes the beam to sequentially cover a rectangular area on the specimen. The image is built-up using detectors by mapping

the detected signals with the beam position. The energy of the electrons can be selected in the range of (100 eV to 30 keV), depending on the aim of the characterization and the type of material under investigation [117]. A schematic diagram showing the overview of the interior column of a typical SEM is provided in Figure 3.9.

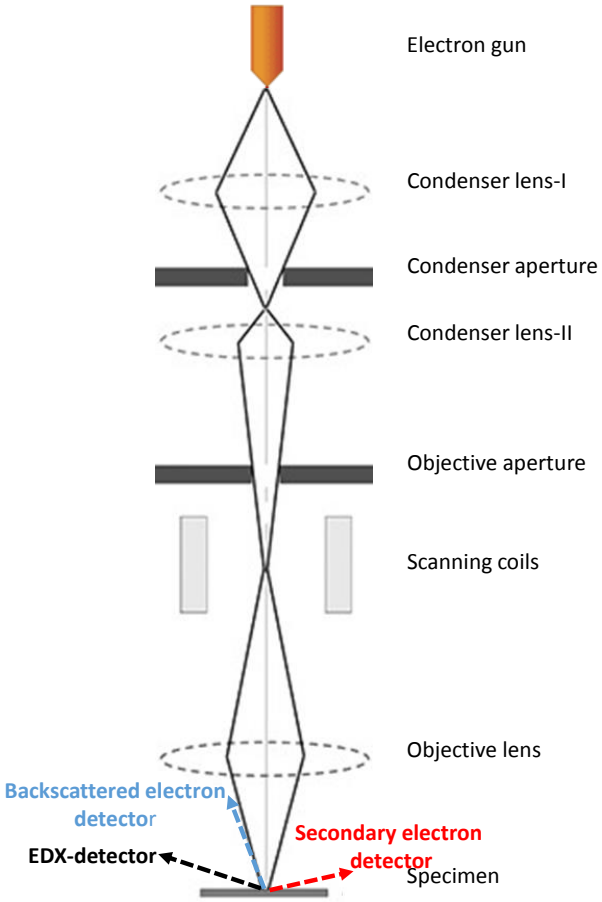

Figure 3.9: Schematic overview of the SEM column [21].

The difference in kinetic energy of the secondary and backscattered electrons are taken as an advantage in the SEM. Secondary electron imaging is a common SEM imaging mode, which uses secondary electrons (low-energy $\leq$50 eV) ejected from the specimen atoms within a few nanometers from the sample surface by inelastic scattering of electron-beam [118]. Once these secondary electrons escape from the surface of the specimen are then collected by a semiconductor (silicon) detector, for subsequent imaging the

morphology and topography of specimen. While backscattered electron imaging mode uses backscattered electrons (high-energy >50 eV) part of the incident beam which are elastically backscattered (at an angle greater than 90°) out of the specimen interaction volume as a result of interaction with the specimen atoms [118]. These electrons provide information regarding the chemical composition of the target material based on atomic-number contrast because the cross-section for high-angle elastic scattering is proportional to the square of atomic number (Z). As the energy of the backscattered electrons is high enough for the creation of electron-hole pairs in a semiconductor detector and are therefore detected and counted by the detector, thus allowing image formation on the screen [117, 119]. Typically, backscattered electron images show contrast due to variations in chemical composition of a specimen, whereas secondary electron images reflect mainly its surface topography [117].

(ii) Experimental setup

In this study, SEM investigations were performed using an FEI Inspect F microscope with accelerating voltage of 20 kV. Some of the preliminary chemical analysis were carried out using EDX-SEM, which works with the characteristic X-rays emitted from the sample atoms when the incident beam interacts with the atoms and excitation or ejection of electrons from the inner-most shells of atoms take place. The characteristic peaks in EDX-spectra correspond to the presence of particular elements identified in-terms of atomic number (Z).

(iii) Strengths and limitations of SEM

SEM is a versatile technique used for studying morphology and topography of the samples, nevertheless, it comes under limitations when a material is investigated aiming to know whether it is crystalline or amorphous. Although, SEM provides high-resolution surface imaging of the specimen with a significant thickness which is not possible with the optical microscopes because the wavelength associated with electrons in SEM is very

small compared to that of the wavelength of visible light. Due to the significant mass-thickness of the specimen and low-energy of the electron-beam, SEM is not capable to unveil the crystal structure and phase-composition of the material, because the electron beam cannot transmit through the specimen. At higher magnification, the SEM has a very limited spatial resolution. The latest SEM has an image resolution typically between 1 and 10 nm, not as good as the TEM but greatly superior to the light microscope. Moreover, SEM images have a relatively large depth of focus: specimen features that are not exactly in the plane of focus still appear sharp and distinguishable [117]. In case of non-conducting samples, static charges (electrons) are acquired on the surface of the specimen which influence the electron-beam and deteriorate the image formation. Therefore, carbon or gold coating is usually required for investigation of such type of samples.

Transmission electron microscopy

TEM is a powerful technique to investigate the morphology, crystal structure, phase and elemental composition of the nanoscale materials. In a TEM, electrons penetrate through a very thin specimen (30-50 nm) and are then imaged by the appropriate electromagnetic lenses, broadly analogous to the working principle of an optical microscope (OM). Schematic diagrams showing the comparison of TEM and OM are given in Figure 3.10.

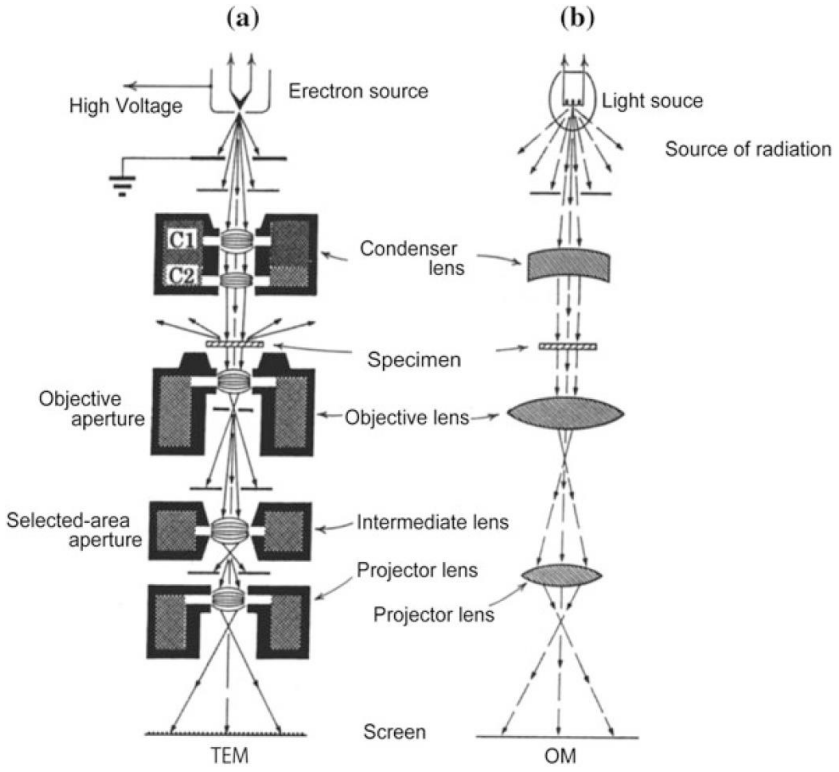

Figure 3.10: Schematic diagrams showing a comparison between a transmission electron microscope (TEM) (a) and an optical microscope (OM) (b) [22].

Resolution of the optical microscope is limited by the wavelength of visible light, therefore atomic-resolution imaging is not possible with an optical microscope. Whereas in TEM electrons being charged particles are accelerated to achieve wavelength smaller than 1 Å making it possible to obtain atomic-resolution imaging. The comparison of resolution between an optical microscope and a TEM can be understood by the Abbe's equation [22]:

$$d = 0.612\lambda/n\sin\alpha \tag{3.2}$$

where n is the refractive index and its value is 1 in the vacuum of an electron microscope, d is the resolution (minimum distance at which the points can be distinguished as individuals), α is the half angle of the cone of light from specimen plane received by the objective (half aperture angle in radians) and λ is the wavelength of the imaging

radiation.

As the wavelength range of visible light is between 400 nm to 700 nm. Therefore, the maximum image resolution that can be obtained by light microscopes is about 200 nm. In case of electrons, the associated wavelength (λ) proposed by Louis de Broglie, which is approximately equal to:

$$\lambda = h/\sqrt{2meV} \tag{3.3}$$

where h is Planck's constant (6.626x10^{-34} J seconds), m is the mass of an electron (9.1x10^{-31} kg), e is the charge of an electron (1.6x10^{-19} coulombs) and V is the accelerating voltage. By considering the relativistic effects, the wavelength of an electron at 100 keV, 200 keV, and 300 keV operating voltages in electron microscopes can be calculated as 3.70 pm, 2.51 pm and 1.96 pm, respectively. Thus, the sub-angstrom level resolution is achievable with the TEM. Practically, TEM resolution is limited to $\sim$1 Å= 0.1 nm due to various factors, such as the lens aberrations in electron microscopes, and the requirement of a very thin sample, the drift and the vibrations experienced by the TEM specimens under the electron-beam, etc.

(i) Bright-field and dark-field imaging

Bright-field imaging is the conventional imaging mode for TEM, in which an electron-beam is transmitted through a specimen for the image formation, Figure 3.11 (A). The formation of image results from weakening of the direct beam by its interaction with the atoms of the exposed specimen [23]. Therefore, mass-thickness and diffraction contrast contribute to the formation of an image.

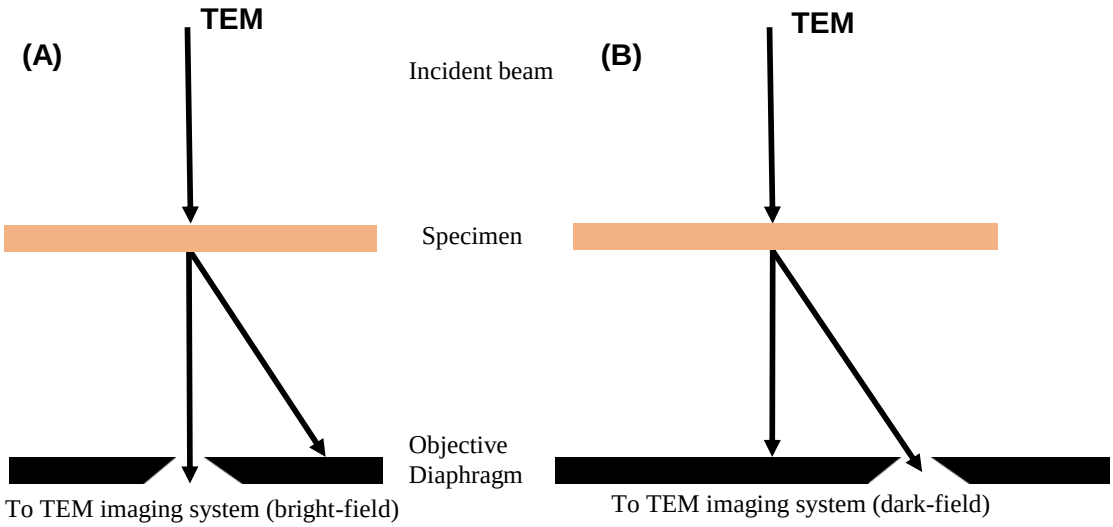

Figure 3.11: Comparison of the use of an objective aperture in TEM to select (A) the direct or (B) the scattered electrons forming bright field (BF) and dark field (DF) images respectively [23].

In dark-field imaging mode, the directly transmitted beam is blocked by the horizontally displaced objective aperture while one or more diffracted beams are allowed to pass through the objective aperture , Figure 3.11 (B). The strongly diffracting regions of specimen appear bright relative to their surroundings, thus forming a dark-field image where any part of the field of view that contains no specimen appears dark [23, 117]. The detailed theoretical description on the formation of bright- and dark-field images can be found in several textbooks [23, 117].

(ii) Electron diffraction

The elastic scattering (deflection) of electrons due to the Coulomb field of atomic nuclei in a crystalline material is called as electron diffraction [117]. The electron diffraction occurs as the electron beam is diffracted by the crystal lattice at specific angles and a diffraction pattern is yielded, which is a characteristic of the crystalline material under investigation.

The distances between the diffraction spots in a diffraction pattern correspond to the interplanar spacing in the crystalline material and is given by the Bragg's law:

$$2d\sin\theta = n\lambda \tag{3.4}$$

Where λ is the wavelength of the electrons, θ is the angle of incidence with respect to a set of crystallographic planes, d is the interplanar spacing of the atomic planes and constructive interference occurs when n is an integer. Using the values of θ and d with the presence or absence of certain reflections, the crystal structure, phase and orientation of a specimen can be identified. In case of polycrystalline materials, the collection of diffraction spots yield rings centered on a bright central spot that represents the undiffracted electrons. The radii of these rings can also be used to identify the material investigated, as they correspond to particular atomic planes.

Selective area electron diffraction (SAED) is a local probing technique based on electron diffraction that limits the exposed region of the material under the electron beam by using a specific diameter selective area aperture. This gives information about the crystal structure and the particular phase of the material in that specific location of interest which is probed. In case of HRTEM, the fast Fourier transform taken from the selected region of the image is equivalent to selective electron diffraction pattern.

The electron beam intensity used throughout this study was 60-120 pA cm^{-2}. SAED patterns were taken with the lowest selective area aperture of 10 μm, which corresponds to an in image-plane area of diameter 160 nm; SAED patterns along different zone axes were obtained by tilting the samples in the range of -25° to +25°.

(iii) Sample preparation and experimental setup

TEM specimens were prepared by ultrasonication of the as-produced powder of radial structures in ethanol and pipetting to carbon-coated holey copper grids. The ultrasound conditions were selected to produce detachment of the radial nanotubes from the central particle to facilitate TEM access to the full length of the encapsulated nanowire.

In order to investigate phase composition and junctions between different phases in the encapsulated nanowires, Bright-field and dark-field TEM images and selective area electron diffraction (SAED) patterns were collected using a Jeol JEM 2010 transmission electron microscope operated at accelerating voltage of 200 kV.

(iv) Limitations

TEM is quite a large instrument and very expensive as compared to SEM. Imaging and diffraction in TEM is limited to sample thickness. Unless the specimen is made very thin, electrons are strongly scattered or even absorbed in the specimen, rather than being transmitted. Secondly, with TEM only two-dimensional images of the specimen are produced whereas SEM produces three-dimensional images of the specimen. The TEM images are in black and white.

Scanning transmission electron microscopy

STEM in a TEM is now a routine high-resolution technique, which can be operated both in transmission and scanning imaging mode. A typical STEM is a conventional TEM equipped with additional scanning coils, detectors and necessary circuits, which allows it to switch between the STEM and conventional TEM. However, dedicated STEMs are also manufactured which only works in scanning mode [23].

(i) High-angle annular dark-field imaging

STEM imaging mode uses the elastically scattered electrons [23]. These electrons are scattered at an angle θ and are detected by either a bright field (θ <10 mrad) or annular dark field (10 mrad< θ < 50 mrad) (ADF, usually a ring-shaped scintillation detector to which a photomultiplier is attached) detector, as shown in Figure 3.12 [23]. For electrons scattered to high-angles (θ >50 mrad), the intensity is nearly proportional to the square of the atomic number (Z), so that the strong chemical contrast (Z-contrast) is obtained. This type of imaging is known as a high-angle annular dark field (HAADF) [120]. The main advantage of HAADF-STEM imaging mode, over the ADF and BF is to avoid

the Bragg effects, because the HAADF detector only collects those electrons which are scattered at very high angles (θ >50 mrad). Therefore, the strength of scattering is not strongly influenced by diffraction. STEM imaging is useful if the specimen is beam sensitive such as organic nanomaterials because the beam scans over the specimen in a raster pattern and avoiding long time exposure of the specimen [121]. Therefore, a scanning beam allows you to precisely control the irradiated region of the specimen and it is a form of low-dose microscopy [23, 122].

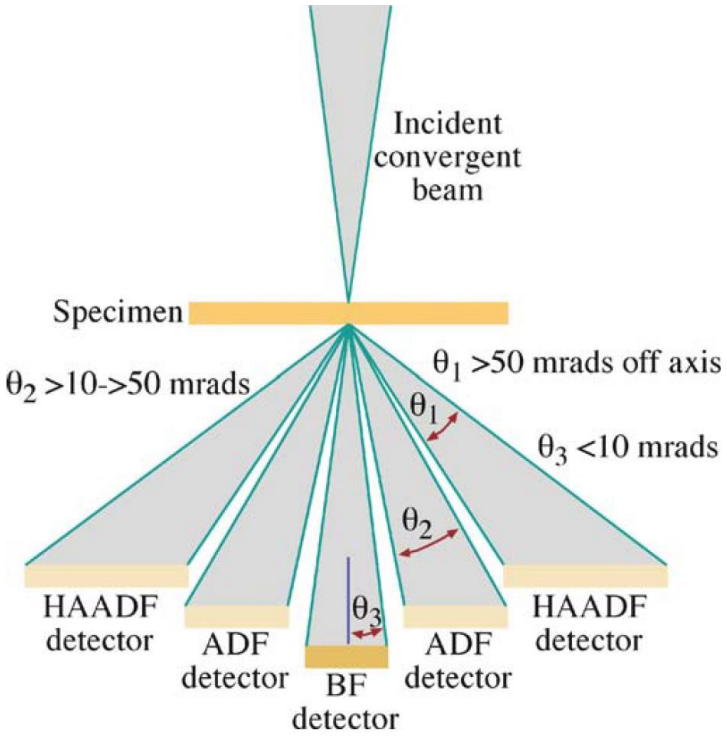

Figure 3.12: Schematic of the HAADF detector setup for Z-contrast imaging in a STEM. The conventional ADF and BF detectors are also shown along with the range of electron scattering angles gathered by each detector [23].

(ii) Energy dispersive X-ray spectroscopy

The beam scanning of the specimen in a raster pattern makes STEM suitable for analytical techniques such as Z-contrast annular dark-field imaging, and spectroscopic mapping by energy dispersive X-ray (EDX) spectroscopy. EDX uses the characteristic X-rays emitted from the sample atoms during the bombardment by an electron beam to charac-

terize the elemental composition of the exposed volume of the specimen. The presence of elements with an atomic number between 4 (Be) and 92 (U) can be analysed and mapped with this technique.

(iii) Experimental set-up

High-resolution transmission electron microscopy was performed on a double aberration-corrected FEI-QU-Ant-EM, using accelerating voltage of 120 kV. Energy dispersive X-ray spectroscopy was performed using FEI-X-Ant-EM equipped with highly efficient Bruker EDX system with a collection solid angle close to 1 Sr. High-angle annular dark field (HAADF) imaging were carried out on a double aberration-corrected FEI-QU-Ant-EM in scanning mode, using accelerating voltage of 120 kV.

Programs and software

The image acquisition and processing software for analysis of images and diffraction patterns, used in all the TEM investigations were Gatan Digital Micrograph, ImageJ, CrystalMaker, CrystalDiffract and SingleCrystal.

3.2.3 Magnetisation

(i) SQUID Magnetometer

A SQUID in combination with the MPMS is one of the most sensitive device for measuring magnetic properties. This instrument is capable to detect incredibly small magnetic field in the sample and is able to directly determine the overall magnetic moment of a sample in absolute units [24, 123].

Figure 3.13 shows a schematic diagram of the SQUID magnetometer. The SQUID consists of two superconductors separated by thin insulating layers to form two parallel Josephson's junctions, blue in Figure 3.13.

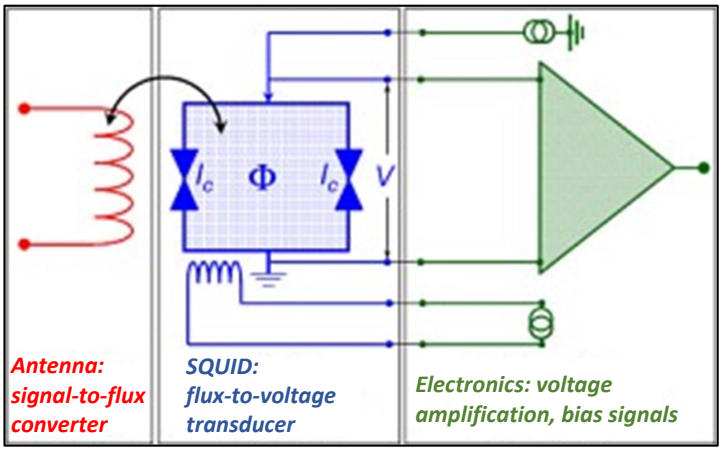

Figure 3.13: Schematic diagram of the MPMS SQUID magnetometer showing antenna: signal-to-flux converter, SQUID: flux-to-voltage converter, and the electronics for voltage amplification [24].

In Figure 3.14, a typical response curve shows the induced voltage between the two junctions as a periodic function of the change in position of the sample with respect to the pick-up coil shown in Figure 3.15 [24].

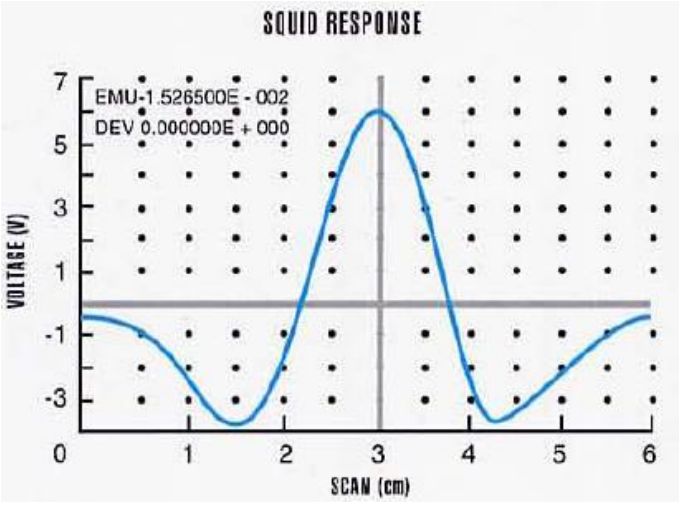

Figure 3.14: Schematic of the superconducting pick-up coil with 4 windings [24].

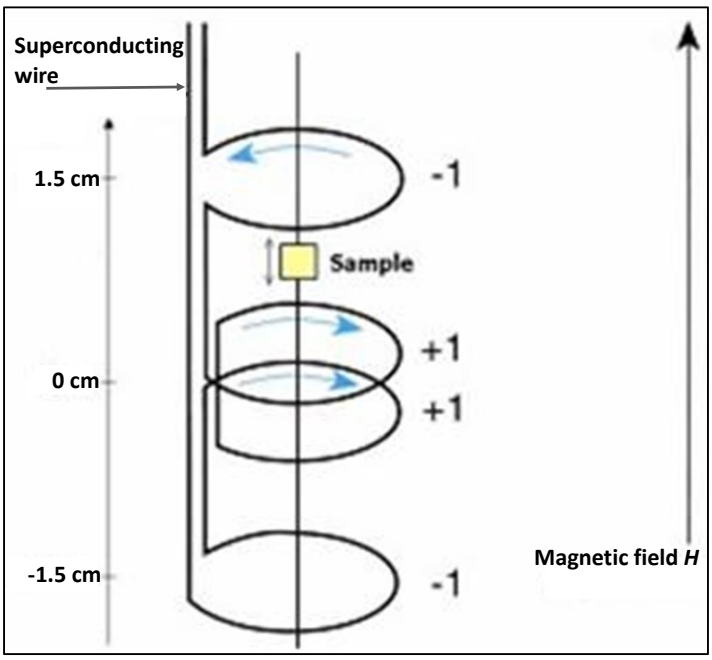

Figure 3.15: Schematic of the superconducting pick-up coil with 4 windings [24].

The SQUID works as a magnetic flux-to-voltage converter (blue in Figure 3.13), therefore, the variations in magnetic flux $\Delta\Phi$ through a SQUID antenna (red in Figure 3.13) in the pick-up coils produces corresponding variations in the SQUID output voltage V. This voltage is then amplified and read out by the magnetometers electronics (green in Figure 3.13). In principle, the obtained voltage is proportional to the magnetic moment of the sample. In a fully calibrated system, measurements of the voltage variations from the SQUID detector when a sample is moved through the pick-up coils provide a highly accurate measurement of the sample's magnetic moment. The sensitivity of the MPMS-7, as declared by the manufacturer Quantum Design, is 10 to 7 emu [24, 123].

SQUID magnetometer MPMS-7 (Quantum design) allows two types of measurements in the -1.0 Tesla to 1.0 Tesla range of magnetic fields and 1.75 K to 400 K temperature range:

1. Measurements of the magnetisation M of the sample as a function of magnetic field H at a given temperature T

2. Measurements of the magnetisation M of the sample as a function of temperature T at a given magnetic field H.

(ii) Magnetization measurements

The magnetization measurements were performed on powder of radial structures removed from a roughened quartz substrate using a SQUID magnetometer MPMS-7 (Quantum design) as function of magnetic field and temperature in the range 5 K to 300 K. For zero-field-cooled (ZFC) measurements, the sample was cooled in zero magnetic field from room temperature to 5 K. The field-cooled (FC) measurements were performed under a magnetic field of 100 Oe during cooling from 300 K to 5 K.

Chapter 4

Results and Discussion-I

4.1 Synthesis and microstructural analysis of low and high γ-Fe-content nanowires

The aim of this work is to first reproduce the low γ-Fe-content (15%) nanowires achieved by Boi *et al.* [10], and to analyse the spatial distribution of encapsulated phases. The second aim is to achieve higher γ-Fe-content nanowires and to perform microstructural analysis of the spatial distribution of phases and α-Fe/γ-Fe junctions.

4.1.1 Low γ-Fe-content nanowires

Firstly, powder of self-organized radial structures with low γ-Fe-content nanowires was reproduced using the recently reported boundary layer chemical vapour synthesis route [10].

The pre-synthesis and post-synthesis scanning electron micrographs of the substrates (see insets) are presented in Figure 4.1 (A-B). The rough surface of the substrate shown in Figure 4.1 (A) is covered with the ensembles of radial structures deposits shown in Figure 4.1 (B).

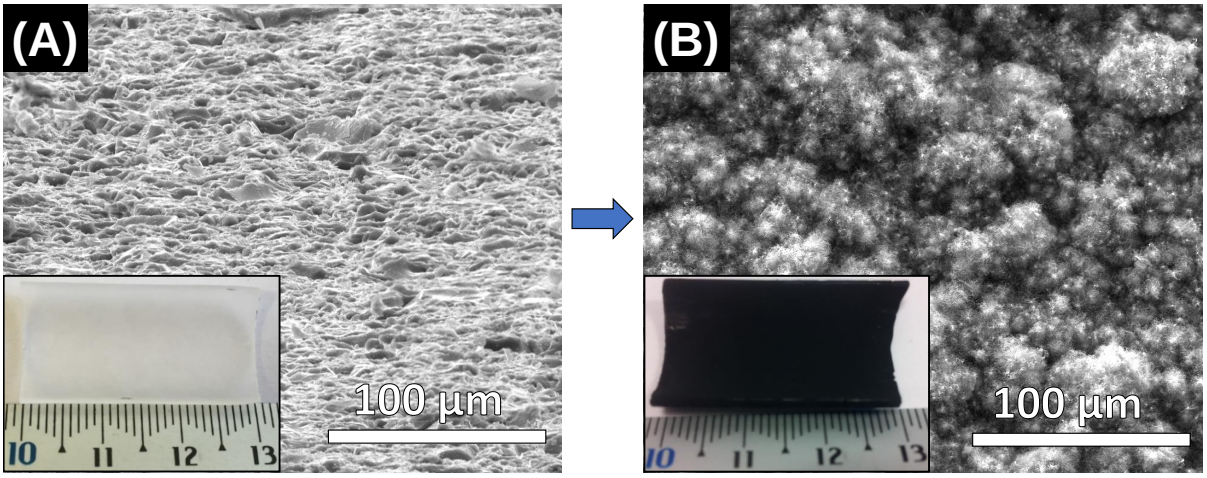

Figure 4.1: (A-B) Scanning electron micrographs of a quartz substrate before and after the synthesis. (A) is the SEM image showing the rough surface of the quartz substrate presented in the inset before synthesis. (B) showing the ensemble of radial structures deposited on the substrate shown in the inset after synthesis.

Further detail view of the as-grown radial structure deposits on a roughened quartz substrate taken out of the reactor is presented in Figure 4.2.

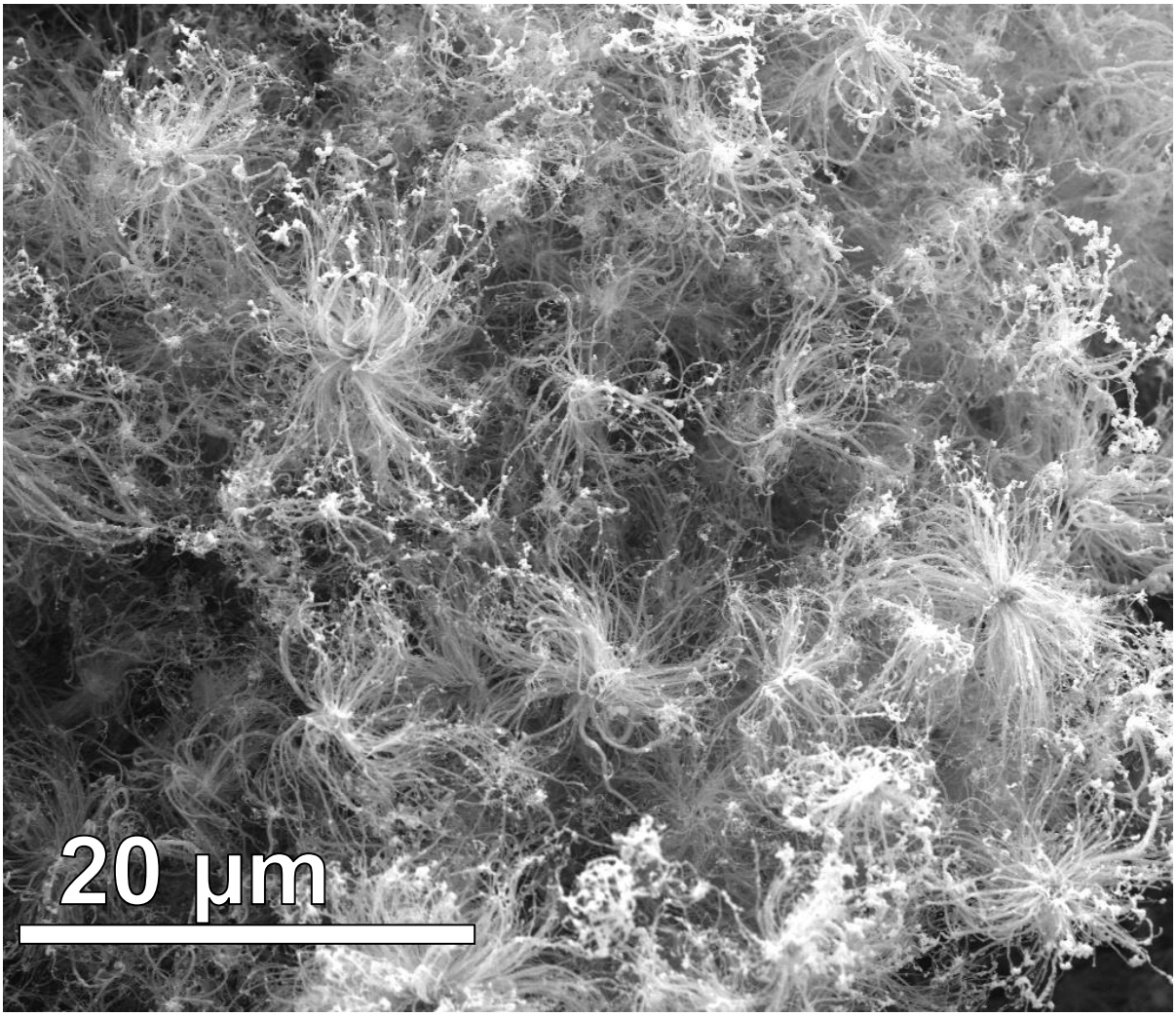

Figure 4.2: Scanning electron micrograph of an ensemble of radial structures deposited on the roughened quartz substrate.

A typical example of the individual radial structure is shown in Figure 4.3. This high magnification SEM image shows the radial carbon nanotubes departing from a central particle. The average diameter of a typical radial structure is ~ 11 μm. The thickness of the deposited layer on the substrate is several times the diameter of an individual radial structure. The deposited powder can be easily removed magnetically or mechanically and can readily be dispersed in ethanol or other solvents for further characterisations. The observed morphology is in agreement with that reported by Boi *et al.* [10].

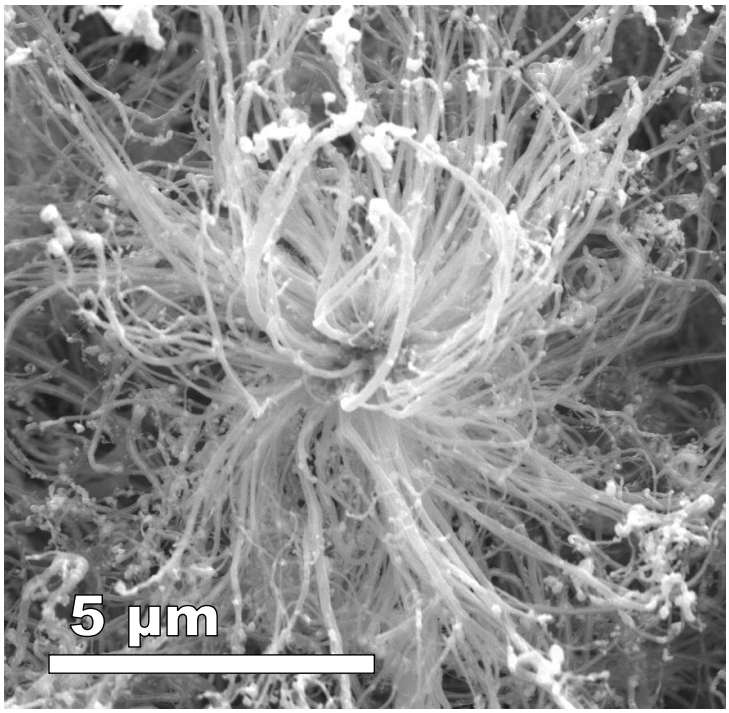

Figure 4.3: Scanning electron micrograph of a typical individual radial structure [1].

X-ray diffractogram obtained from powder extracted from the substrate is presented in Figure 4.4. The Rietveld refinement was performed using the General Structure Analysis System (GSAS) program with the EXPGUI interface to identify and estimate the relative weight abundances of the encapsulated phases [113–115].

In X-ray diffractogram (Figure 4.4), 110 is a characteristic peak of α-Fe (bcc) at $2\theta \sim 44.67°$ and 111 is a characteristic peak of γ-Fe (fcc) at $2\theta \sim 43.61°$ respectively. The relative weight abundances of the various encapsulated single crystal phases α-Fe with space group ($Im\bar{3}m$), γ-Fe space group ($Fm\bar{3}m$) and Fe_3C space group ($Pnma$) extracted from the X-ray diffraction data (Figure 4.4) after Rietveld refinement are summarised in Table 4.1.

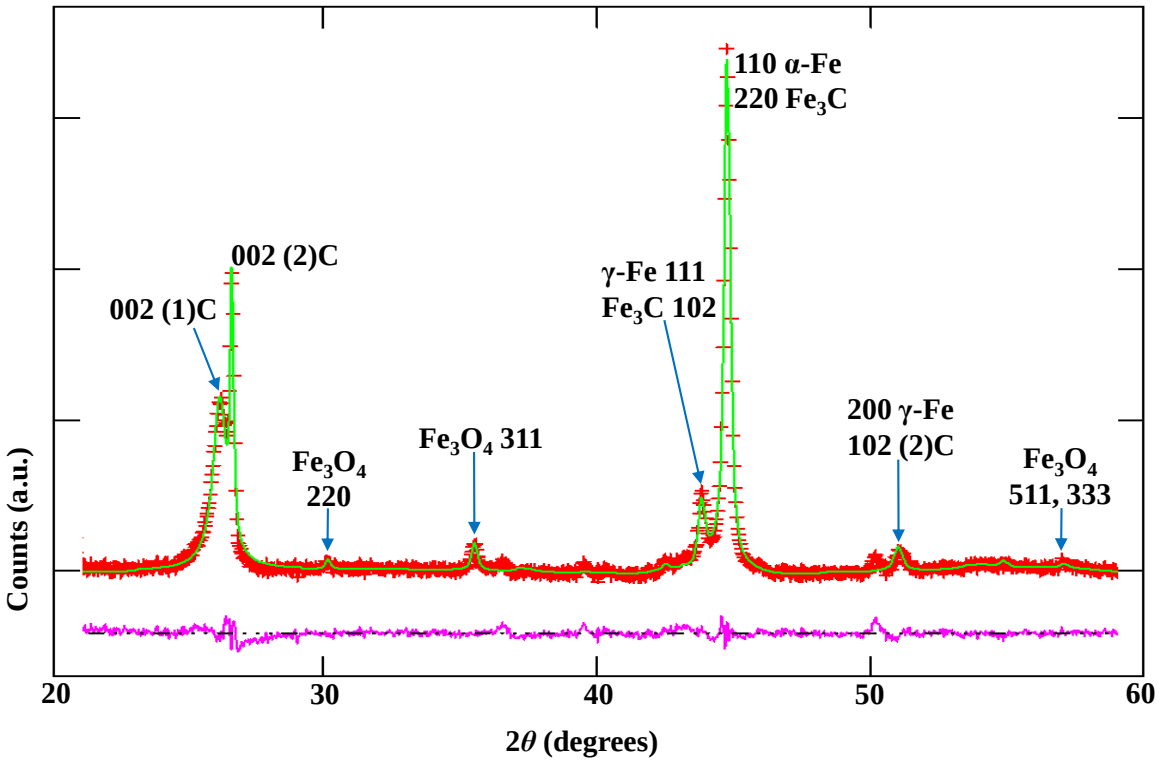

Figure 4.4: Typical X-ray diffractogram data (red), Rietveld refinement (green), and difference (purple) for a powder extracted from the reactor. Arrows denote the crystal planes attributed to each intensity peak. The encapsulated phases were analysed in terms of the following components of α-Fe ($Im\bar{3}m$, Crystal Open Database Ref. 1100108), γ-Fe ($Fm\bar{3}m$, Crystal Open Database Ref. 9008469), and Fe_3C ($Pnma$, Crystal Open Database Ref. 16593). The relative weight abundances of these phases are 75% of cubic α-Fe, 15% cubic γ-Fe and 10% of orthorhombic Fe_3C. The cubic Fe_3O_4 (space group $Fd\bar{3}m$, ICSD Chemical Database Ref. 84098) content results from spontaneous oxidation of non-encapsulated iron particles when the powder is handled in air, this constitutes less than ten percent of the total sample weight. The lower angle graphitic carbon peak, (1)C, corresponding to the 002 reflection from graphite (space group $P6_3/mmc$, ICSD Chemical Database Ref. 53781), originates from reflections from the graphitic walls of the multiwall carbon nanotubes, inter-wall spacing 0.34 nm. The second graphitic peak, (2)C, corresponds to the lattice spacing 0.33 nm (002 peak of graphite hexagonal $P6_3/mmc$, ICSD Chemical Database Ref. 52230) of the graphitic shell of the spherical particles that comprise the core of the radial structures, [10].

Substrate-temperature	Relative abundance (wt.%)		
	α-Fe ($Im\bar{3}m$)	γ-Fe ($Fm\bar{3}m$)	Fe_3C ($Pnma$)
921 °C	75	15	10

Table 4.1: Summary of the relative abundances of the encapsulated phases, extracted from the Rietveld refinement of the X-ray diffractogram in Figure 4.4.

The observation of these phases have been frequently reported in the vertical-aligned surface-grown as well as in radial carbon nanotube structures [9, 10, 33, 35, 42, 91, 124–128]. The presence of oxides is because of spontaneous oxidation of non-encapsulated elemental iron traces on the exterior of the nanotubes due to post-synthesis handling of the sample in air [1, 10] . Therefore, the corresponding peaks of oxides have been refined and indexed in the X-ray Diffractogram (Figure 4.4). In addition, the lower angle graphitic carbon peak 1(C) corresponds to the 002 reflection from the graphitic walls (inter-wall spacing of 0.34 nm) of the multiwall carbon nanotube and the higher angle peak 2(C) corresponds to the 002 reflection (inter-wall spacing of 0.33 nm) from the graphitic shell around the spherical Fe_3C nanoparticles of which the core of the radial structures is composed [10].

The high relative abundance of ferromagnetic α-Fe (75%) depicts more stability of this phase at room temperature compared to other encapsulated phases. According to Fe-C phase diagram, the mainly present iron phases above 727 °C, are γ-Fe and Fe_3C. Upon cooling, the majority of γ-Fe is transformed into α-Fe and Fe_3C. Fe_3C in contact with the nanotube walls further decomposes into graphitic carbon and the α-Fe in the core of the nanotube [12]. Therefore, a relatively low relative abundance of Fe_3C has been observed in the radial structures. It is important to mention that the measured Fe_3C content (10 %) in the radial structures sample contributes towards the spherical Fe_3C nanoparticles comprising the core as well as its spatial distribution in the encapsulated nanowires.

The retained γ-Fe (15 %) at room temperature which in bulk is a high-temperature and high-pressure phase and is unstable at room temperature, has been frequently attributed to the pressure-induced encapsulation or elastic confinement of the carbon nanotubes in the literature for more than a decade [15, 48, 49]. However, the presence of encapsulated γ-Fe at room temperature requires detail investigation and will be discussed in section 4.2 of this Chapter.

Figure 4.5 (A) shows a scanning electron micrograph of Fe-based nanowires encapsulated by MWCNTs, taken from a radial structure. In fact, the recorded peaks in EDX spectra (see Figure 4.5 (B)) confirms the presence of carbon and iron. The Si peak in the spectra is likely to originate from either the quartz substrate or the X-ray detector itself.

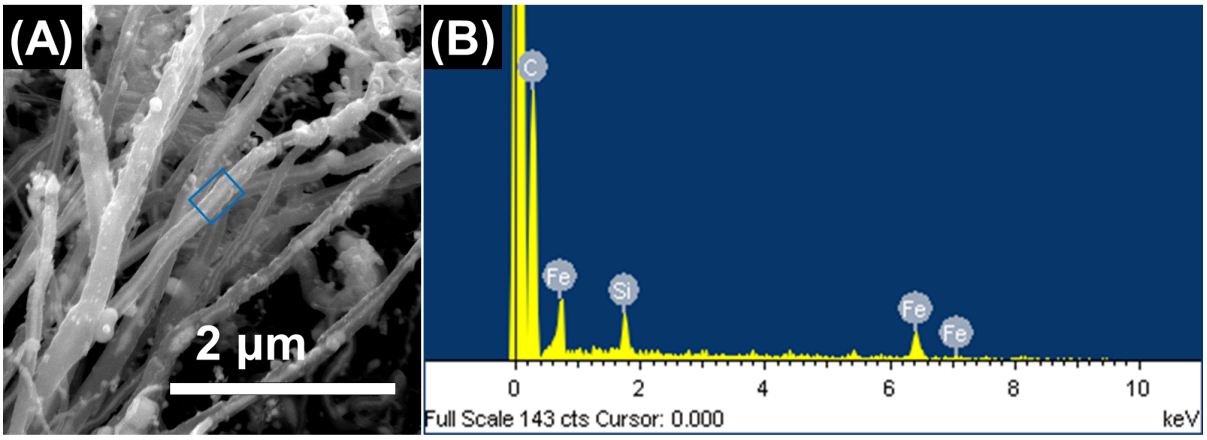

Figure 4.5: (A) Scanning electron micrograph of the encapsulated Fe-based nanowires, (B) is the corresponding energy dispersive x-ray spectra (EDX) of the region within the blue rectangle in (A). The Si peak in the spectra originates from the quartz substrate.

Unlike the vertically aligned structures, we frequently encountered high volume fraction of continuous Fe-based nanowires encapsulated by MWCNTs under transmission electron microscope. Long continuous nanowires are useful for probing the spatial distribution of the encapsulated phases and the junction formation between two phases. A typical transmission electron micrograph of the ultrasonicated radial structures showing micrometers long Fe-based nanowires encapsulated by multiwalled carbon nanotubes detached from the central core of the radial structure is provided in 4.6.

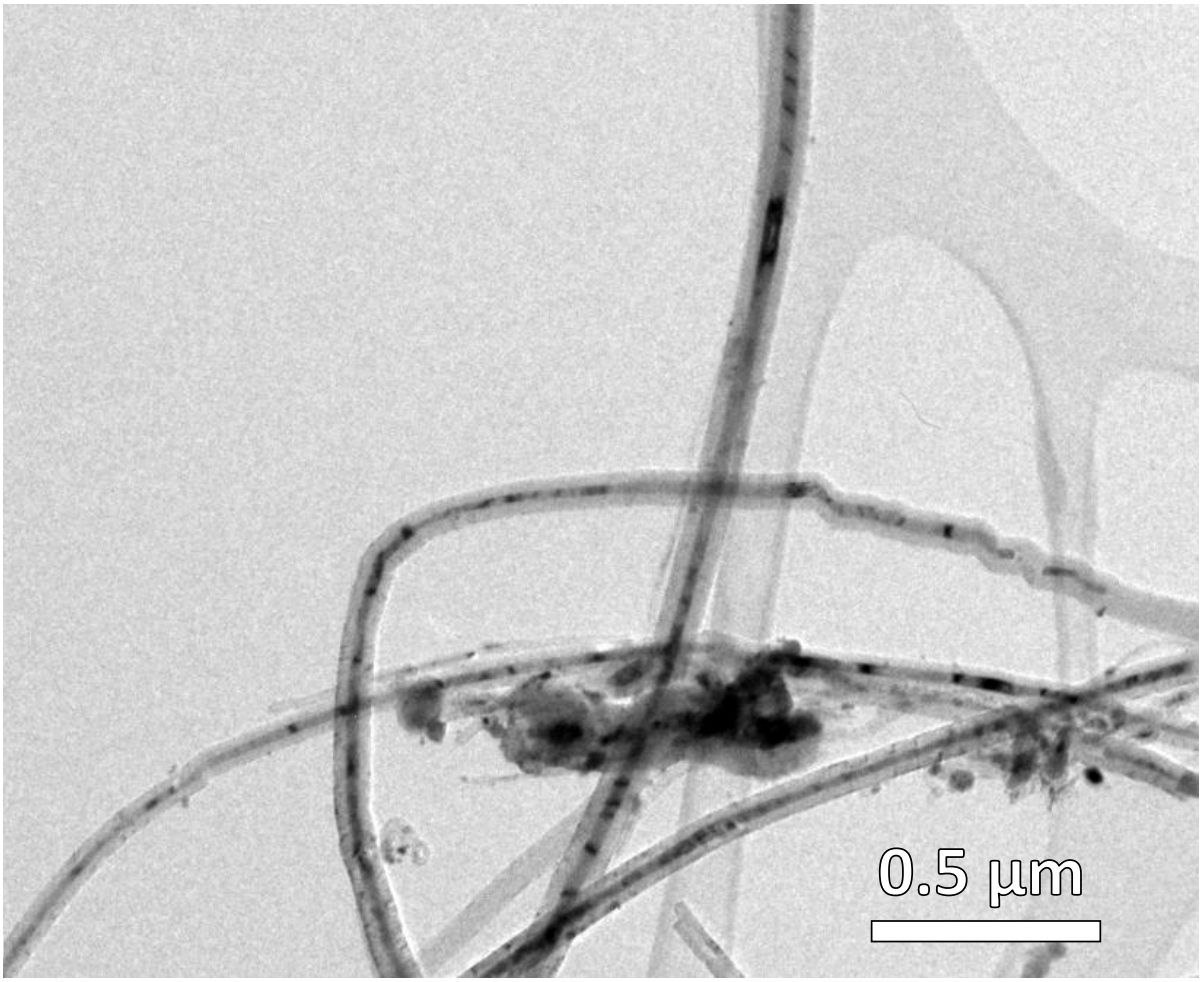

Figure 4.6: Transmission electron micrograph showing the micrometer long Fe-based nanowires encapsulated by multiwalled carbon nanotubes detached from a radial structure.

Here we are present few examples of characterized Fe-based nanowires to show the crystallinity of these nanowires system. These encapsulated nanowires detached from the central particle of the radial structues are radomly selected under TEM.

Continuous α-Fe nanowires

An example of the 6 μm long continuous α-Fe nanowire encapsulated by MWCNTs is presented in Figure 4.7. The nanowire has been probed under TEM by obtaining selective area electron diffraction patterns from 160 nm diameter areas within the broken circles (A-D). The zone axis identified in each of the diffraction patterns is α-Fe $[111]_{\mathrm{bcc}}$. The doubling and streaking of the 002_{C} reflections originating from the graphitic nanotube

walls is likely to be a consequence of the irregular outer diameter of the nanotube at these positions.

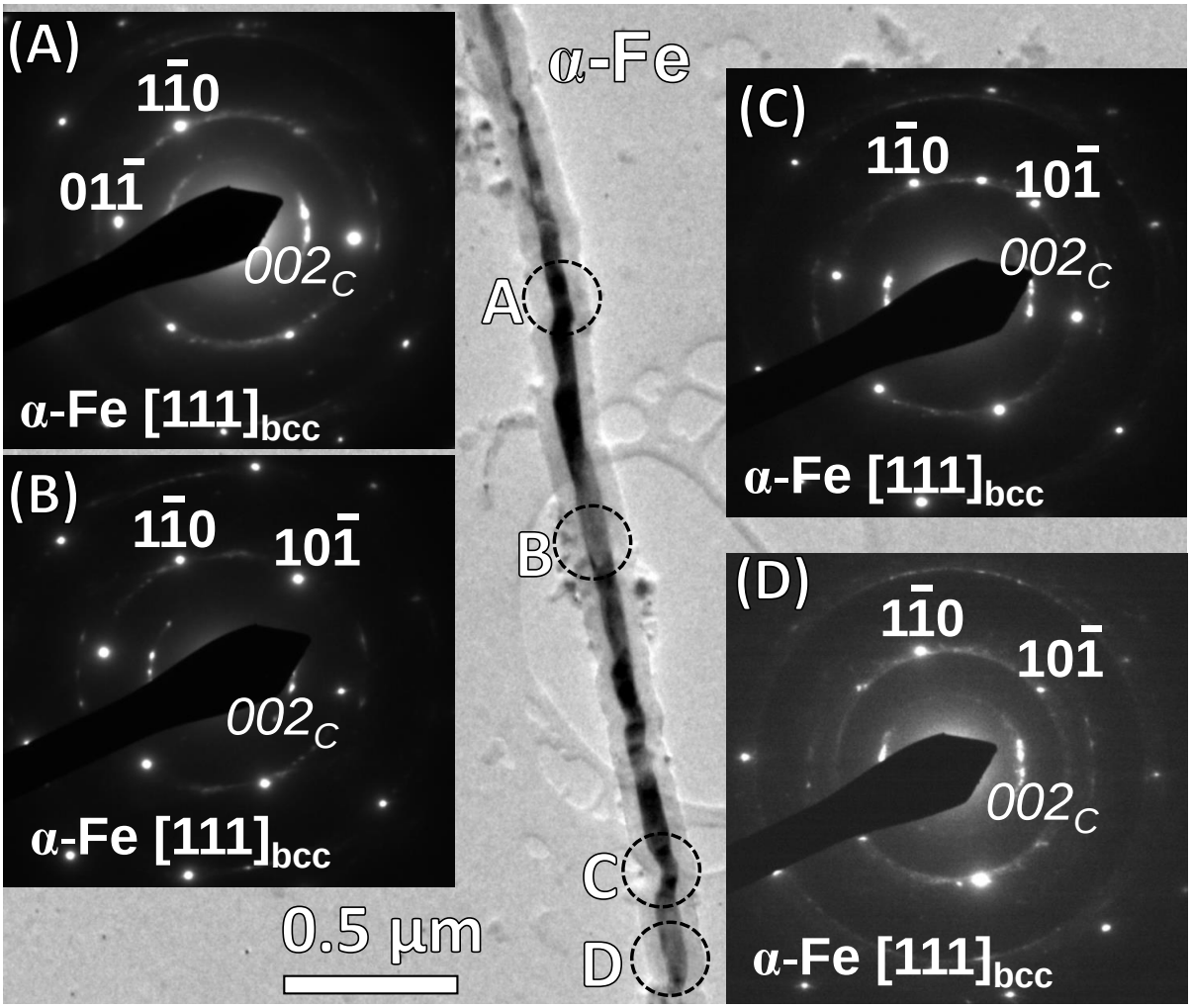

Figure 4.7: Transmission electron micrograph showing 6 μm long continuous α-Fe nanowire encapsulated by MWCNTs. The selective area electron diffraction patterns (A-D) are taken from the 160 nanometer image-plane areas indicated by the broken circles (A-D). The identified zone axis in each of the diffraction pattern is α-Fe $[111]_{\mathrm{bcc}}$. The 002_{C} indicates the reflection from the graphitic layers of multiwall carbon nanotubes.

In a second example, SAED patterns were obtained from 160 nm diameter areas centred on the three points A-C separated by $\sim$ 100 nm along the length of a continuous α-Fe crystallite, Figure 4.8 (A-C).

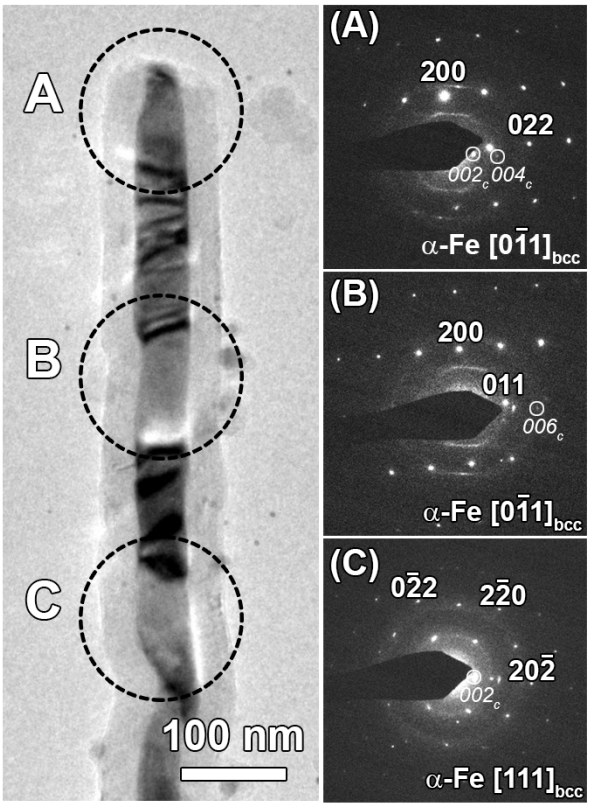

Figure 4.8: Transmission electron micrograph of an encapsulated α-Fe nanowire showing a slight variation in crystallographic orientations relative to the nanotube axis. The SAED patterns were obtained with smallest selective area aperture at three consecutive points close to the tip of a radial nanotube, upper left; the image-plane electron beam area of diameter 160 nm is indicated by the broken circle centred on the point. The highlighted zone axes are indicated in each figure: (A) α-Fe $[0\,\bar{1}1]_{\mathrm{bcc}}$, (B) α-Fe $[0\,\bar{1}1]_{\mathrm{bcc}}$, and (C) α-Fe $[111]_{\mathrm{bcc}}$. The orientation of the (110) planes are approximately parallel relative to the $002_{\,\mathrm{C}}$ planes and the nanotube axis. The reflections labelled $002_{\,\mathrm{C}}$ and $004_{\,\mathrm{C}}$ are from the graphitic carbon walls of the encapsulating nanotube; the inter-wall spacing calculated from these reflections is the one typical for the inter-planer separation in graphite, namely 0.34 nm, and agrees with that calculated from the Bragg peak labelled 1(C) in Figure 4.4.

Figure 4.8 (A-C) shows differing crystallographic orientations exhibited by the α-Fe nanowire relative to the nanotube axis. The identified zone axes are: (A) $[0\,\bar{1}1]$, (B) $[0\,\bar{1}1]$ and $[111]$. In SAEDs Figure 4.8 (A-B), the orientation of the (110) planes relative to the nanotube axis are approximately parallel to the $002_{\,\mathrm{C}}$ reflections of the graphitic walls of the multiwall nanotube. In SAED Figure 4.8 (C), the $(20\bar{2})$ planes are also nearly parallel to the $002_{\,\mathrm{C}}$ reflections and the nanotube axis.

Another TEM image showing an α-Fe nanowires with crystal planes exhibiting a slight twist in the crystallographic orientations relative to the nanotube axis indicated by $002_{\,C}$ (Figure 4.9 (A-B)).

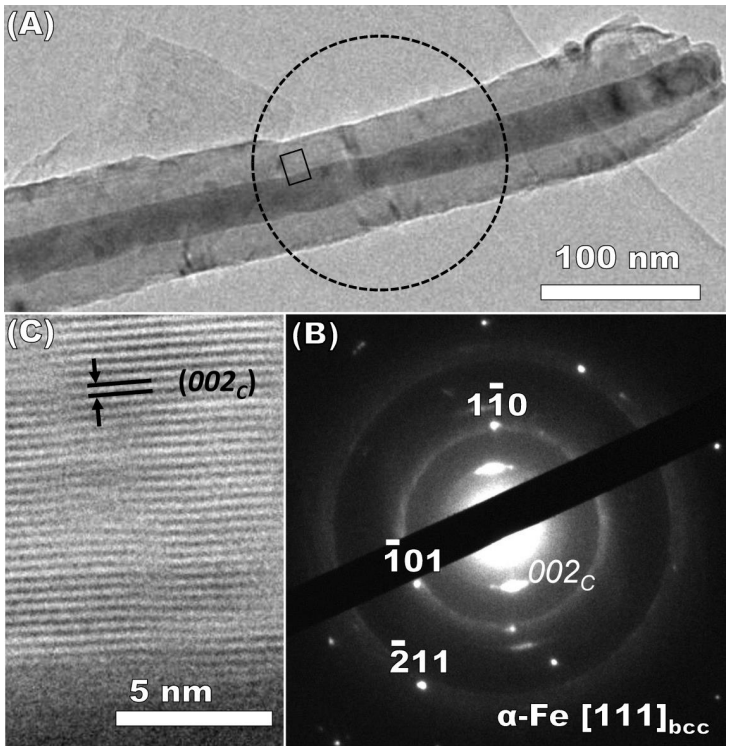

Figure 4.9: (A) Transmission electron micrograph of an encapsulated α-Fe nanowire exhibiting a slight twist in the crystallographic orientation relative to the nanotube axis. (B) The selective area electron diffraction pattern was obtained using smallest selective area aperture with image-plane area of diameter 160 nm is indicated by the broken circle in (A). The highlighted zone axis is indicated as α-Fe $[111]_{\mathrm{bcc}}$ with space group ($Im\bar{3}m$). The orientation of the $(1\,\bar{1}0)$ plane is roughly parallel relative to the $002_{\,C}$ plane and the nanotube axis The reflection labelled as $002_{\,C}$ is from the graphitic carbon walls of the encapsulating nanotube; the inter-wall spacing of 0.343 nm was calculated from $002_{\,C}$ reflections corresponds to a typical inter-planner separation in graphite, and agrees with that calculated from the Braggs peaks labelled as 1(C) in Figure 4.4. The $002_{\,C}$ inter-planer spacing is indicated in the HRTEM image in (C) taken from the area within the small rectangle inside the broken circle. The α-Fe reflections from $(1\,\bar{1}0)$ plane correspond to the lattice spacing of 0.203 nm and $(\bar{2}11)$ correspond to 0.118 nm.

The selective area electron diffraction pattern (Figure 4.9 (B)) of the nanowire has been taken with a low index zone $[111]_{\mathrm{bcc}}$ form the region within the broken circle shown in Figure 4.9 (A). The $(1\,\bar{1}0)$ crystal planes are approximately parallel to the graphitic layers of the nanotube shielding the nanowire. An HRTEM image of these graphitic layers

indexed with 002_{C} is presented in Figure 4.9 (C) coressponds to the lattice spacing 0.343 nm and agrees with the 002 reflection denoted by 1(C) in X-ray diffractogram (Figure 4.4).

Continuous Fe_3C nanowires

A typical encapsulated Fe_3C nanowire encountered under TEM also revealed variations in the crystallographic orientations after probing at three different locations. The insets provide selective area electron diffraction patterns obtained from the regions within the broken circles shown in Figure 4.10(A-C). Inset (A) is the diffraction pattern with an identified zone axis of $[\bar{1}\bar{3}2]$. The $(\bar{1}11)$ crystal planes are oriented parallel to the nanotube axis and the graphitic layers of the MWCNTs indicated by 002_{C}. A change in crystallographic orientation is followed from the diffraction patterns taken at point (B) and (C) shown in Figure 4.10. Insets (B-C) are the low index zone diffraction patterns each identified with a zone axis $[0\,\bar{1}0]$. Now the $[00\,\bar{1}]$ crystal planes are oriented parallel to the nanotube axis indicated by 002_{C} reflection from the parallel graphitic layers of the carbon nanotubes.

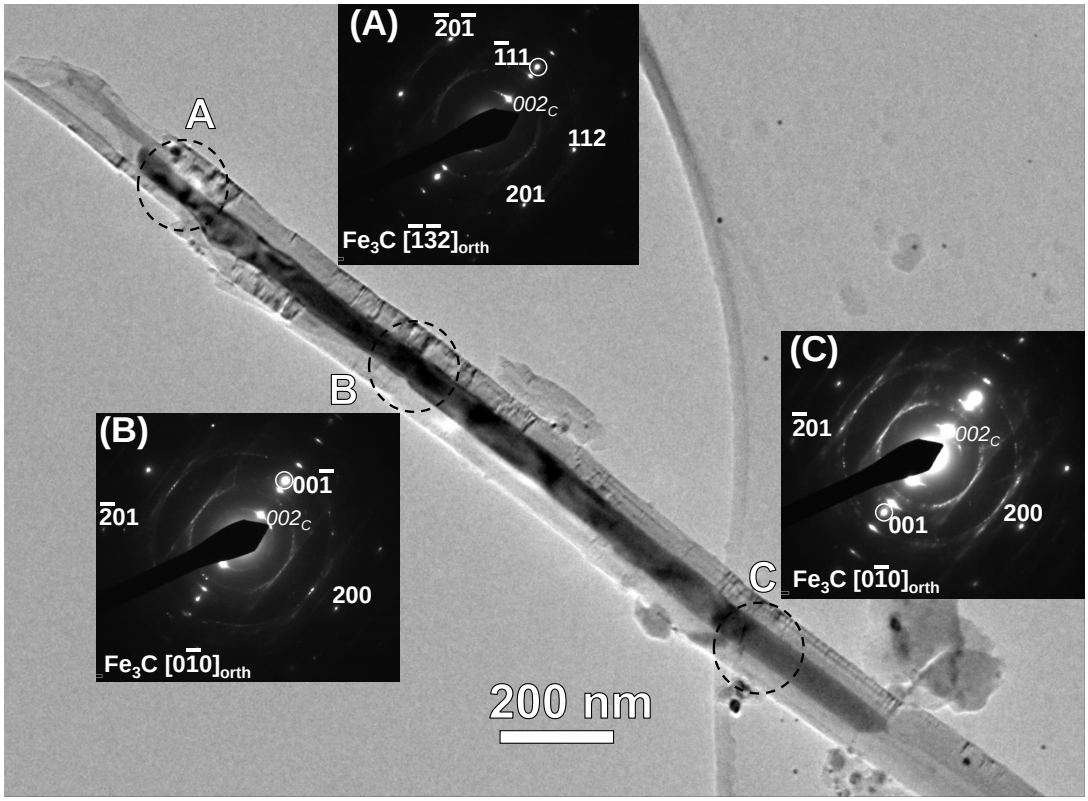

Figure 4.10: Transmission electron micrograph of the continuous Fe_3C nanowire encapsulated by multiwalled carbon nanotube and the insets are the selective area electron diffraction patterns taken from the area within the broken circles of 160 nm area of the nanowires. The identified zone axis are: (A) $Fe_3C\ [\bar{1}\bar{3}2]$, (B) $Fe_3C\ [0\,\bar{1}0]$, and (c) $Fe_3C\ [0\,\bar{1}0]$.

Continuous γ-Fe nanowire

Figure 4.11 is an example of rarely observed encapsulated γ-Fe phase at room temperature, a metastable phase of iron which is stable at high temperature and high pressure as shown in the equilibrium phase diagram shown in Figure 2.12 [12]. The surprising presence of metastable γ-Fe phase inside carbon nanotubes has previously been reported [14–16].The indicated 002_C reflections shown originated from the graphitic layers of the MWCNTs, Figure 4.11.

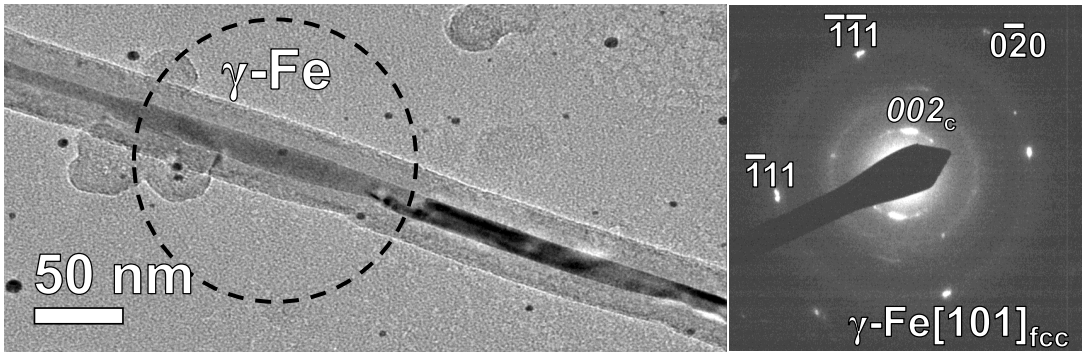

Figure 4.11: Transmission electron micrograph of the γ-Fe nanowire encapsulated by multiwalled carbon nanotube at room temperature and on the right is the selective area electron diffraction pattern taken from the area within the broken circle of 160 nm area of the nanowire. The highlighted zone axis is γ-Fe $[101]_{\text{fcc}}$ with a space group of $(Fm\bar{3}m)$. The indicated 002_{C} reflections originated from the graphitic layers of the MWCNTs.

4.1.2 Synthesis of high γ-Fe-content nanowires

The aim of this work is to find the optimum location for substrates in the reactor for the production of high γ-Fe-content nanowires. It was assumed that the high γ-Fe-content in the encapsulated nanowires would increase the probability of formation of α-Fe/γ-Fe junctions.

Three sequentially arranged roughened quartz substrates were placed at different locations within the reactor at corresponding temperatures of 878 °C, 921 °C and 944 °C (Figure 3.3). Ferrocene flowing vapours over these roughened substrates yielded radial structures with varying γ-Fe-content. The furnace was cooled to room temperature at its natural rate (2 °C/min). The furnace temperature profile of the first 30 cm used for the synthesis is shown in the Figure 4.12. The sequential arrangement of the substrates is indicated under the plot and their corresponding temperatures have also been indicated (Figure 4.12).

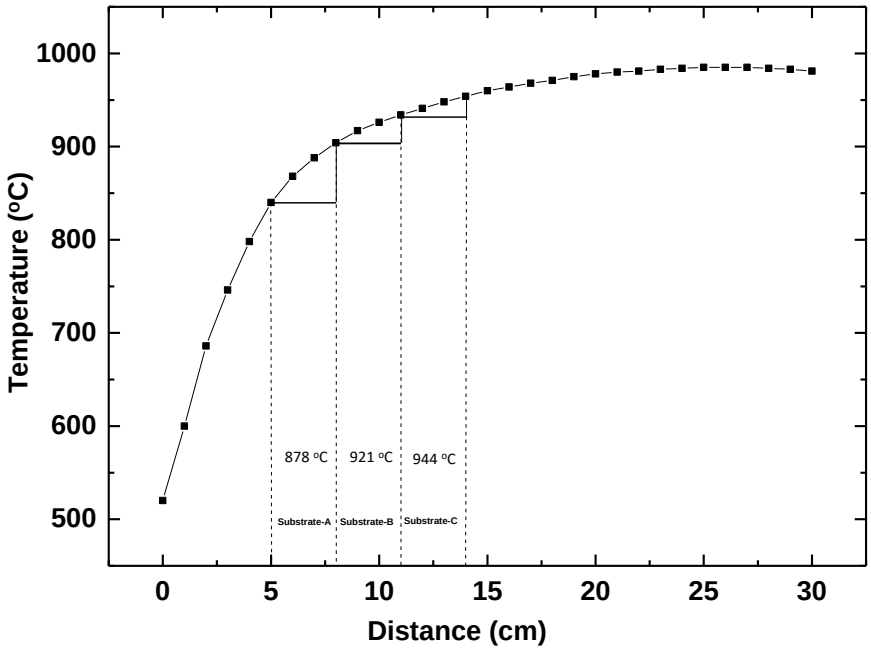

Figure 4.12: Temperature profile of the first 30 cm of the furnace operated at 990 °C used for the synthesis of radial structure using sequentially arrange substrates at three different thermal locations with corresponding temperatures at these locations have been indicated. The 878 °C, 921 °C and 944 °C shows the temperature of the mid points of the three substrates, respectively.

The morphology of the reaction products was found to be consistent with the previous studies performed on radial structures [10, 95]. Relatively high γ-Fe-content has been found in the nanowires produced at thermal location with the corresponding temperature of 944 °C.

The X-ray diffraction data obtained from the powder extracted from the three substrates is presented in Figure 4.13 (A-C).

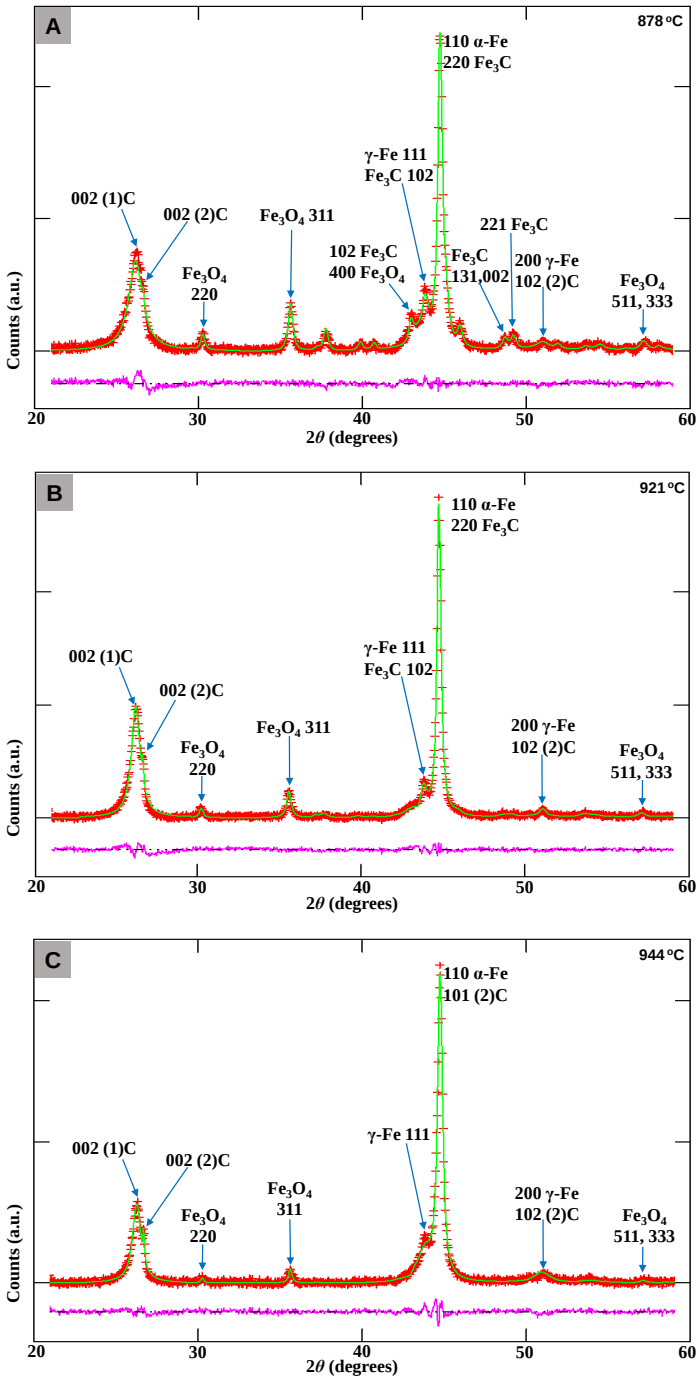

Figure 4.13: Typical X-ray diffractograms data (red), Rietveld refinement (green), and difference (purple) for powder extracted from quartz substrates located at 878 °C, 921 °C and 944 °C of the CVD reactor. Arrows denote the reflections from the crystal planes attributed to each intensity peak. (A) The relative weight abundances of the encapsulated phases are 51% of cubic α-Fe ($Im\bar{3}m$), 11% cubic γ-Fe ($Fm\bar{3}m$) and 38% of orthorhombic Fe_3C ($Pnma$). (B) The relative weight abundances of the encapsulated phases are 71% of α-Fe, 14% of γ-Fe and 15% of Fe_3C.(C) The relative weight abundances of the encapsulated phases are 75% of α-Fe, 25% of γ-Fe and 0% of Fe_3C.

The relative abundances of the encapsulated phases extracted from the Rietveld refinement, α-Fe with space group ($Im\bar{3}m$), γ-Fe space group ($Fm\bar{3}m$) and Fe_3C space group ($Pnma$) are summarised in Table 4.2.

Substrate-temperature	Relative abundance (wt.%)		
	α-Fe	γ-Fe	Fe_3C
878 °C	51	11	38
921 °C	71	14	15
944 °C	75	25	0

Table 4.2: Summary of the relative abundances of the encapsulated phases, extracted from the Rietveld refinement of the X-ray diffractograms in Figure 4.13.

A simple observation that can be made from the analysed X-ray diffraction data is the presence of significantly high γ-Fe-content (25%) near isothermal zone (downstream) of the reactor entrance as compared to the γ-Fe content formed on upstream substrates (Table 4.2). On the other hand, the high Fe_3C-content (38 %) is found only away from the isothermal zone, upstream of the reactor entrance and α-Fe was found to be constant in the nanowires formed on the downstream substrates. The presence of Fe_3C is revealed by the observation of 102, 220, 131, 002 and 221 peaks shown in Figure 4.13 (A). Surprisingly, some of these peaks disappear in Figure 4.13 (B) and the remaining disappear in Figure 4.13 (C). The absence of Fe_3C peaks in Figure 4.13 (C) is surprising since the Fe_3C is considered as an essential intermediate for the growth of the carbon nanotubes [14, 129–136]. However, the absence of metal carbides (Fe_3C and Ni_3C) has also been noticed in synthesis of NiFe encapsulated nanowires synthesised by conventional solid- and liquid-source CVD. But none of the authors commented on the absence of Fe_3C in the final product nor attempt to describe the growth mechanism [137–139]. However, the remarkable decrease in Fe_3C content suggests that the growth process is either initiated without the intermediate iron-carbide nanoparticle formation at elevated temperature, or the graphitic carbon wall formation is driven by the carbon supply from an unstable carbide that subsequently decomposes at high rates at elevated temperatures

[1]. According to Fe-C phase diagram, the most likely iron phase at 944 °C is γ-Fe (Figure 2.12). Therefore, radial structures nucleated at elevated temperatures will have high volume fraction of γ-Fe which is likely to retain high γ-Fe content at room temperatures.

Conclusion:

In conclusion boundary layer chemical vapour synthesis was successfully employed to reproduce radial structures with low and high γ-Fe-content nanowires. The evidence from this study suggests that high γ-Fe content in the nanowires can be achieved at elevated temperatures. The adopted approach could be useful for producing radial structures with high density of α-Fe/γ-Fe junctions

4.2 First observation of α-Fe/γ-Fe junctions in Fe-based nanowires

In this part of the chapter, microstructural analysis of the encapsulated Fe-based nanowires with high γ-Fe-content and the first observation of α-Fe/γ-Fe junctions in these nanowires is reported. This work was carried out in collaboration with Dr. Mert Kurttepeli, Professor Gustaaf Van Tendeloo and Professor Sara Bals from EMAT, University of Antwerpen, Dr. Nadezda V. Tarakina and Dr. Rory M. Wilson, Queen Mary University of London.

Radial structures were synthesised by flowing ferrocene vapour over a roughened quartz substrate located at a position with a temperature of 944 °C in the CVD reactor described in Chapter 3 (see Figure 3.1). The reactor is cooled down to room temperature at its natural rate of cooling (2 °C/min).

The post-synthesis deposits on the rough substrate were examined using scanning electron microscopy (Figure 4.14). These deposits are in the form of a powder comprising ensembles of carbon nanotube radial structures.

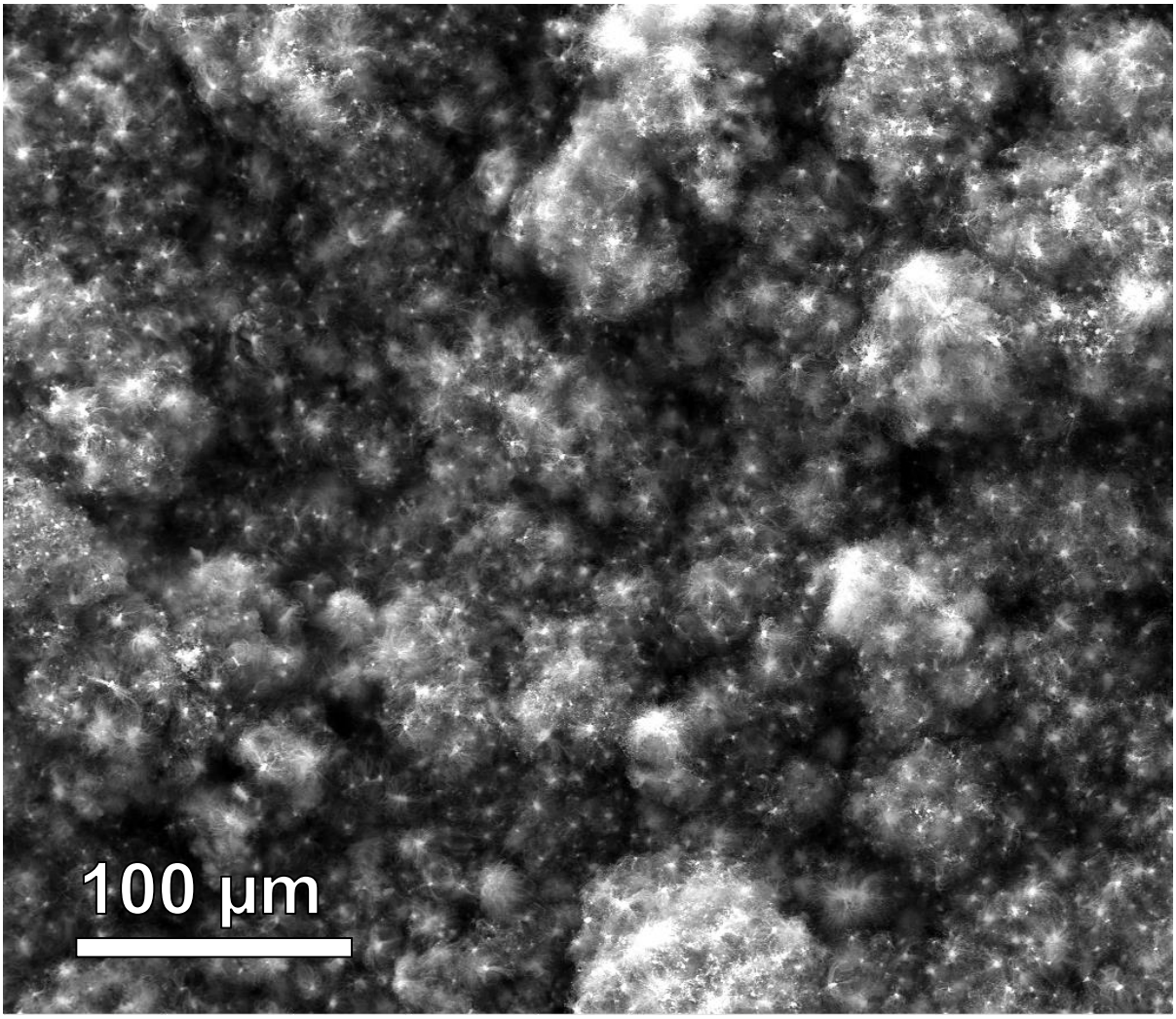

Figure 4.14: Scanning electron micrograph of an ensemble of radial structures deposited on a roughened quartz substrate.

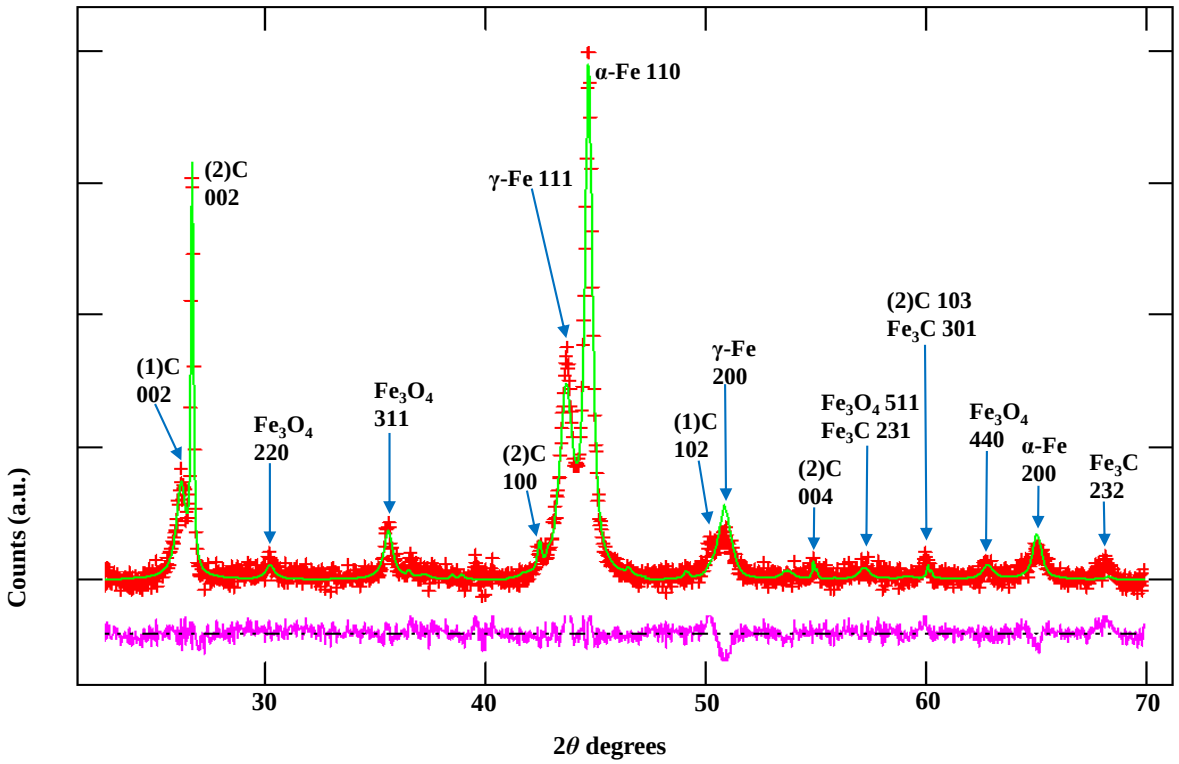

Figure 4.15: Typical X-ray diffractogram data (red), Rietveld refinement (green), and difference (purple) for a powder extracted from the reactor. Arrows denote the crystal planes attributed to each intensity peak. The encapsulated phases were analysed in terms of the following components of α-Fe ($Im\bar{3}m$, Crystal Open Database Ref. 1100108), γ-Fe ($Fm\bar{3}m$, Crystal Open Database Ref. 9008469), and Fe_3C (Pnma, Crystal Open Database Ref. 16593). The relative weight abundances of these phases are 56% of cubic α-Fe, 41% cubic γ-Fe and 3% of orthorhombic Fe_3C. The cubic Fe_3O_4 (space group $Fd\bar{3}m$, ICSD Chemical Database Ref. 84098) content results from spontaneous oxidation of non-encapsulated iron particles when the powder is handled in air, this constitutes less than ten percent of the total sample weight. The lower angle graphitic carbon peak, (1)C, corresponding to the 002 reflection from graphite (space group $P6_3/mmc$, ICSD Chemical Database Ref. 53781), originates from reflections from the graphitic walls of the multiwall carbon nanotubes, inter-wall spacing 0.34 nm. The second graphitic peak, (2)C, corresponds to the lattice spacing 0.33 nm (002 peak of graphite hexagonal $P6_3/mmc$, ICSD Chemical Database Ref. 52230) of the graphitic shell of the spherical particles that comprise the core of the radial structures, [10].

A refinement result of the representative fit of the observed X-ray diffraction data obtained from powder extracted from the reactor, is given in Figure 4.15. The Rietveld refinement provided estimates of relative weight abundances of α-Fe and the retained γ-Fe in the encapsulated nanowire; 56% and 41%, respectively. The absence of significant Fe_3C features in the diffractogram suggests a relative abundance of the order of one to

several percent. The details of the relative weight abundance and quality of fit indicators extracted from the refinement of X-ray diffractogram in Figure. 4.15 are summarized in Table 4.3. The extracted unit cell parameters are given in Table 4.4.

Relative abundance of encapsulated phases (wt.%)			**Profile fit indicators**		
α-Fe ($Im\bar{3}m$)	γ-Fe ($Fm\bar{3}m$)	Fe_3C (*Pmna*)	χ^2	Rp	wRp
56	41	3	2.183	0.0273	0.0351

Table 4.3: Summary of the relative abundance of the encapsulated phases and quality of fit indicators, extracted from the Rietveld refinement of the X-ray diffractogram in Figure 4.15.

Unit cell parameters of various phases					
α-Fe ($Im\bar{3}m$)	γ-Fe ($Fm\bar{3}m$)	Fe_3C (*Pmna*)	(1)C) $P6_3/mmc$	(2)C $P6_3/mmc$	Fe_3O_4 ($Fd\bar{3}m$)
2.868(1) Å,	3.593(1) Å,	4.890(6) Å 7.182(5) Å 4.681(5) Å	2.484(3) Å, 2.484(3) Å, 6.817(4) Å	2.457(1) Å, 2.457(1) Å, 6.689(0) Å	8.376(3) Å,

Table 4.4: The unit cell parameters extracted from the X-ray diffractogram in Figure 4.15.

Since the extracted lattice parameter for γ-Fe, 3.593 Å, is greater than that obtained by extrapolating the carbon concentration dependence of the dilute carbon alloy values to zero solute content (3.556 Å), we conclude the presence of interstitial carbon atoms is the most likely source of stabilisation. Assuming a linear relationship between the lattice parameter and carbon concentration (Equation 2.2), we estimate the carbon content to be 0.8 wt.% [46, 47].

The spatial distribution of the observed phases within the nanowire was investigated by TEM imaging and SAED. Typical examples of most frequently encountered compositions and junctions are outlined below.

1. α-Fe/γ-Fe junctions

An example of a sequential α-Fe/γ-Fe junction is presented in Figure 4.16. The location of the junction was inferred from the abrupt change in contrast indicated by a white

arrow. The $(\bar{1}11)$ crystal plane reflection from γ-Fe crystallite is oriented parallel to the nanotube axis inferred from $002_{\,C}$ reflection from the graphitic nanotube walls (Figure 4.16 (A) and in case of α-Fe crystallite the $(1\,\bar{1}0)$ crystal plane reflection is oriented parallel relative to the nanotube axis (Figure 4.16(B) and (C)).

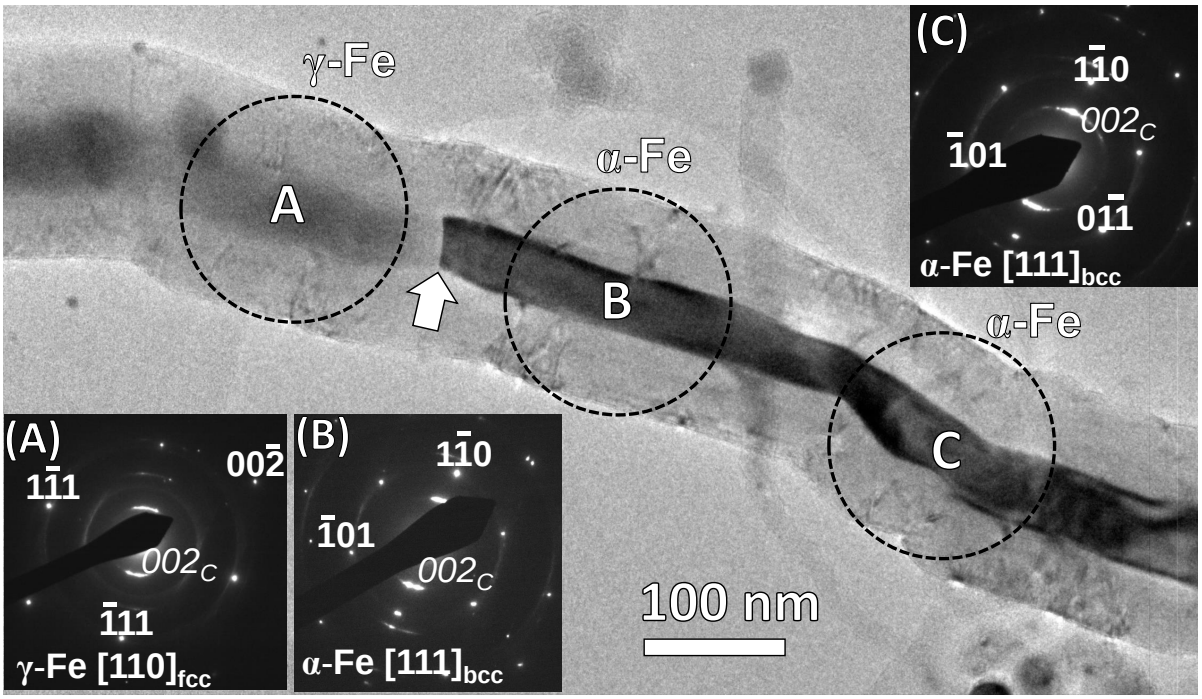

Figure 4.16: Transmission electron micrograph of an encapsulated nanowire; the image-plane electron beam area of diameter 160 nm is indicated by the broken circles centred on the points A-C. The image shows contrast variation along the length of nanowire. The highlighted zone axes are indicated in each figure: (A) γ-Fe $[110]_{\mathrm{fcc}}$, (B) α-Fe $[111]_{\mathrm{bcc}}$ and (C) α-Fe $[111]_{\mathrm{bcc}}$. The white arrow indicates the likely position of the α-Fe/γ-Fe junction between points A and B in the internal cavity of the nanotube. The $002_{\,C}$ reflections of the graphitic nanotube walls correspond to an inter-wall spacing of 0.34 nm which agrees with that value calculated from the Bragg peak labelled 1(C) in Figure 4.15.

Another example of a nanowire comprised sequential α-Fe and γ-Fe crystallites is given in Figure 4.17, the likely location of an α-Fe/γ-Fe junction, deduced from the contrast in the bright-field image and a reduction in the nanowire radius in the α-Fe $\rightarrow$ γ-Fe direction, is indicated by a large white arrow in Figure 4.17 (I)-(III). The nanowire is terminated by a $\sim$100 nm length γ-Fe crystallite with a convex termination, Figure 4.17 (III). Figure 4.17 (B), (C) shows $[100]_{\mathrm{bcc}}$ and $[011]_{\mathrm{bcc}}$ parallel to the nanotube axis; this

observation is consistent with the previously observed <001> directions for α-Fe and <110> directions for γ-Fe parallel to the nanotube axes [15, 140].

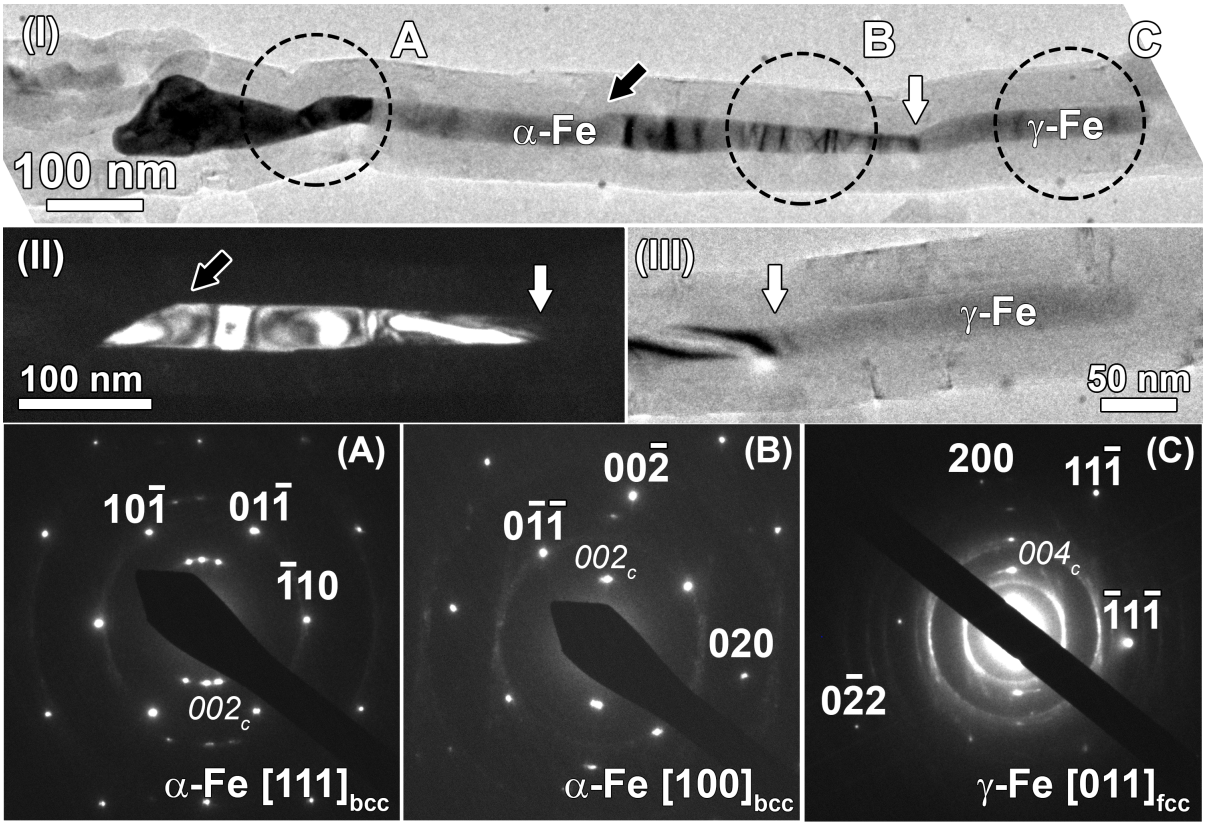

Figure 4.17: (I) Transmission electron micrograph of an encapsulated nanowire; the image-plane electron beam area of diameter 160 nm is indicted by the broken circle centred on the points A-C., the image showing contrast variation along the nanowire, (II) the dark-field image that confirming the polycrystalline nature of the nanowire and is taken around [00 $\bar{2}$] spot appearing in (B), and (III) γ-Fe crystallite with ∼100 nm length having a convex end, and the white arrow indicating the region of constriction in the internal cavity. The highlighted zone axes are indicated in each figure: (A) α-Fe [111]$_{bcc}$, (B) α-Fe [100]$_{bcc}$, (C) γ-Fe [011]$_{fcc}$. The white arrows indicate the likely position of the α-Fe/γ-Fe junction between points B and C. The black arrows indicate the grain boundary between the same phase; α-Fe [111]$_{bcc}$ and α-Fe [100]$_{bcc}$. The 002 $_C$ and 004 $_C$ reflections of the graphitic nanotube walls correspond to an inter-wall spacing of 0.34 nm which agrees with that value calculated from the Bragg peak labelled 1(C) in Figure 4.15. The multiple spots labelled 002 $_C$ in (A) are likely to be a consequence of the irregular outer diameter of the nanotube at this position.

A close inspection of another sequential α-Fe/γ-Fe junction, Figure 4.18, similarly reveals a reduction of the radius of the internal cavity in the region of the junction; analysis of the fast Fourier transformations obtained across the junction shows that in both α-Fe

and γ-Fe grains have the [001] direction parallel to the tube axis.

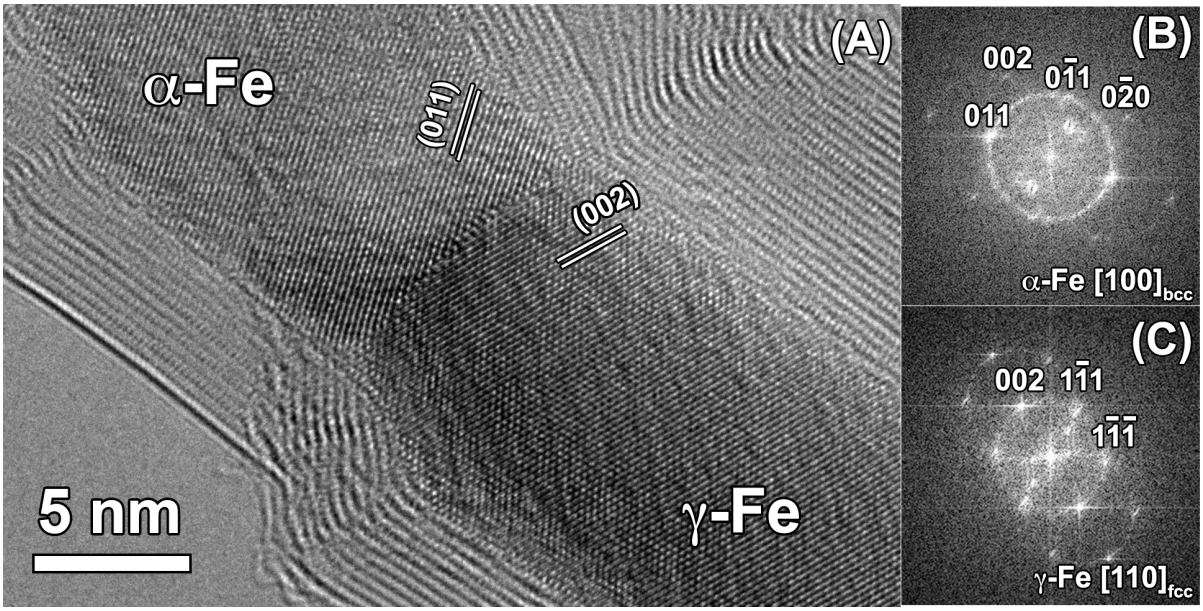

Figure 4.18: (a) High-resolution TEM image of the α-Fe/γ-Fe junction, and corresponding Fast Fourier transformations obtained from left (b) and right (c) sides of the junction.

Many of the features of the γ-Fe crystallite and the encapsulating nanotube in Figure 4.19 (i) resemble those induced by irradiation with a high electron beam intensity (400 A cm^{-2}) in TEM studies of nanotube-encapsulated Fe_3C nanowires at 600 °C [141]. The micrographs in this study were obtained at room temperature with electron beam intensities of $\sim$ 60-120 pA cm^{-2} so the common features, namely, the convex crystallite termination and the abrupt variation of the nanowire diameter, are unlikely to be irradiation induced. Nevertheless, the cause of the convex termination, namely, the closing of the inner nanotube walls due to the migration of carbon interstitial defects, is likely to be the same although produced during the growth process rather than by TEM [142]. Electron beam radiation induces an abrupt change in nanowire diameter by (i) causing nanowire to extrude along the nanotube axis owing to a reduction in the nanotube diameter due to dynamic expulsion of carbon atoms from the walls by the electron beam, (ii) subsequent accumulation of graphitic carbon in the internal cavity at the end of the extruding nanowire, and (iii) its conversion to nanotube walls departing from the end of

the nanowire; the net result is an abrupt reduction in the diameter of the nanowire [17].

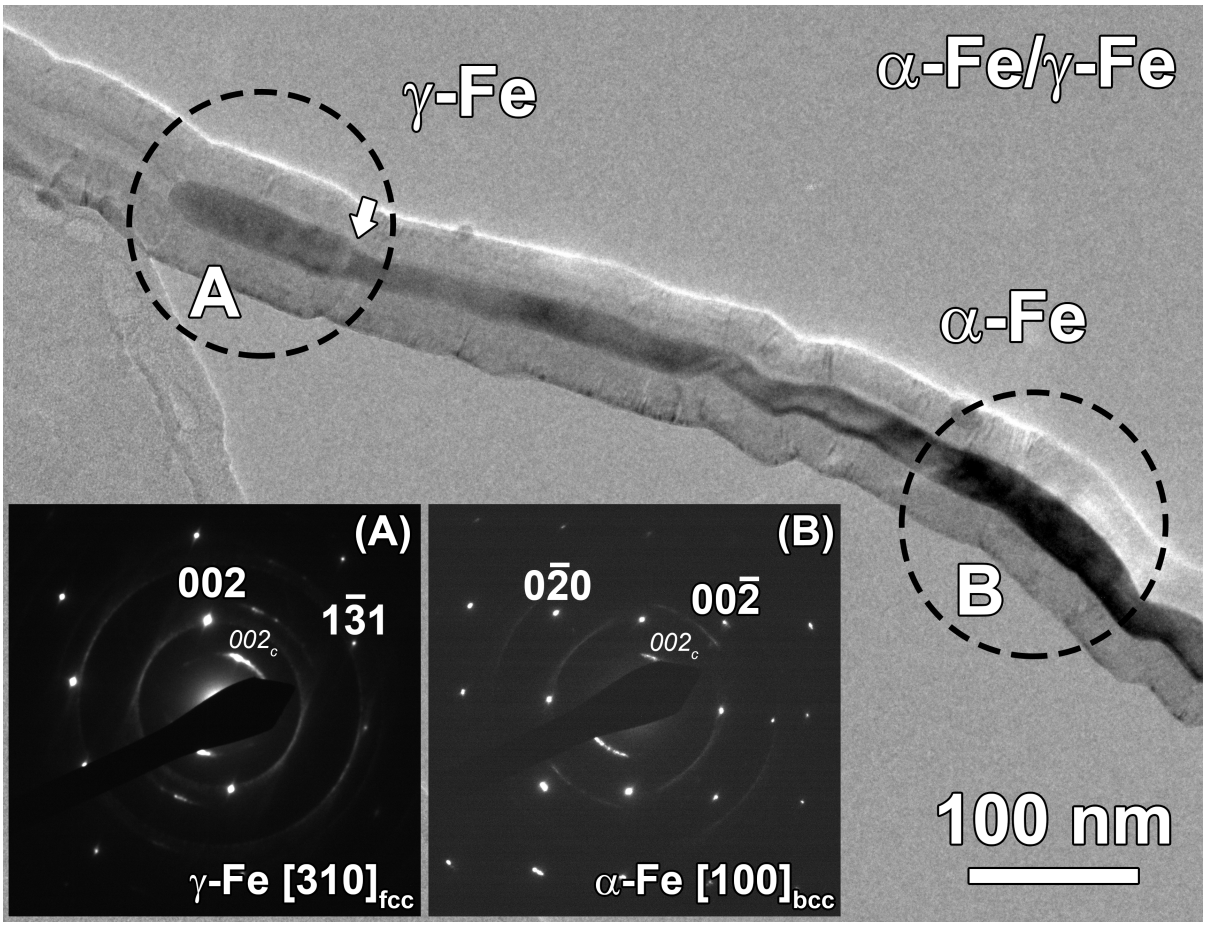

Figure 4.19: Transmission electron micrograph showing an encapsulated nanowire containing a α-Fe/γ-Fe junction in a region of a constriction in the internal cavity of the nanotube indicated by the black arrow. The cavity diameter at the constriction is 18 nm and the diameter of the γ-Fe crystallite far from the junction is 28 nm; the image-plane electron beam area of diameter 160 nm is indicated by the broken circle centred on the points A and B. The highlighted zone axes are indicated in each figure: (A) γ-Fe $[310]_{\mathrm{fcc}}$ and (B) α-Fe $[100]_{\mathrm{bcc}}$.

The exact location of the α-Fe/γ-Fe junction cannot confidently be determined from this analysis but if it is to be found exactly at the point of narrowing of the nanowire diameter then an explanation for the α-Fe $\rightarrow$ γ-Fe transformation at this point could be the change in the rate of growth of this nanowire being favourable to capture of the γ-Fe phase.

2. α-Fe/Fe_3C junctions

A typical micrograph of an α-Fe/Fe_3C junction-containing encapsulated nanowire is

shown in Figure 4.20, upper left. The SAED patterns obtained from 160 nm diameter areas centred on the three points A-C, are given the corresponding label in Figure 4.20.

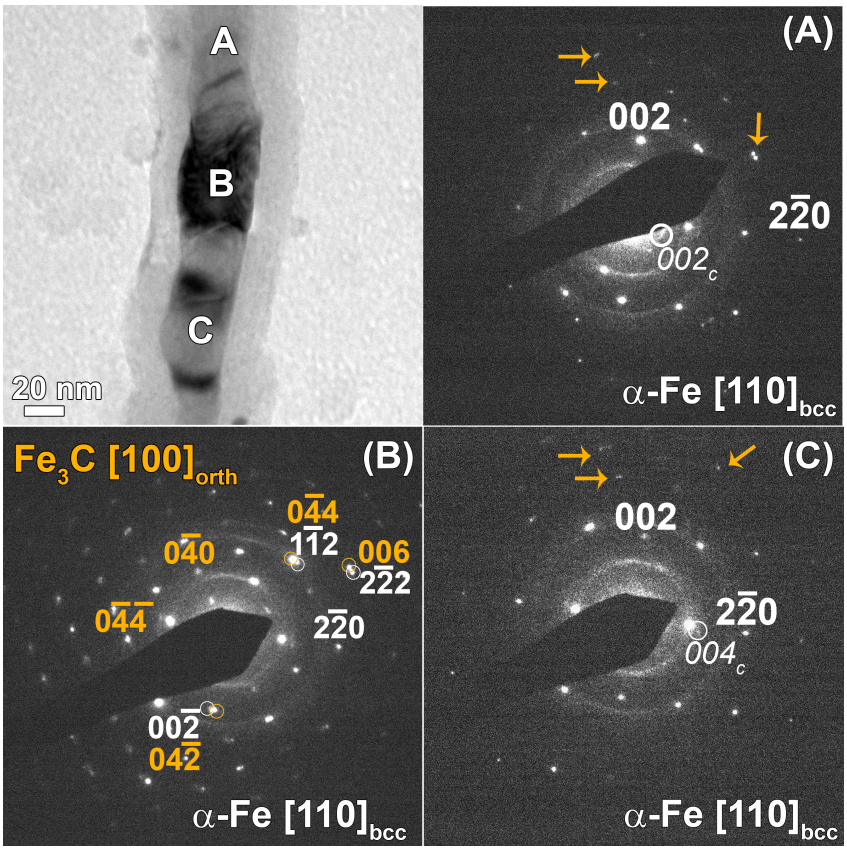

Figure 4.20: Upper left, transmission electron micrograph of an encapsulated nanowire; the SAED patterns obtained from the three areas centred on points A-C are given corresponding labels on the following images. The highlighted zone axes are indicated in each Figure: (A) α-Fe $[110]_{bcc}$, (B) Fe_3C $[100]_{orth}$ and α-Fe $[110]_{bcc}$, and (C) α-Fe $[110]_{bcc}$ obtained after tilting by 2°. The white and orange text in (B) connect highlighted spots associated with the Fe_3C $[100]_{orth}$ and α-Fe $[110]_{bcc}$ orientations, respectively. Orange arrows in the upper part of both (A) and (C) α-Fe $[110]_{bcc}$ is pointing to the Fe_3C reflections similar to (B) Fe_3C $[100]_{orth}$.

The crystal planes corresponding to the diffraction spots in Figure 4.20 (A) and Figure 4.20 (C) are those of α-Fe but with slightly differing crystallographic orientations relative to the nanotube axis. Morelos-Gómez *et al.* attribute the splitting or doubling of the diffraction spots as observed in Figure 4.20 (B) to the presence of coaxial volumes of α-Fe and Fe_3C; but this effect could also be explained by contact between sequential

crystallites over an area that is a significant fraction of that of the probing electron beam [17]. Nevertheless, the coincident highlighted zones at point B exhibit the Bagaryatski orientation relationship, $[110]_{bcc} \parallel [100]_{orth}$ for the two crystallites comprising the α-Fe/Fe_3C junction [143].

Magnetisation measurements were performed on powder samples with differing γ-Fe content (41 wt.%, 35 wt.% and 23 wt.%) of the encapsulated nanowires. The relative weight abundances of the encapsulated phases were found using Rietveld analysis of the X-ray diffractograms, Figure 4.15, 4.21 and 4.22.

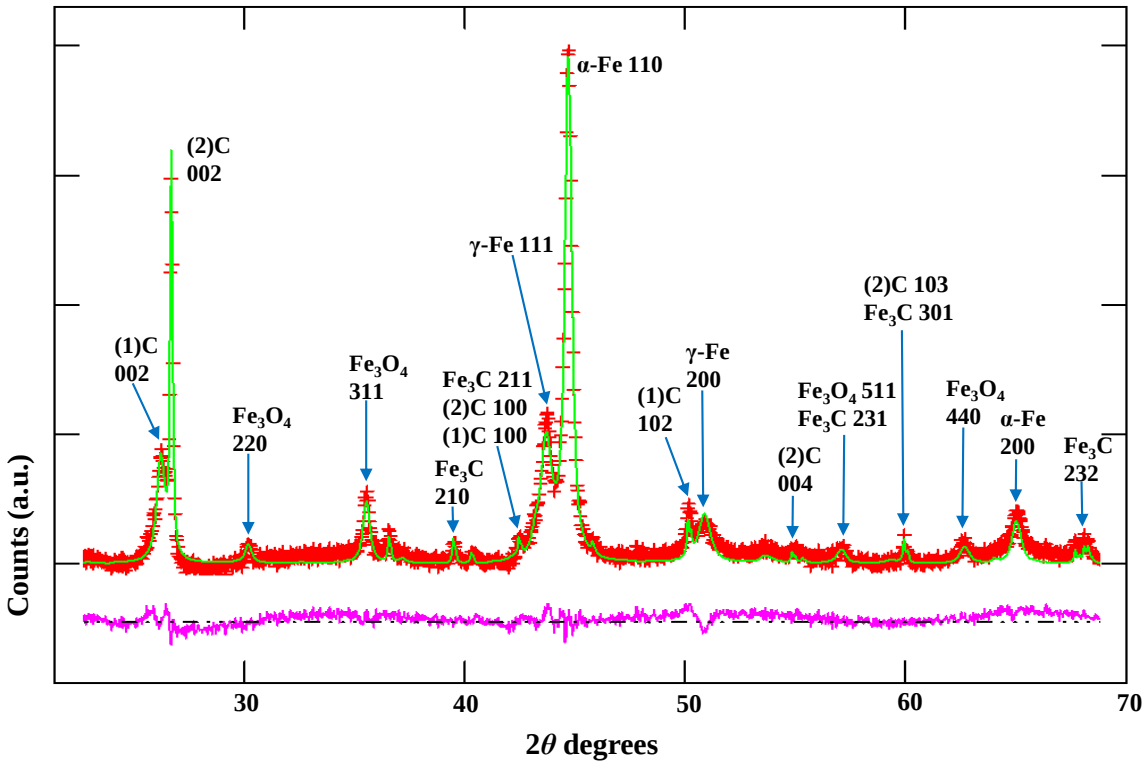

Figure 4.21: X-ray diffractogram data (red), Rietveld refinement (green), and difference (purple) for a powder extracted from the reactor. Arrows denote the crystal planes attributed to each intensity peak. The extracted relative weight abundances of the encapsulated phases are 62% of cubic α-Fe, 35% cubic γ-Fe and 3 % of orthorhombic Fe_3C.

Relative abundance of encapsulated phases (wt.%)			Profile fit indicators		
α-Fe ($Im\bar{3}m$)	γ-Fe ($Fm\bar{3}m$)	Fe_3C ($Pmna$)	χ^2	Rp	wRp
62	35	3	4.472	0.0354	0.0438

Table 4.5: Summary of the relative abundance of the encapsulated phases and quality of fit indicators, extracted from the Rietveld refinement of the X-ray diffractogram in Figure 4.21.

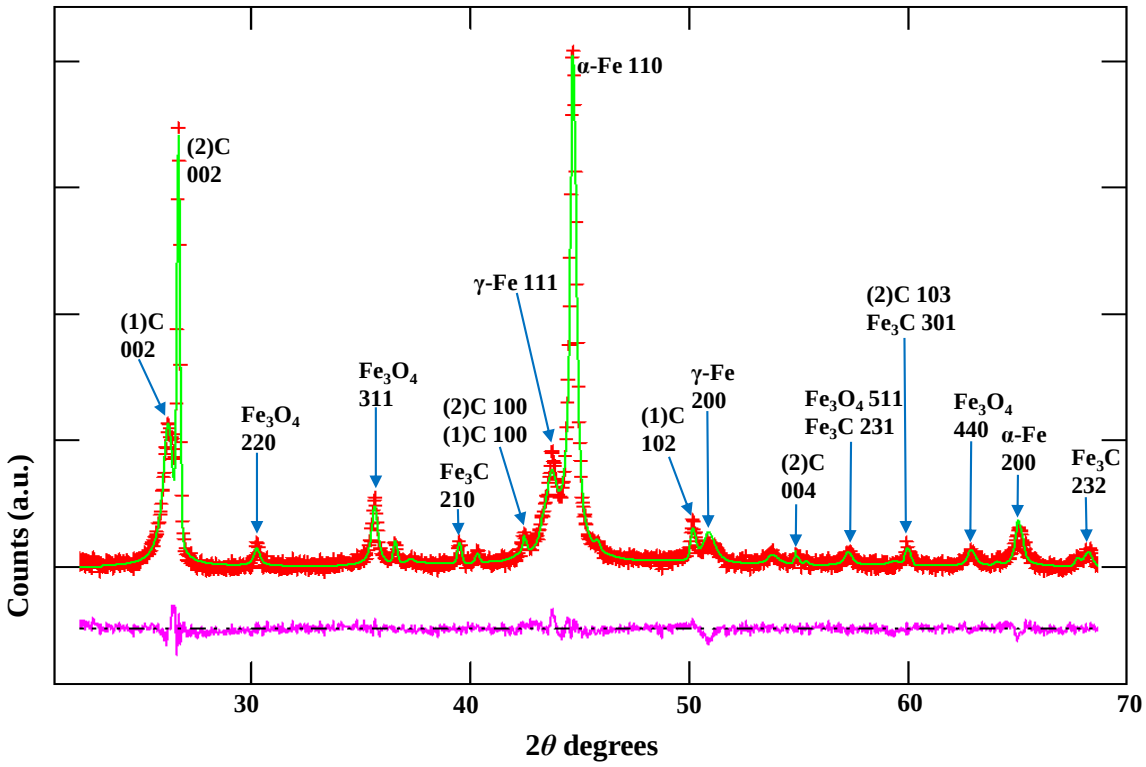

Figure 4.22: X-ray diffractogram data (red), Rietveld refinement (green), and difference (purple) for a powder extracted from the reactor. Arrows denote the crystal planes attributed to each intensity peak. The extracted relative weight abundances of the encapsulated phases are 53% of cubic α-Fe, 23% cubic γ-Fe and 24% of orthorhombic Fe_3C.

Relative abundance of encapsulated phases (wt.%)			Profile fit indicators		
α-Fe ($Im\bar{3}m$)	γ-Fe ($Fm\bar{3}m$)	Fe_3C ($Pnma$)	χ^2	Rp	wRp
53	23	24	2.734	0.0274	0.0359

Table 4.6: Summary of the relative abundance of the encapsulated phases and quality of fit indicators, extracted from the Rietveld refinement of the X-ray diffractogram in Figure 4.22.

The magnetic state of the γ-Fe was inferred from the magnetisation observed in a powder

material with high γ-Fe content (41%) at low temperature, Figure. 4.23.

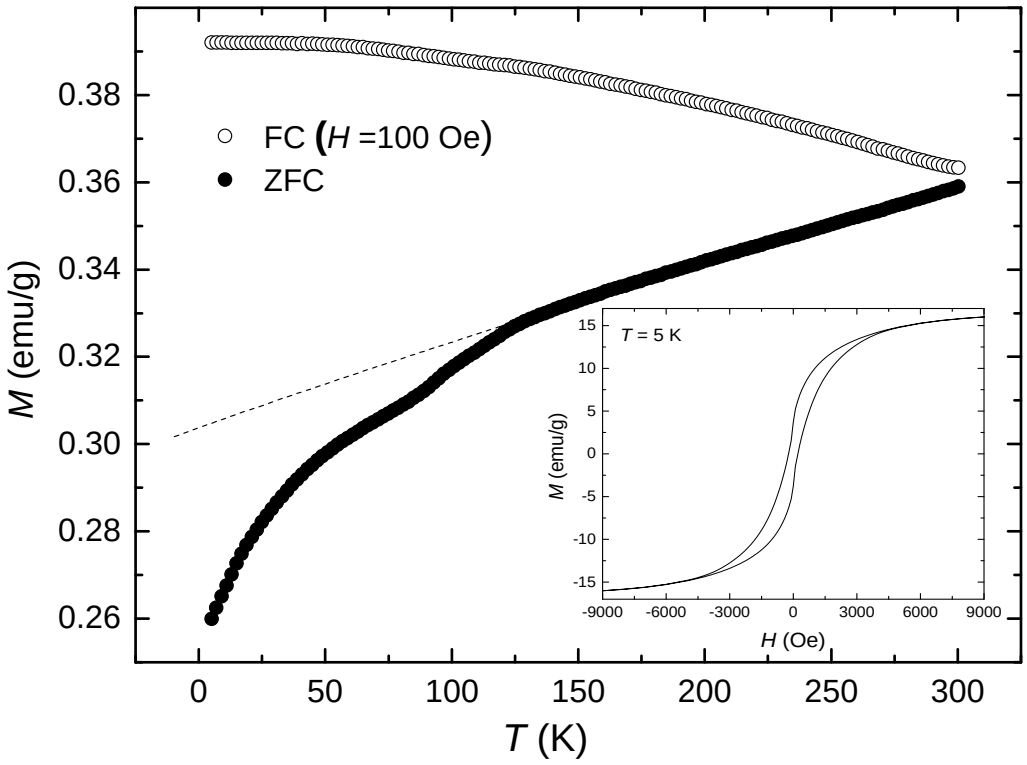

Figure 4.23: The FC and ZFC temperature variations of magnetisation, M, and its variation with magnetic field strength, H, at 5 K (inset). The broken line is a guide to the eye. The extracted relative weight abundances of the encapsulated phases are 56% of cubic α-Fe, 41% cubic γ-Fe and 3% of orthorhombic Fe_3C (Figure 4.15).

The value of saturation magnetisation calculated from the weighted sum of contributions from the nanowire using the saturation magnetisation values for α-Fe (220 emu/g) [144], Fe_3C (169 emu/g), [145] neglecting the contribution from Fe_3O_4 (100 emu/g) and the weakly diamagnetic carbon nanotube walls, is 128 emu/g. The experimental value is 17 emu/g, Figure. 4.23 (inset). This lowering of saturation magnetisation relative to that expected from such calculations, is a common observation in magnetic nanowire systems. It is usually attributed to the pinning of magnetic moments at the surface of a nanowire; this effect greatly increases as the dimensions of the nanowire decrease because

the contribution from the surface moments increases in significance. A transition to the antiferromagnetic state in one of the component crystallites in an otherwise ferromagnetic nanowire is an alternative explanation. There is evidence for the latter interpretation in the temperature variation of the zero-field cooled (ZFC) and field cooled (FC) behaviour of powder extracted from the reactor, Figure. 4.23. The discontinuity in the ZFC trend, here seen at 125 K, has previously been attributed to a transition from the paramagnetic to the antiferromagnetic state in γ-Fe [33].

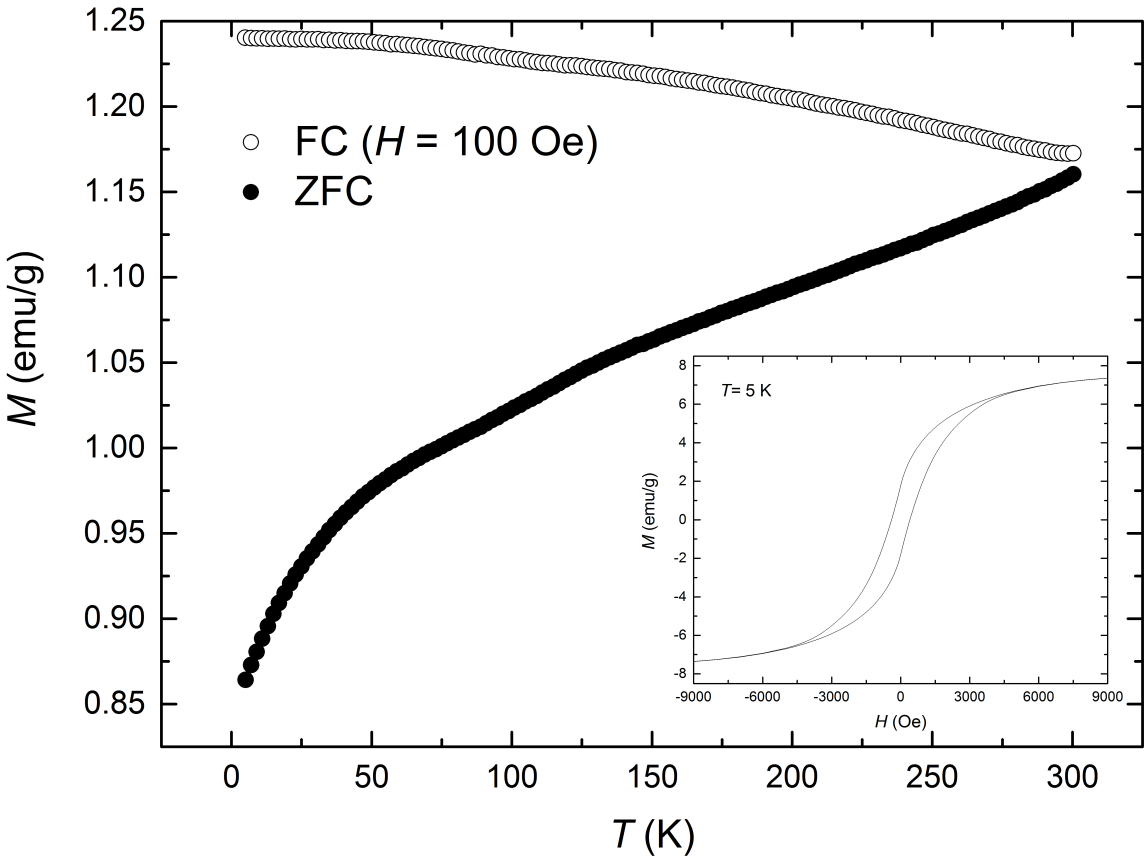

Figure 4.24: The FC and ZFC temperature variations of magnetisation, M, and its variation with magnetic field strength, H, at 5 K (inset). The extracted relative weight abundances of the encapsulated phases are 62% of cubic α-Fe, 35% cubic γ-Fe and 3% of orthorhombic Fe_3C (Figure 4.21).

Figure 4.24 and 4.25 show the magnetization measurements performed on relatively low γ-Fe content (35% and 23%) radial structures powder. The discontinuity in the ZFC trend appearing in Figure 4.23 gradually disappears in Figure 4.24 and 4.25. This indicates

that the observable paramagnetic to the antiferromagnetic transition in ZFC is dependent on the γ-Fe content of the nanowires present in the sample.

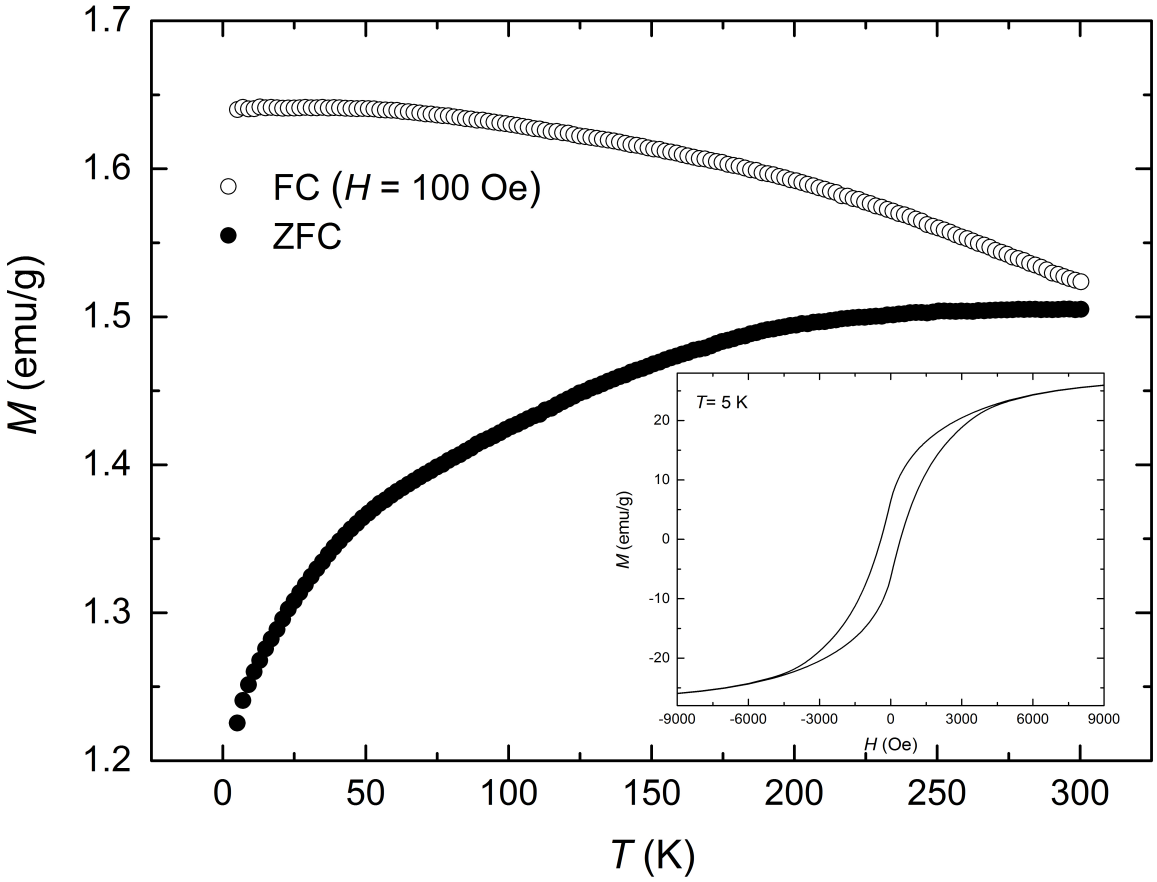

Figure 4.25: The FC and ZFC temperature variations of magnetisation, M, and its variation with magnetic field strength, H, at 5 K (inset). The extracted relative weight abundances of the encapsulated phases are 53% of cubic α-Fe, 23% cubic γ-Fe and 24% of orthorhombic Fe_3C (Figure 4.22).

In case of relatively low γ-Fe content (35% and 23%) magnetisation measurements (Figure 4.24 (inset) and 4.25 (inset)), the saturation magnetisation values calculated from the weighted sum of contributions from the nanowire using the saturation magnetisation values for α-Fe (220 emu/g) [144], Fe_3C (169 emu/g), [145] neglecting the contribution from Fe_3O_4 (100 emu/g) and the weakly diamagnetic carbon nanotube walls, are 141 emu/g and 157 emu/g. The corresponding experimental values are 8 emu/g and 28 emu/g respectively. This observation of lowering of saturation magnetisation values relative to

that expected from such calculations, is found to be similar to that of high γ-Fe content nanowire sample.

Statistical analysis α-Fe/γ-Fe junctions

This work was aiming to find and study the microstructure of α-Fe/γ-Fe junctions. Therefore, while studying Fe-based nanowires under TEM, we focused on the features such as abrupt variation in the diameter or change of contrast in a dark-field imaging aiming to the direct observation of junctions rather than single phase nanowires. However, we encountered frequent observation of individual α-Fe, while γ-Fe was rarely found as an individual encapsulated nanowire. Nevertheless, we present the evidence of γ-Fe observation as in the from of sequential α-Fe/γ-Fe junctions. In addition, Fe_3C content was minimized by performing synthesis at elevated temperatures followed by cooling the reactor at its natural rate to allow the carbon to migrate towards the nanotube walls.

The quantitative phase analysis performed using X-ray powder diffraction is based on sample averaging technique. Therefore, the extracted relative abundances using this technique provides a quick but global estimate of the single crystal phases present in a particular powder sample (example Figure 4.15, Table 4.7). On the other hand, TEM is a size-specific local probing technique to examine a thin specimen of the sample. Therefore, the analysed volume is always very small. However, the obtained relative abundances of these single crystal phases measured from the TEM micrographs (examples in Figure 4.16, 4.19 and 4.17) are compared with the relative abundances extracted from X-ray diffraction. The overall measurement results of the relative abundances obtained from X-ray diffraction and TEM are summarised in Table 4.7.

Techniques	Percentage of relative abundances		
	α-Fe	γ-Fe	Fe_3C
X-ray diffraction	56	41	3
TEM	74	25	1

Table 4.7: Summary of the relative abundances of the encapsulated phases extracted from the Rietveld refinement of the X-ray diffractogram in Figure 4.15 and the TEM micrographs (examples in Figure 4.16, 4.19 and 4.17) .

The obtained percent relative abundance of the α-Fe, γ-Fe and Fe_3C from the Rietveld analysis of X-ray diffractogram given in Figure 4.15 is 56%, 41% and 3% respectively. Whereas, the relative percentage of these phases obtained from the length-scales of the single-crystal nanowires from the TEM micrographs are 74%, 25% and 1% respectively. The differing relative abundances of the corresponding phases in Table 4.7 is likely the consequence of limited sampling under TEM that cannot represent specimen with enough single-crystal phases to be averaged. Therefore, it does not survey enough to represent statistically the sample as the X-ray powder diffraction does. However, the estimates of relative abundances of the encapsulated phases extracted from TEM micrographs confirms the presence of the encapsulated phase identified quantitatively by X-ray diffraction. The consistency of these results depends on the extensive sampling of the specimen under TEM, which requires further investigation.

Figure 4.26 and Figure 4.27 shows the statistical distributions of the diameters of α-Fe and γ-Fe nanowires, respectively. The average diameter of the α-Fe nanowire obtained from the TEM micrographs (examples in Figure 4.9, 4.8, 4.7, 4.16, 4.19 and 4.17) is 27(5) nm.

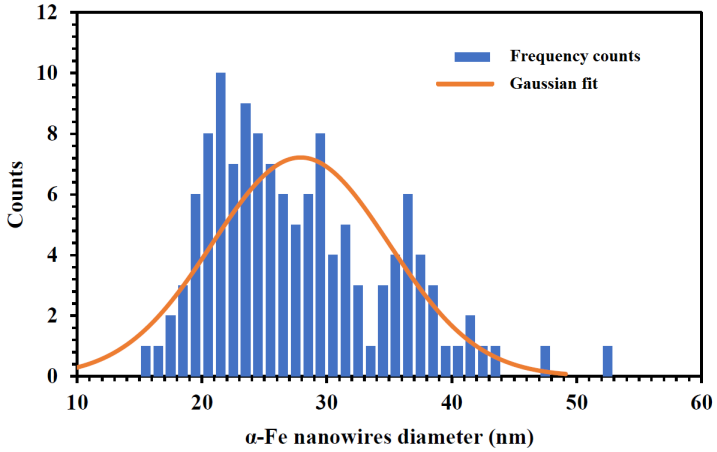

Figure 4.26: (a) Histogram showing the diameter distribution of the α-Fe nanowires obtained from the TEM micrographs. The average diameter is 27(5) nm.

The diameter distribution of γ-Fe obtained from the TEM micrographs (examples in Figure 4.16, 4.19 and 4.17) is provided in Figure 4.27. The average γ-Fe nanowire diameter is 33(7) nm.

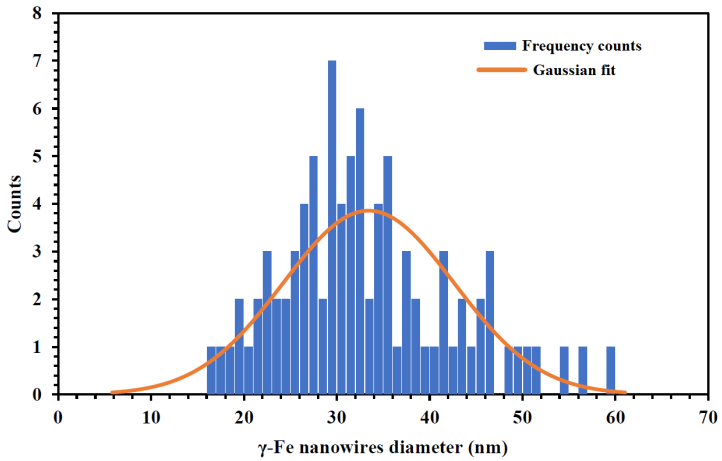

Figure 4.27: Histogram showing the diameter distributions of the γ-Fe nanowires obtained from the TEM micrographs. The average diameter of the γ-Fe nanowire is 33(7) nm.

Conclusion:

The γ-Fe crystallites in iron-based nanowires encapsulated by multiwalled carbon nanotubes are stabilised by dilute carbon alloying. The α-Fe/γ-Fe junctions in the nanowire are arranged sequentially. The α-Fe/Fe_3C junction, a coaxial arrangement exhibit the

Bagaryatski orientation relationship: $[110]_{\mathrm{bcc}} \parallel [100]_{\mathrm{orth}}$. The indirect evidence suggests that the encapsulated γ-Fe is in the antiferromagnetic state at low temperature. From the microscopic analysis of the relative abundances of the encapsulated phases under TEM confirms the presence of encapsulated phases identified from X-ray diffraction.

4.3 The role of substrate roughness in the boundary layer synthesis of radial structures

This work was carried out in collaboration with Dr. Nadezda V. Tarakina and Dr. Rory M. Wilson, Queen Mary University of London.

Here, the influence of substrate roughness on the morphology and composition of the reaction products is tested with a comparative study using high- and low-roughness substrates.

The pre-synthesis scanning electron micrographs of the high- and low-roughness substrates are shown in Figure 4.28 (A) and (B) respectively. Scanning electron micrographs of the post-synthesis deposits on the high- and low-roughness substrates are shown in Figure 4.29 (A) and (B) respectively. By simple inspection it can be seen that although the diameter of a typical radial structure is approximately 12 μm in both cases, the structures found on the low-roughness substrate have fewer radial carbon nanotubes than those on the high-roughness substrate.

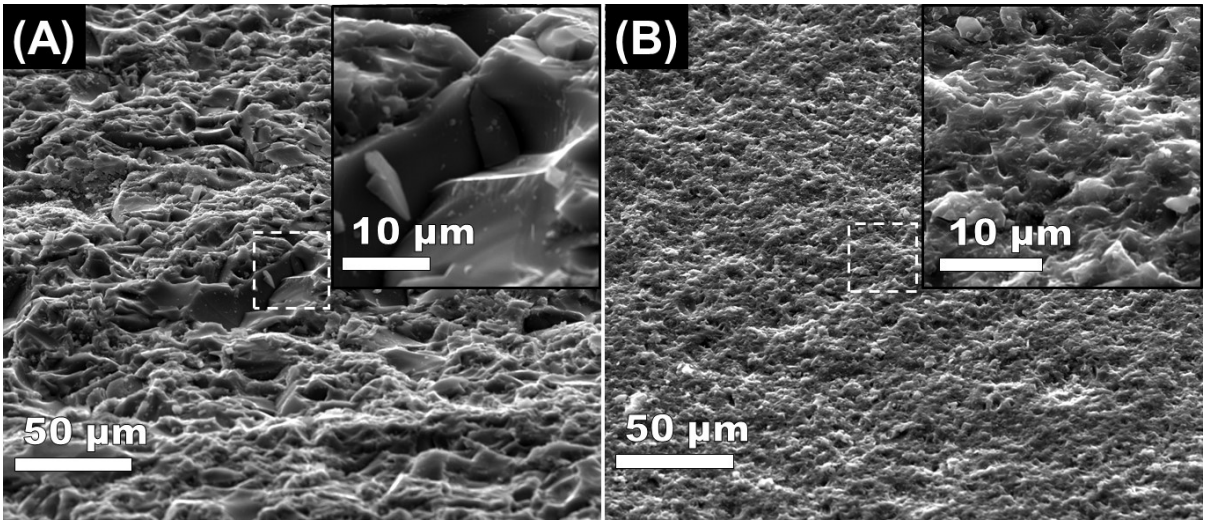

Figure 4.28: Scanning electron micrographs of the (A) high- and (B) low-roughness surfaces. The insets show a higher magnification image of the region within the broken square.

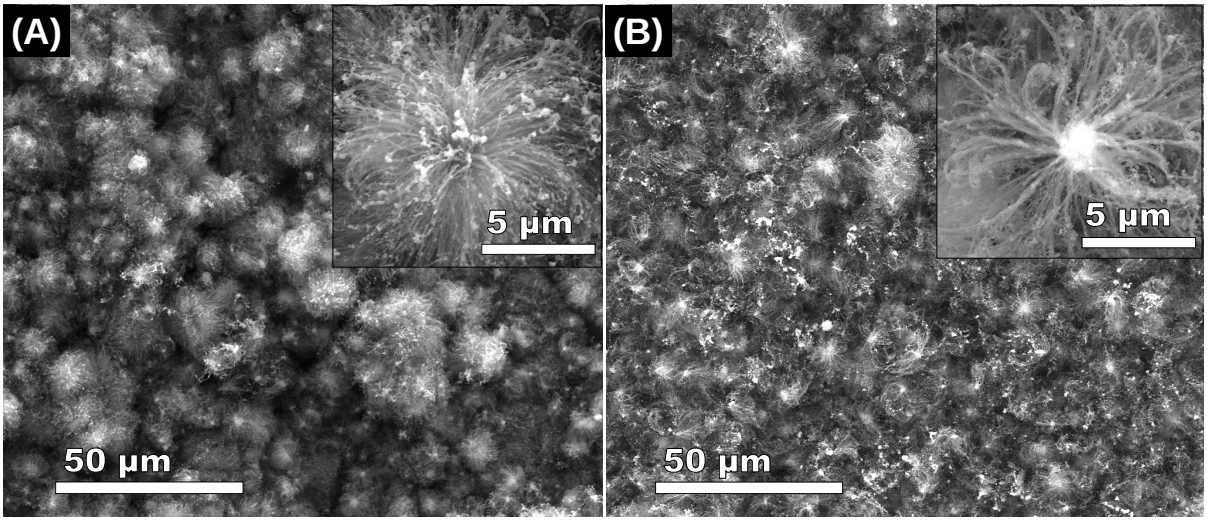

Figure 4.29: (A) Scanning electron micrograph of an ensemble of radial structures deposited on the high-roughness substrate during synthesis. Inset is a typical example of individual radial structure found on the high-roughness substrate. (B) Scanning electron micrograph of an ensemble of radial structures deposited on the low-roughness substrate during synthesis. Inset is a typical example of individual radial structure found on the low-roughness substrate.

The X-ray diffractograms obtained from powder extracted from the two substrates are presented in Figure 4.30 (A) and (B). Reflections from the encapsulated phases were analysed in terms of the following components: α-Fe ($Im\bar{3}m$, Crystal Open Database Ref. 1100108), γ-Fe ($Fm\bar{3}m$, Crystal Open Database Ref. 9008469), and Fe_3C ($Pnma$, Crys-

tal Open Database Ref. 16593). The cubic Fe_3O_4 (space group $Fd\bar{3}m$, ICSD Chemical Database Ref. 84098) content, which constitutes less than ten percent of the total sample weight, is on the exterior of the nanotube, Figure 4.31. The lower angle graphitic carbon peak, (1)C, corresponding to the 002 reflection from graphite (space group $P6_3/mmc$, ICSD Chemical Database Ref. 53781), originates from reflections from the graphitic walls of the multiwall carbon nanotubes, inter-wall spacing 0.34 nm. The higher angles graphitic peaks, (2)C, corresponds to the lattice spacing 0.20 nm and 0.18 nm (101 and 102 peaks of graphite hexagonal $P6_3/mmc$, ICSD Chemical Database Ref. 52230) of the graphitic shell of the spherical particles that comprise the central core, Figure 4.30 (A) [10].

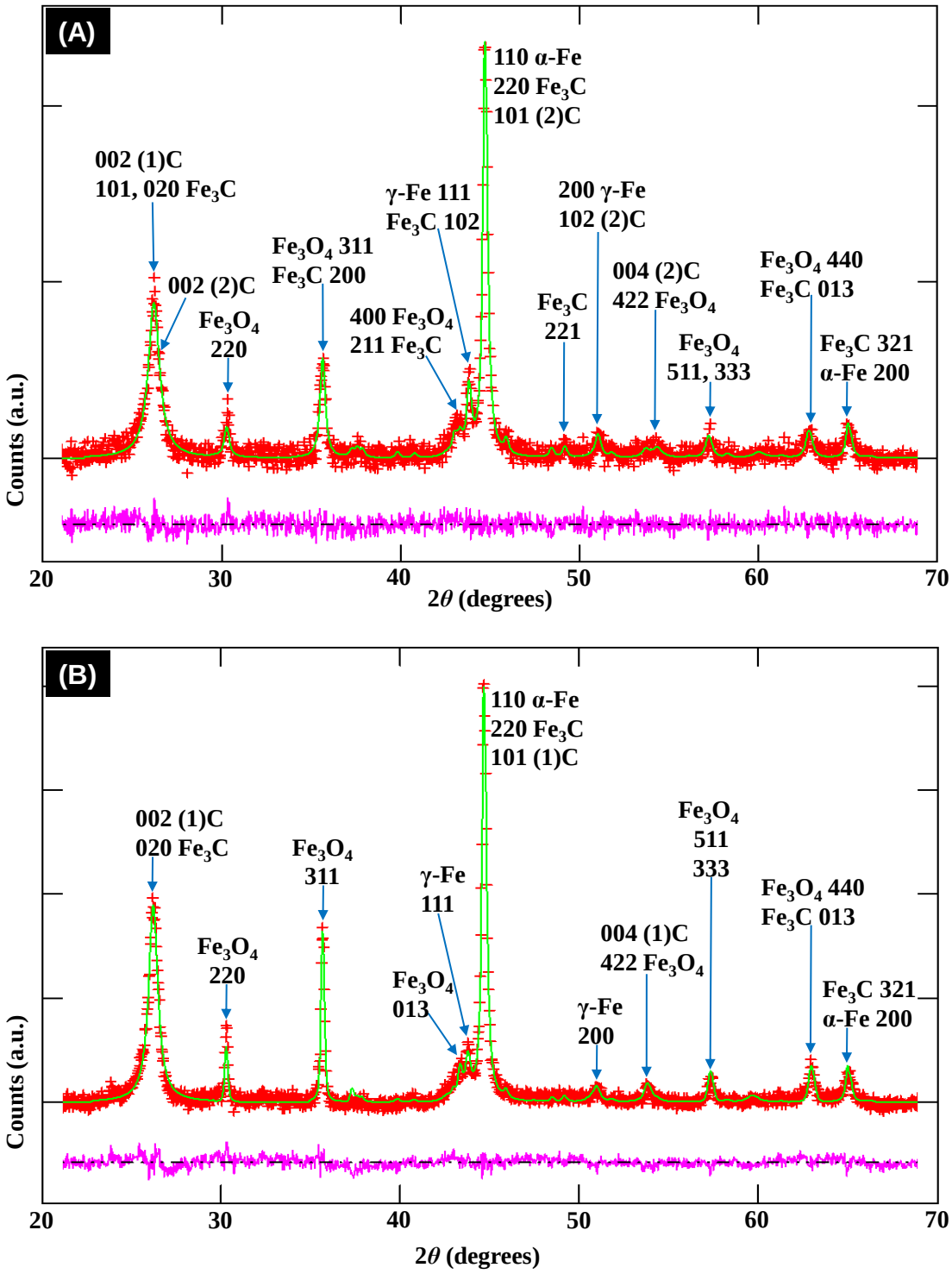

Figure 4.30: X-ray diffractograms data (red), Rietveld refinement (green), and difference (purple) obtained from powder extracted from the high-roughness and low-roughness quartz substrates. Blue arrows denote the crystal planes attributed to each intensity peak. (A) The relative weight abundances of the encapsulated phases are 60% α-Fe, 11% γ-Fe and 29% Fe_3C. (B) The relative weight abundances of the encapsulated phases are 74% α-Fe, 11% γ-Fe and 15% Fe_3C.

TEM study of the reaction products revealed the presence of micromere-length nanowires encapsulated by multiwalled carbon nanotubes, Figure 4.31 (A), and particles of about 7 nm in diameter, Figure 4.31 (B). The fast Fourier transform (FFT) obtained for these particles revealed one set of reflections, which makes unambiguous identification of the phase not possible, Figure 4.31 (B-D). However, most likely these particles are Fe_3O_4 because the only lattice spacing measured from FFT corresponds to the (113) plane of Fe_3O_4. We assume that the formation of Fe_3O_4 results from the post-synthesis oxidation of non-encapsulated iron particles when the powder is handled in air [10].

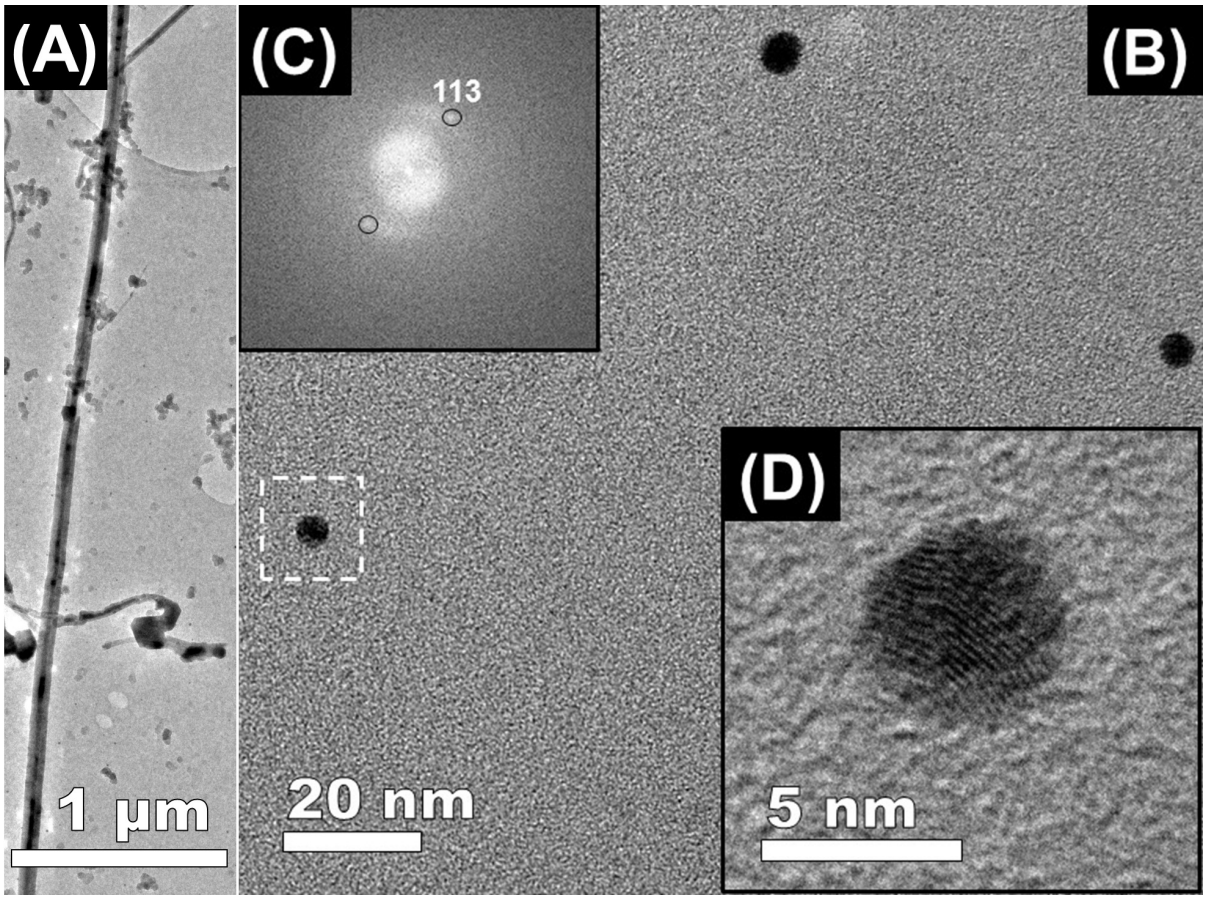

Figure 4.31: (A) A typical example of an individual multiwalled carbon nanotube, the encapsulated nanowire contrasts with the exterior graphitic carbon. (B) A higher resolution image of the nanotube surface showing dark spherical particles of average diameter 6.71(1) nm. (C) The Fourier transform of the high-resolution TEM image (D) of the individual dark particle within the broken square in image (B). The black circles in (C) indicate a lattice spacing of 0.253 nm which corresponding to the (113) plane of Fe_3O_4 (cubic, space group $Fd\bar{3}m$).

Another such example of these oxides is also presented in Figure 4.32. The FFT obtained from the region within the broken square gives one set of reflection. The measured lattice spacing only corresponds to (222) crystal plane of Fe_3O_4 (cubic, space group $Fd\bar{3}m$).

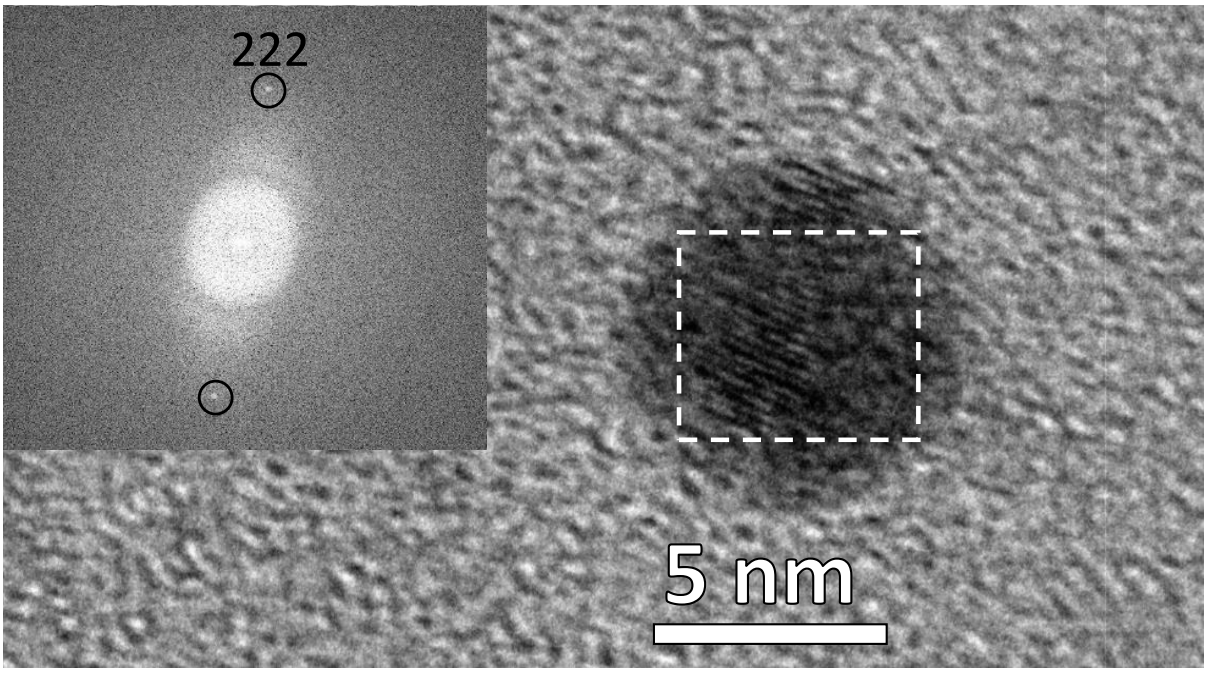

Figure 4.32: The fast Fourier transform of the high-resolution TEM image of the individual particle of diameter $\sim$ 7.5 nm within the broken square. (C) The black circles in FFT indicate a lattice spacing of 0.240 nm which corresponding to the (222) plane of Fe_3O_4 (cubic, space group $Fd\bar{3}m$).

The details of the relative weight abundance of various encapsulated single crystal phases (α-Fe, α-Fe and Fe_3C) and quality of fit indicators, extracted from the refinement of X-ray diffractograms in Figure 4.30 (A) and (B) are summarized in Table 4.8. For microstructural details, the summary of refined unit cell parameters is provided in Table 4.9.

Substrate	Relative abundance (wt.%)			Profile fit indicators		
	α-Fe	γ-Fe	Fe_3C	χ^2	R_p	wRp
High-roughness	60	11	29	2.357	0.0632	0.0864
Low-roughness	74	11	15	2.278	0.0321	0.0406

Table 4.8: Summary of the relative abundance of the encapsulated phases and quality of fit indicators, extracted from the Rietveld refinement of the X-ray diffractograms in Figure 4.30.

Substrate	Unit cell parameters (Å)					
	α-Fe ($Im\bar{3}m$)	γ-Fe ($Fm\bar{3}m$)	Fe_3C (*Pnma*)	1(C) *P6₃/mmc*	2(C) *P6₃/mmc*	Fe_3O_4 ($Fd\bar{3}m$)
High-roughness	2.868 (2)	3.580 (1)	5.073 (5) 6.760 (7) 4.529 (4)	2.472 (2) 2.474 (2) 6.814 (1)	2.460 (4) 2.460 (4) 6.704 (3)	8.367 (2)
Low-roughness	2.868 (2)	3.581 (1)	5.075 (5) 6.776 (9) 4.526 (5)	2.450 (2) 2.450 (2) 6.805 (1)	--- --- ---	8.349 (4)

Table 4.9: The unit cell parameters extracted from the X-ray diffraction data given in Figure 4.30 (A) and (B).

The extracted lattice parameter for α-Fe, 2.868 Å, corresponds to that of bulk ferromagnetic α-Fe. That for γ-Fe is less than the 3.6 Å for which antiferromagnetic behaviour is predicted but is greater than the expected lattice parameter of carbon-free γ-Fe (3.556 Å) at room temperature suggesting the likely incorporation of interstitial carbon atoms [45–47].

Surprisingly, (002) reflections from the graphitic shells labelled (2)C in Figure 4.30 (A) are not observed in Figure 4.30 (B) suggests that the graphitic shells are absent from the central core of the structures grown using the low-roughness substrate. The later has been confirmed by TEM inspection, Figure 4.33.

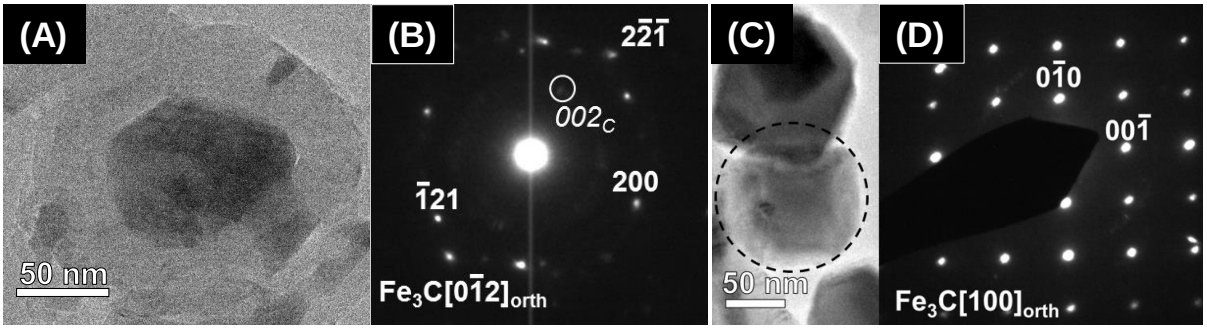

Figure 4.33: (A) Transmission electron micrographs of a graphite-encapsulated Fe_3C nanocrystals observed in the central core of a radial structure produced using the high-roughness substrate, and (B) the SAED pattern obtained from this particle. The highlighted zone axis is $Fe_3C\ [0\,\bar{1}2\,]_{\mathrm{orth}}$ with space group ($Pnma$). The $002_{\,C}$ spots originated from the inter-planer lattice spacing of the graphite shells around the Fe_3C particles. (C) Transmission electron micrograph of particle found in the central core of a radial structure produced using a low-roughness substrate, and (D) the SAED pattern obtained from the particle within the broken circle. The highlighted zone axis is $Fe_3C\ [100\,]_{\mathrm{orth}}$ with space group ($Pnma$).

In summary, the material produced using the low-roughness substrate has a smaller central core, fewer radial nanotubes, a higher α-Fe and lower Fe_3C content in the nanowire than that produced using the high-roughness substrate. The Fe_3C nanocrystals that comprise the central core are unencapsulated rather than encapsulated by a graphitic shell.

These observations can readily be explained by the surface degree of roughness impacting on the magnitude and duration of fluctuations in the boundary layer, which in turn intervenes in the self-organisational growth processes, Figure 4.34.

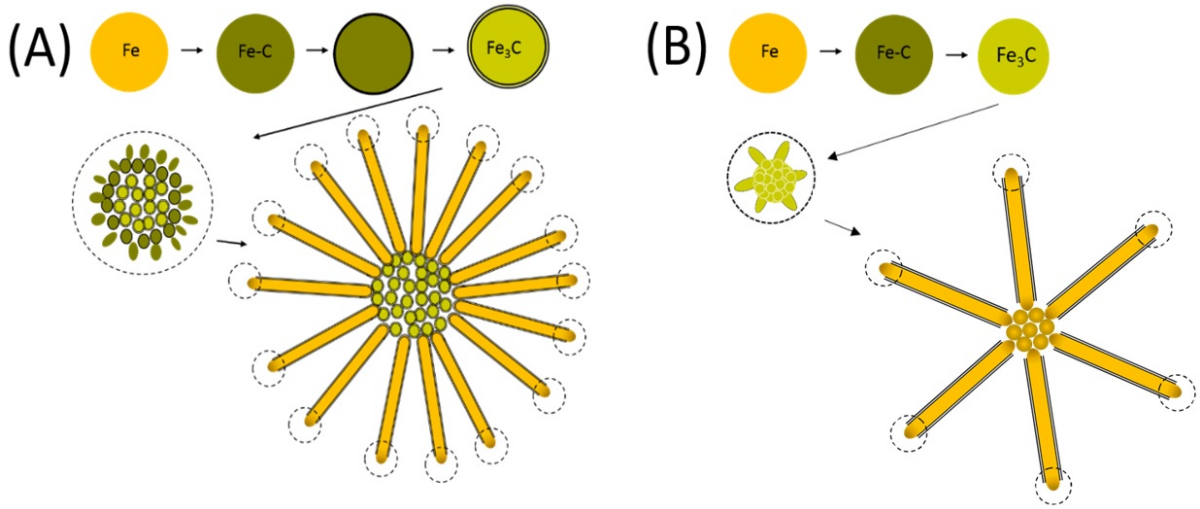

Figure 4.34: (A) Schematic illustration of the growth mechanism of the radial structures produced using the high-roughness substrates. The nucleating solid-phase iron particles which form in a vapour fluctuation catalytically decompose the hydrocarbon products of ferrocene decomposition (exothermic) resulting in carbon dissolution, single graphitic shell formation upon saturation (endothermic), multiple shell formation driven by carbon diffusion to the surface due the concentration gradient established by the shell formation, and subsequent graphitic encapsulation of Fe_3C. Central core formation is then by rapid agglomeration of these spherical structures; this creates an inward, spherically symmetrical diffusion gradient for the vapour feedstock (example concentration contours are given by the dashed lines). Peripheral Fe-C particles elongated by the spherical diffusion gradient provide the instability points from which radial nanotube and iron-based nanowire growth departs; vapour feedstock is now driven to the growth front at the tips of the nanotube by a thermal diffusion gradient created by the proximate endo- and exo-thermal processes (dashed circles at nanotube tips). (B) The low-roughness substrate produces weaker, shorter-lived fluctuations in the vapour flow therefore the nucleating particles do not become encapsulated, the core agglomeration is smaller and the fewer instability points result in fewer radial nanotubes. The length of the nanotube is determined by thermophoresis.

Conclusion:

We demonstrated that the degree of surface roughness used to produce iron-based nanowires encapsulated by radial carbon nanotubes by boundary layer chemical vapour synthesis can be used to tailor details of the structure and the composition of the nanowires. We have found that lowering of the fractal roughness results in fewer radial carbon nanotubes, unencapsulated rather than encapsulated Fe_3C nanocrystals form the central core, and a significant increase in α-Fe content with a corresponding decrease in Fe_3C content, while γ-Fe content remained unaffected.

4.4 Conclusion

Radial structures with high γ-Fe-content nanowires are successfully produced with the boundary layer chemical vapour synthesis. The evidence from this study suggests that high γ-Fe-content in the nanowires can be achieved at elevated temperatures. The γ-Fe crystallites in iron-based nanowires encapsulated by multiwalled carbon nanotubes are stabilised by dilute carbon alloying. The α-Fe/γ-Fe junctions in the nanowire are arranged sequentially. The α-Fe/Fe_3C junction, a coaxial arrangement exhibit the Bagaryatski orientation relationship: $[110]_{bcc} \parallel [100]_{orth}$. The indirect evidence suggests that the encapsulated γ-Fe is in the antiferromagnetic state at low temperature. Microscopic analysis of the relative abundances of the encapsulated phases under TEM confirms the presence of the encapsulated phases identified quantitatively by X-ray diffraction. We also demonstrated that the degree of surface roughness used to produce iron-based nanowires encapsulated by radial carbon nanotubes by boundary layer chemical vapour synthesis can be used to tailor details of the structure and the composition of the nanowires.

Chapter 5

Results and Discussion-II

5.1 Microstructure of encapsulated NiFe nanowires

This work was carried out in collboration with Dr. Mert Kurttepeli, Professor Gustaaf Van Tendeloo and Professor Sara Bals from EMAT, University of Antwerpen, Dr. Nadezda V. Tarakina and Dr. Rory M. Wilson, Queen Mary University of London.

NiFe alloy nanowires encapsulated by multiwalled carbon nanotube radial structures were synthesised by boundary layer chemical vapor synthesis by sublimating a 100 mg mixture of powder ferrocene and nickelocene in the weight ratio 1:1, to create a mixture of Ar-driven flowing vapour over a roughened quartz substrate. The substrate was located at a position within the reactor at temperature 921 °C. After complete sublimation of the metallocene powder, the reactor was cooled to 700 °C at its natural rate and held at this temperature for 1 hour before quenching to room temperature. The aim of the quenching was to retain γ-NiFe [40].

Scanning electron microscopy studies revealed thick deposit of ensemble of radial structures shown in the Figure 5.1. A closer inspection of the scanning electron micrographs depicts the presence of extended and elongated central cores in the radial structures 5.2.

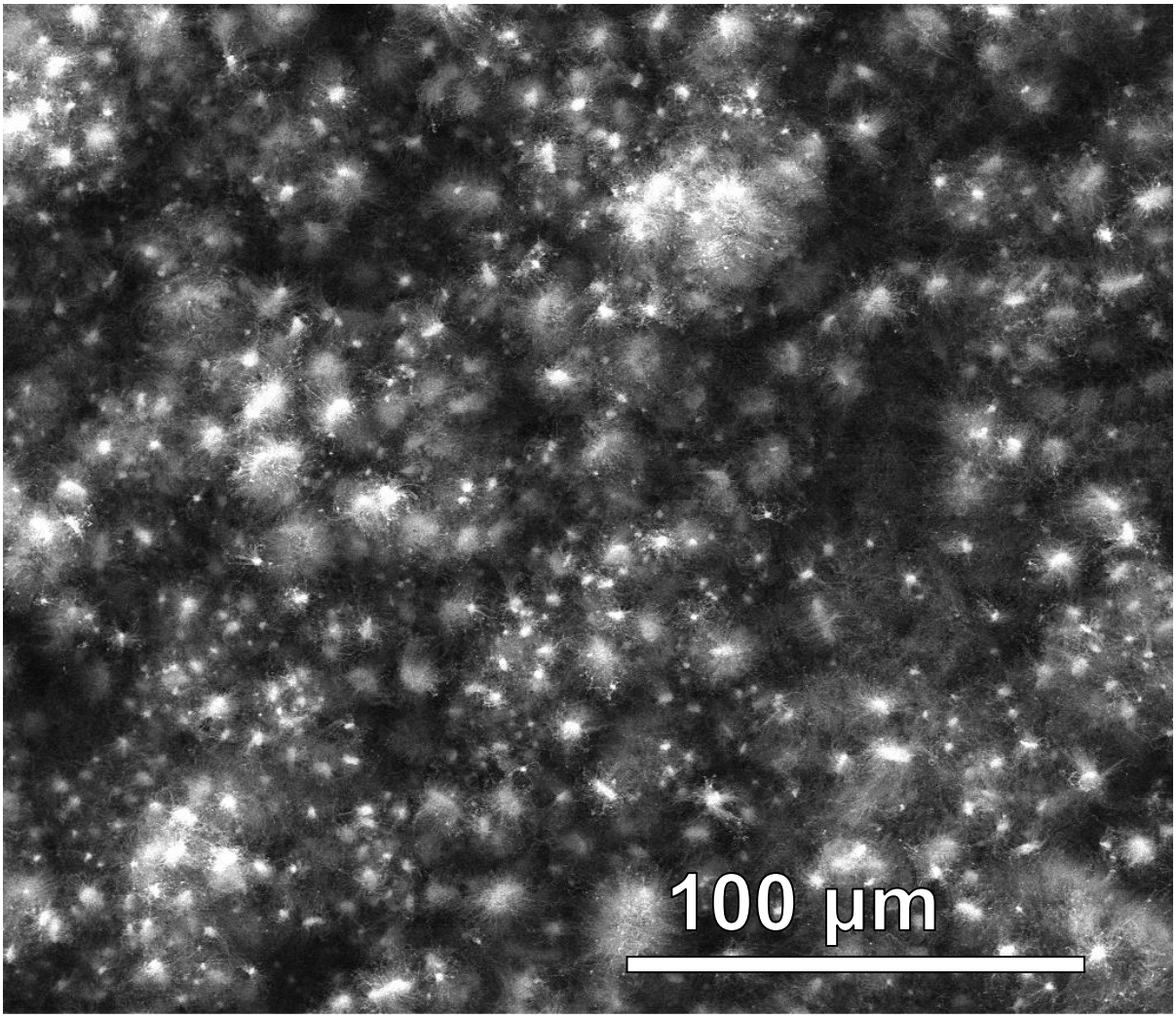

Figure 5.1: The scanning electron micrograph of an ensemble of the radial structures comprising NiFe nanowires encapsulated by multiwalled carbon nanotubes deposited on the surface of a roughened quartz substrate under Ar-driven ferrocene-nickelocene vapours in a conventional horizontal CVD reactor.

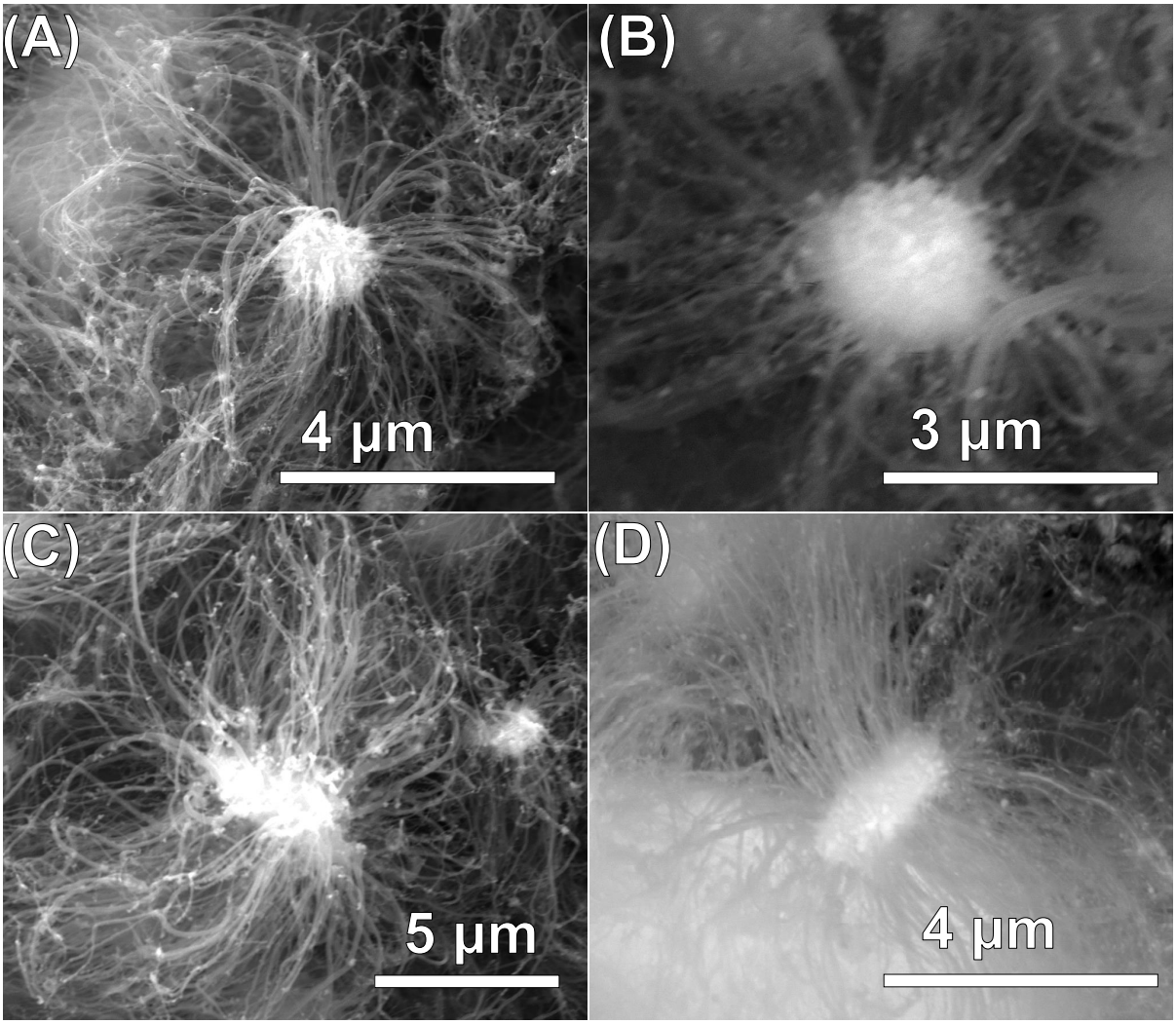

Figure 5.2: (A-D): The scanning electron micrographs of the typical individual radial structures comprising of NiFe nanowires encapsulated by multiwalled carbon nanotubes departing from a central core. (A) and (C) are the secondary electron micrographs and (B) and (D) are the backscattered electron micrographs of the individual structures. (C) and (D) are examples of the elongated central cores.

Figure 5.3 is a transmission electron micrograph showing an individual elongated central core of diameter about 5 μm. The peripheral nanotubes are detached by the ultrasonication process used to prepare the sample, Figure 5.3.

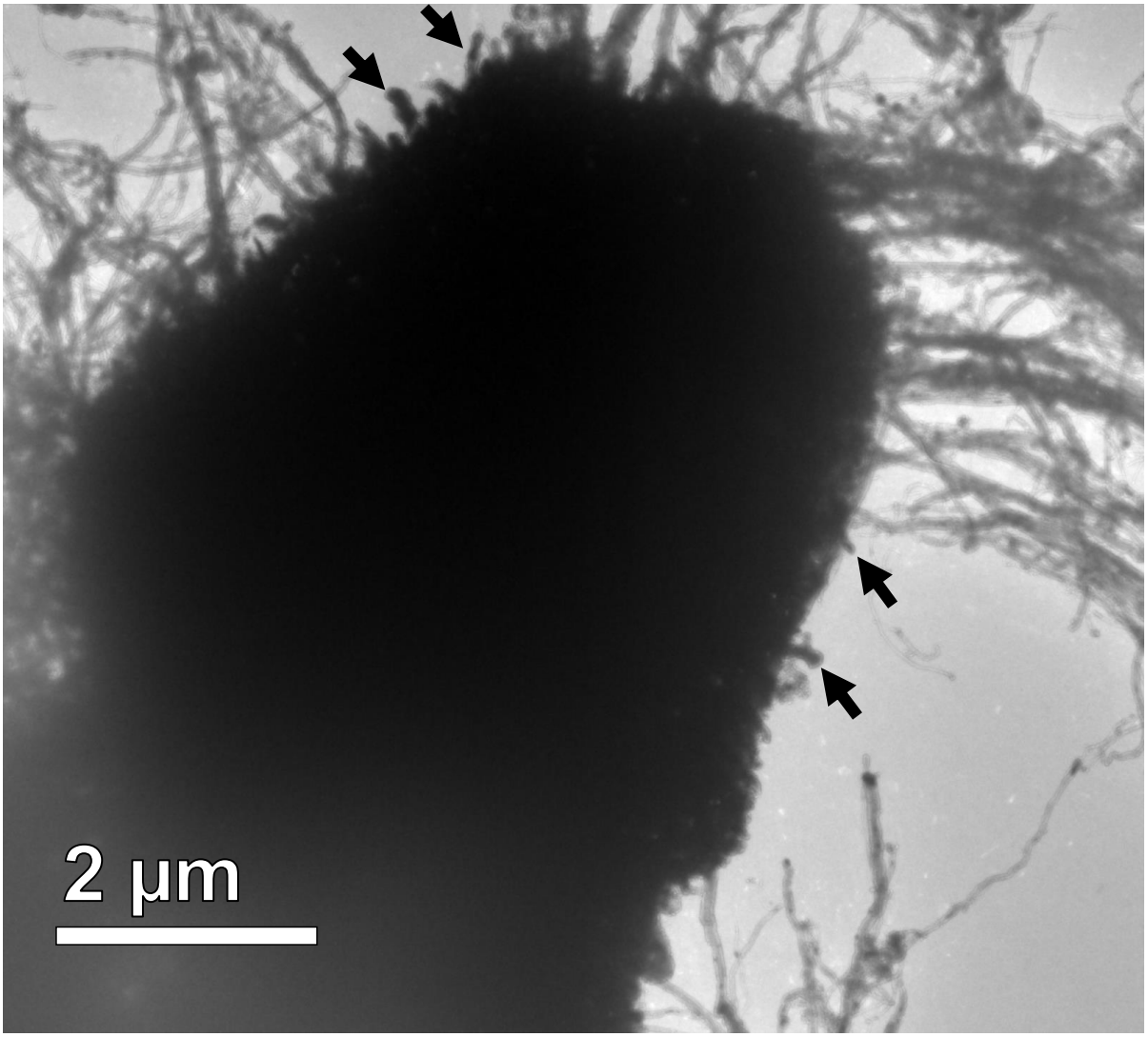

Figure 5.3: Transmission electron micrograph showing an example of the elongated central core of diameter ($\sim$ 5 μm) of a radial structure. The broken edges of the nanotubes are indicated by the arrows. The detachment of the nanotubes from the central core resulted from the ultrasonication process used to prepare the sample.

X-ray powder diffraction data and Rietveld refinement of the substrate deposits is provided in Figure 5.4.

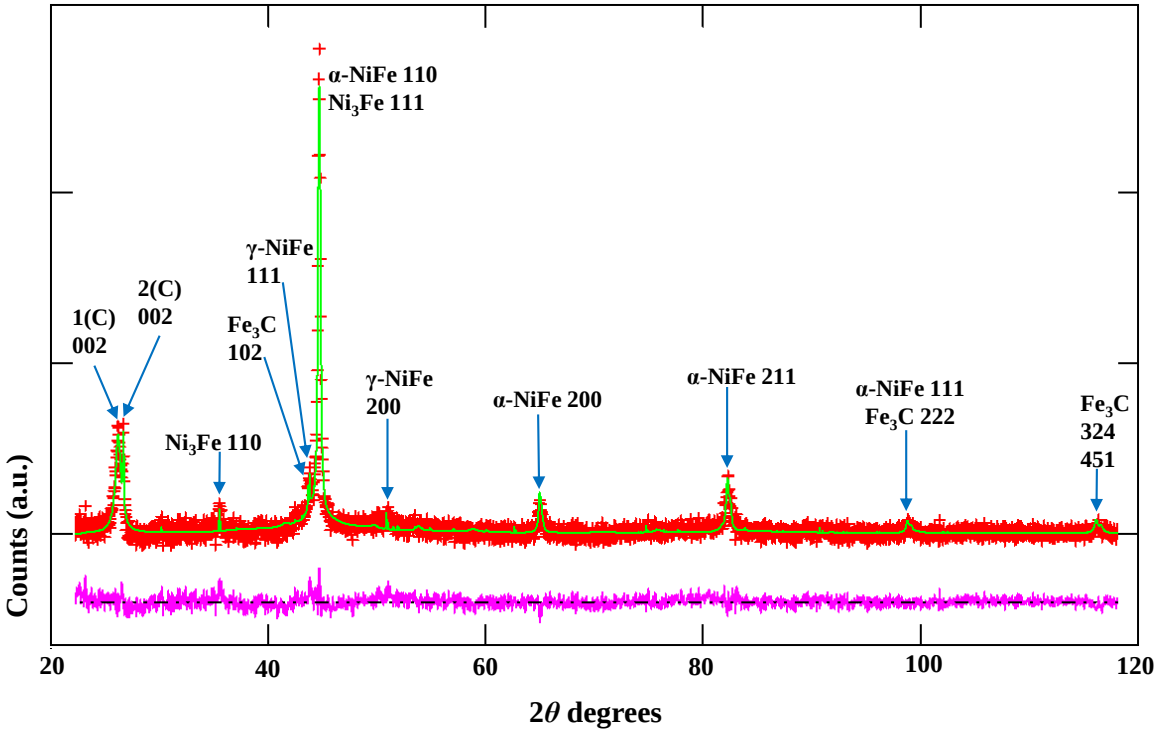

Figure 5.4: X-ray diffractogram data (red), the Rietveld refinement (green) and difference (purple) for a powder extracted from the roughened quartz substrate on collection from the reactor after synthesis and then annealing for 1 hour at 700°C, followed by a rapid quench to room temperature. Arrows denote the crystal planes attributed to each intensity peak. The extracted relative weight abundances of the encapsulated phases are 72% of α-NiFe ($Im\bar{3}m$), 12% of γ-NiFe ($Fm\bar{3}m$), 7% Ni_3Fe ($Pm\bar{3}m$) and 9% Fe_3C ($Pnma$).

The details of the relative abundance of the encapsulated phases and quality of fit indicators are summarised in Table 5.1. The extracted unit cell parameters are also provided in Table 5.2.

Relative abundance (wt.%)				Profile fit indicators		
α-NiFe ($Im\bar{3}m$)	γ-NiFe ($Fm\bar{3}m$)	Ni_3Fe ($Pm\bar{3}m$)	Fe_3C (*Pnma*)	χ^2	R_p	wRp
72	12	7	9	1.509	0.0336	0.0440

Table 5.1: Summary of the relative abundances of the encapsulated phases and the quality of fit indicators, extracted from the Rietveld refinement of the X-ray diffractogram in Figure 5.4.

Unit cell parameters (Å)					
α-NiFe ($Im\bar{3}m$)	γ-NiFe ($Fm\bar{3}m$)	Ni_3Fe ($Pm\bar{3}m$)	Fe_3C *(Pnma)*	1(C) *$P6_3/mmc$*	2(C) *$P6_3/mmc$*
2.870 (1)	3.597 (1)	3.553 (1)	5.089 (1)	2.470 (3)	2.510 (3)
			6.731 (1)	2.470 (3)	2.510 (3)
			4.527 (1)	6.800 (2)	6.803 (3)

Table 5.2: The unit cell parameters of the various phases extracted from X-ray diffractogram given in Figure 5.4.

Reflections from the encapsulated phases were analysed in terms of the following components: α-NiFe ($Im\bar{3}m$, ICSD Chemical Database Ref. 103560), γ-NiFe ($Fm\bar{3}m$, ICSD Chemical Database Ref. 632933), Ni_3Fe ($Pm\bar{3}m$, ICSD Chemical Database Ref. 103557) and Fe_3C ($Pnma$, Crystal Open Database Ref. 16593). The relative weight abundances of the encapsulated phases obtained from this data are 72% of α-NiFe ($Im\bar{3}m$), 12% of γ-NiFe ($Fm\bar{3}m$), 7% Ni_3Fe ($Pm\bar{3}m$) and 9% Fe_3C ($Pnma$). The lower angle graphitic carbon peak, (1)C, corresponding to the 002 reflection from graphite (space group $P6_3/mmc$, ICSD Chemical Database Ref. 53781), originate from the graphitic walls of the multiwall carbon nanotubes, inter-wall spacing 0.34 nm [10]. The second graphitic peak, (2)C, corresponds to the lattice spacing 0.33 nm (002 peak of graphite hexagonal $P6_3/mmc$, ICSD Chemical Database Ref. 52230) of the graphitic shell of the spherical particles that comprise the core of the radial structures [10].

Neither elemental peaks of Ni and Fe were observed nor evidence of their oxides were observed in the diffractogram (Figure 5.4). Surprisingly, although a low content Fe_3C was observed but there was no evidence for the presence of Ni_3C. The carbides of these metals are considered to be essential intermediates for the growth of the carbon nanotubes. None of the metal carbides (Fe_3C or Ni_3C) have been previously found and reported in the encapsulated NiFe nanowires synthesized by conventional solid- and liquid-source CVD method [34, 38, 39, 56, 68]. In addition, these reports neither comment on the absence of metal carbides in the final product nor provide a description of the growth mechanism.

The presence of Fe_3C and the absence of Ni_3C peaks in Figure 5.4 suggests the higher catalytic activity exhibited by Fe compared to Ni [146]. Mordkovich *et al.* reported the suppression of the catalytic activity of Ni as a result of competition between Ni and Fe in NiFe catalyst particles and that the growth of carbon nanotubes is initialized and dominated by Fe [146]. However, the uniform spatial distribution of Ni into Fe throughout the encapsulated nanowire in EDX-STEM maps, Figure 5.5, suggests the likely possibility of the carbon nanotube growth directly from a NiFe catalyst particle. Therefore, the central core-agglomeration of the radial structures could be either composed of only spherical Fe_3C nanocrsytals or it could be composed of NiFe catalyst particles.

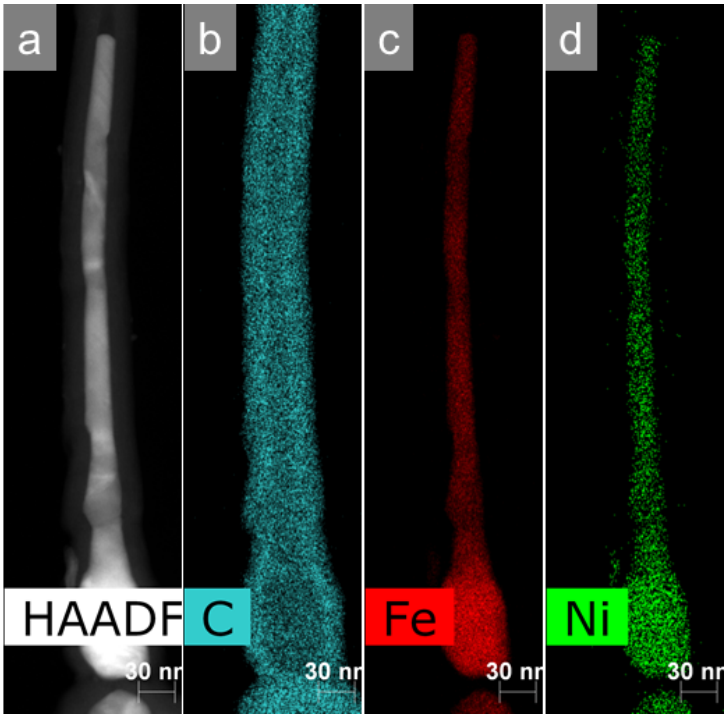

Figure 5.5: High-angle annular dark field (HAADF) image on the left and EDX-STEM maps of the NiFe nanowire show the uniform spatial distribution of Ni into Fe in the nanowire encapsulated by multiwalled carbon nanotubes.

The core particle was inaccessible by transmission electron microscopy owing to its micrometer-scale dimensions. However, elongation is most likely due to the elongation of the fluctuating eddies as result of lowering of the viscosity of the boundary layer through multiple metallocene vapour usage [1].

An example of a continuous α-NiFe encapsulated nanowire detached from the core as a result of ultrasonication is presented in the Figure 5.6. The nanowire was probed at different locations by selective area electron diffraction patterns obtained from 160 nm diameter areas within the broken circles shown in Figure 5.6 (A-D). The SAED patterns revealed differing crystallographic orientations exhibited by the α-NiFe nanowire relative to the nanotube, Figure 5.6.

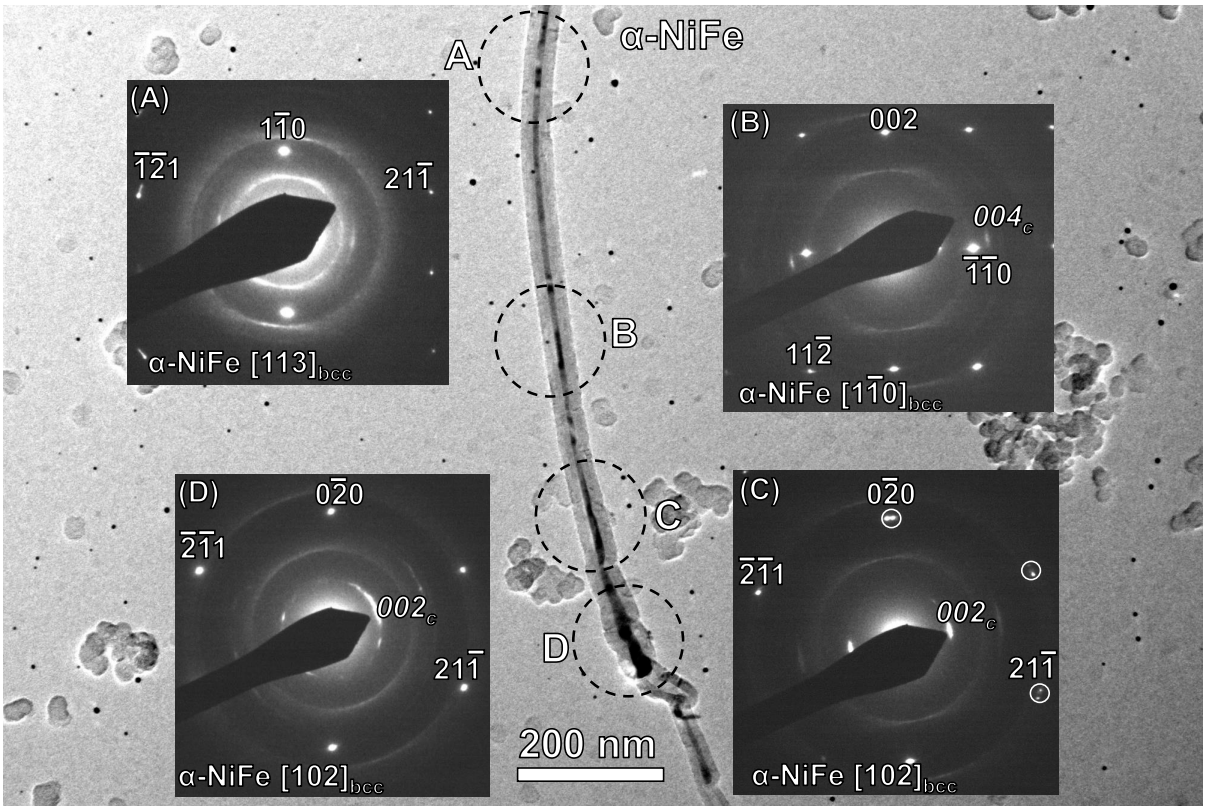

Figure 5.6: Transmission electron micrograph of the encapsulated α-NiFe nanowire with differing crystallographic orientations relative to the nanotube axis are indicated in the selective area electron diffraction patterns (A-D). Each diffraction pattern is taken from the image-plane electron beam areas of diameter 160 nm and are indicated by the broken circles. The highlighted zone axes are also indicated in each pattern: (A) α-NiFe $[113]_{bcc}$, (B)α-NiFe $[1\,\bar{1}0]_{bcc}$, (C) α-NiFe $[102]_{bcc}$ and (D) α-NiFe $[102]_{bcc}$. The 002_C and 004_C reflections of the graphitic nanotube walls correspond to an inter-wall spacing of 0.34 nm and agrees with the value calculated from the Bragg peak labbled 1(C) in Figure 5.4.

High-resolution transmission electron micrographs showing graphitic enclosure features in the internal cavity of the nanotubes exhibited by the encapsulated of γ-NiFe and α-

NiFe, Figure 5.7. Black arrows are indicating graphitic enclosures in the internal cavity of the nanotubes at room temperature. In literature, such features are generally observed under high electron beam irradiation of the encapsulated nanowires, where growth of carbon nanotubes occurs from a single crystal Fe-based nanowires in the host nanotube at a specimen temperature of 600 °C [141, 147, 148]. The γ-NiFe reflection from (111) crystal plane is oriented parallel to the nanotube axis inferred from the $002_{\,C}$ reflection in the FFT (Figure 5.7(B)).

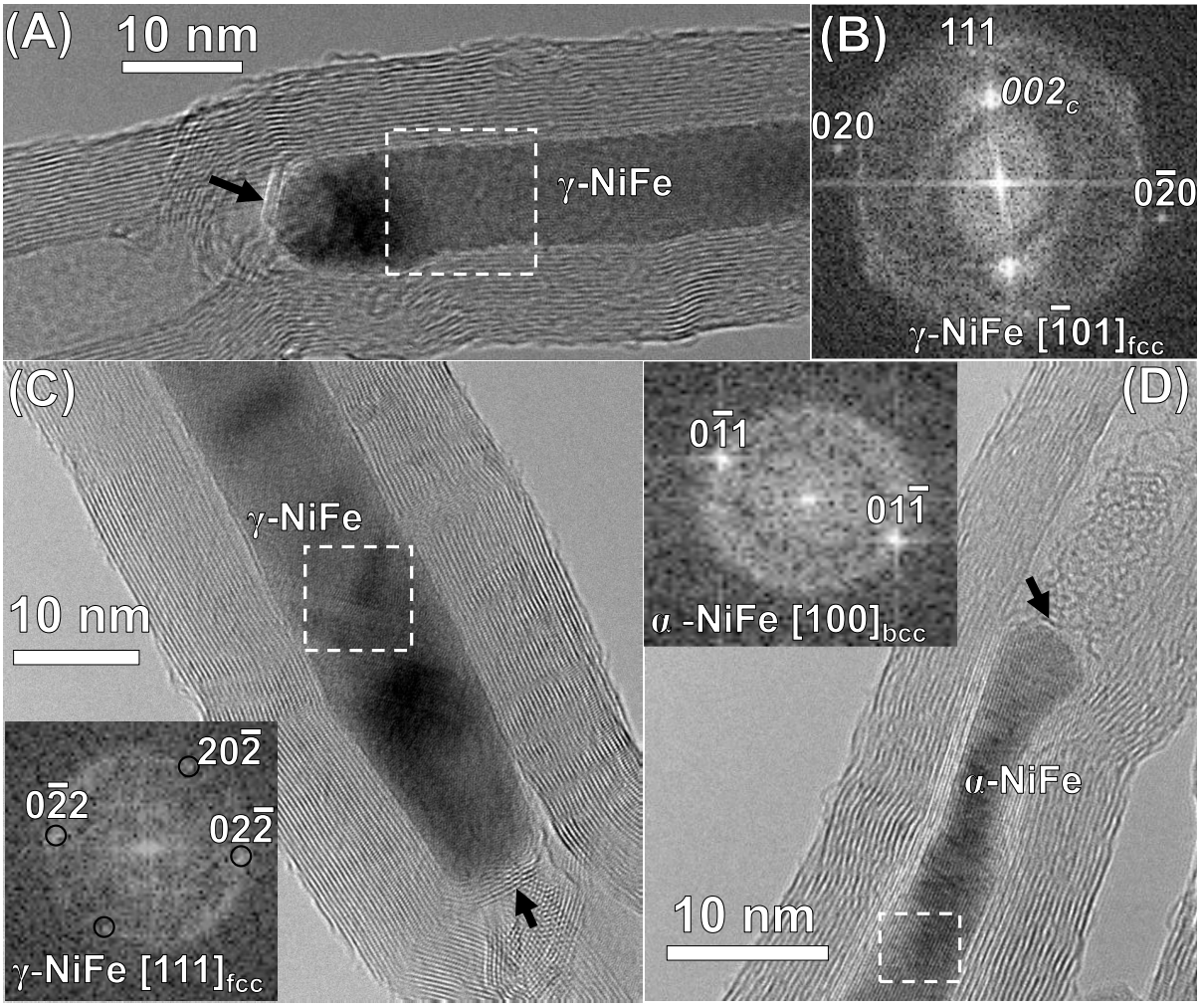

Figure 5.7: (A-C-D) HRTEM images showing examples of nanowires encapsulated by multiwalled carbon nanotubes with graphitic enclosures in the internal cavity of the nanotube (indicated by black arrows). (A) γ-NiFe nanowire, (B) is the FFT taken from the region within the broken square in (A) along the $[\bar{1}01]_{\text{fcc}}$ direction, (C) γ-NiFe nanowire having a jet-type tip with graphitic enclosure and FFT shown in the inset is taken along $[111]_{\text{fcc}}$ direction from the region within the broken square. (D) α-NiFe nanowire with carbon graphitizing from the tip of the nanowire in the internal cavity of the nanotube indicated by a black arrow. Inset is the FFT taken from the region within the broken square along $[100]_{\text{bcc}}$.

Figure 5.8 (A) is an overview of an encapsulated α-NiFe nanowire. An HRTEM image shown in (B) is obtained from the area within the broken circle in (A). The inset in (B) is the FFT taken from the area within the broken square along $[111]_{\text{bcc}}$ direction. The region enclosed by the two dashed ovals in Figure 5.8 (B) and (C) show the carbon nanotubes walls are terminating at the ledges of the nanowire. Such observation is

associated with the characteristic mechanism of low temperature post-synthesis catalytic growth and nucleation of carbon nanotubes from catalyst facets [149]. From a closer inspection of the $(0\,\bar{1}1)$ crystal planes of the α-NiFe nanowire and the graphitic layers of the nanotube, it can be seen that the two replaces each other (an oval region in Figure 5.8 (C)). Such features have been reported for α-Fe nanowire and is referred as faceting and step bunching mechanism for catalytic growth [149]. These features could also be useful to tailor the surface structure, surface chemistry, and surface magnetic properties of the nanowires.

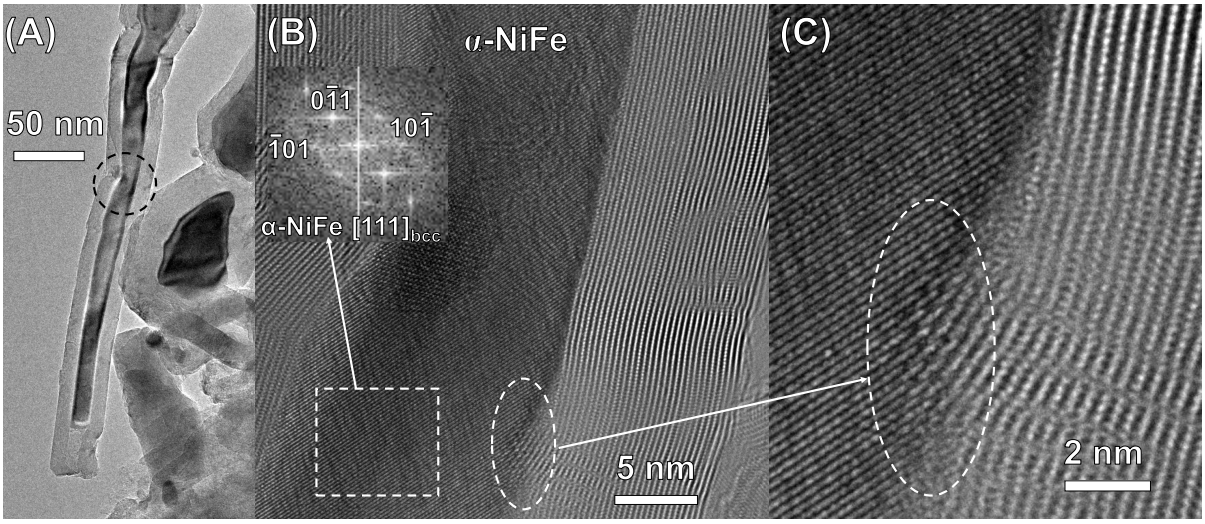

Figure 5.8: (A) TEM image showing overview of an encapsulated α-NiFe nanowire. (B) HRTEM of the region within the broken circle in (A), FFT is taken from the square region along $[111]_{\mathrm{bcc}}$ direction showing the orientation of atomic planes and (C) is the zoomed-in image showing the termination of the nanotube walls at the ledges of the nanowire, the two ovals are guides to eye of this particular feature.

A TEM image of γ-NiFe encapsulated nanowire is presented in Figure 5.9 (A). The SAED pattern is taken from the region within the broken circle (Figure 5.9 (B)) and we identified it as γ-NiFe with a low-index zone axis $[111]_{\mathrm{fcc}}$. The $002_{\,\mathrm{C}}$ reflection of the graphitic carbon corresponds to a lattice spacing of 0.34 nm originated from the inter-layer spacing of multiwalled carbon nanotube and is in agreement with the value calculated from 1(C) reflection from graphitic nanotube walls in X-ray diffractogram, Figure 5.4.

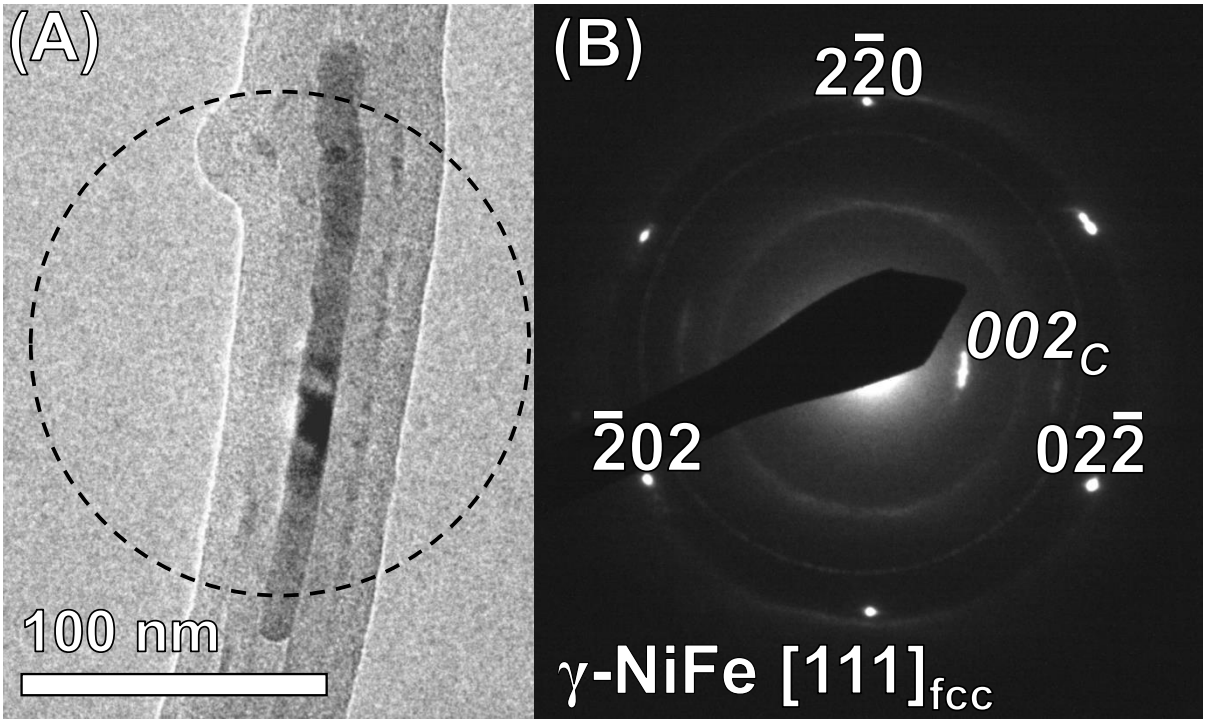

Figure 5.9: TEM image of the γ-NiFe nanowire encapsulated by multiwalled carbon nanotubes. (B) Selective area electron diffraction pattern taken from the area within the broken circle along the $[111]_{fcc}$ direction.

An example of a Ni_3Fe encapsulated nanowire is presented in Figure 5.10. The inset in Figure 5.10 is the FFT of the image taken from the region within the broken square along the direction [111], it shows a set of low-intensity reflections from $(1\,\bar{1}0)$ and $(10\,\bar{1})$ corresponding to crystal planes of Ni_3Fe with space group $(Pm\bar{3}m)$ and the 002_C of the graphitic carbon reflection corresponds to 0.345 nm originated from the interlayer spacing of the multiwalled carbon nanotube. No preferential orientation has been exhibited relative to the nanotube axis indicated by 002_C.

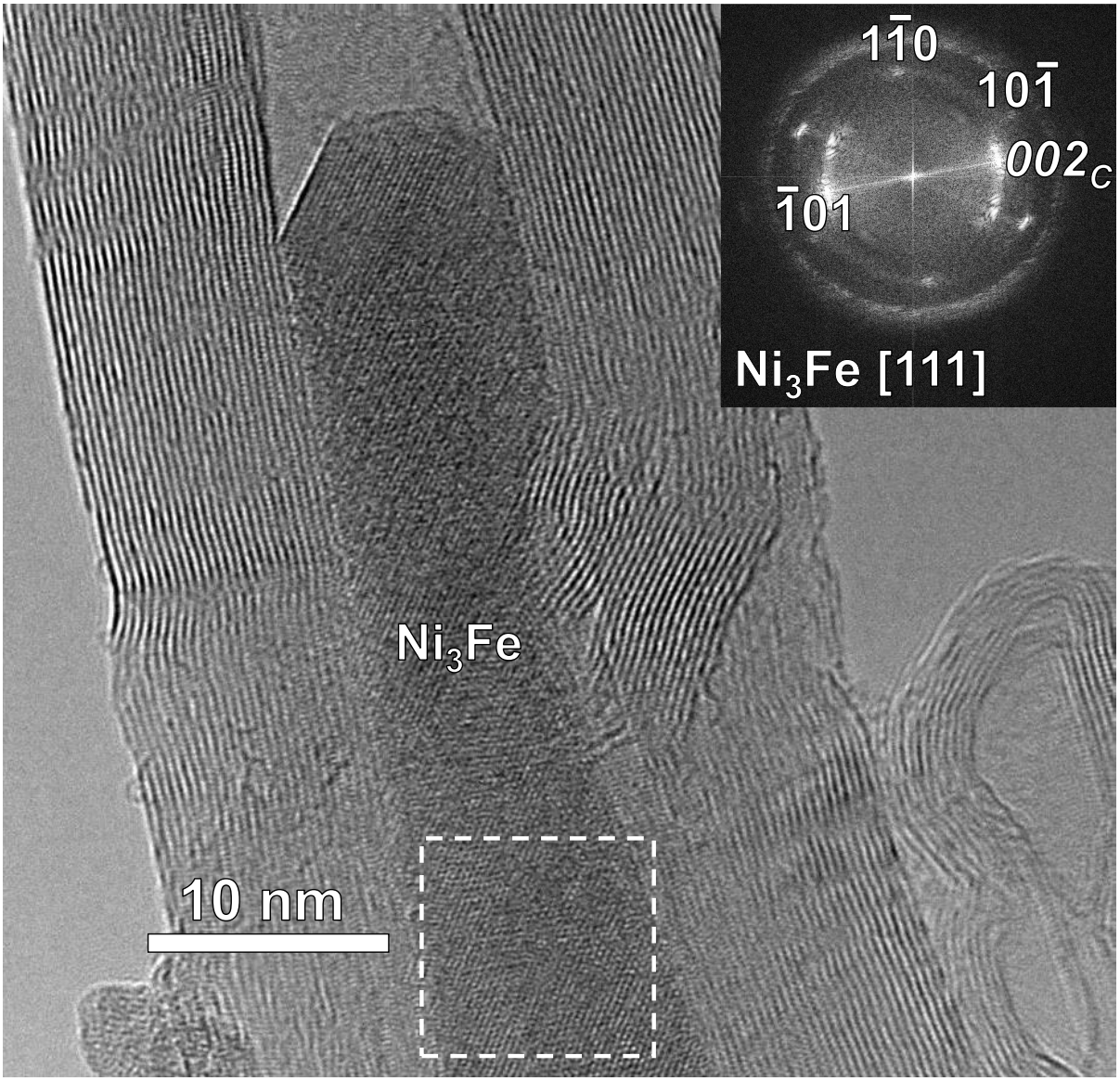

Figure 5.10: HRTEM image of the Ni_3Fe nanowire encapsulated by a multiwalled carbon nanotube. Inset is the fast Fourier transform taken from the region within the broken square. The $(1\,\bar{1}0)$ and $(10\,\bar{1})$ are low-intensity reflections in Ni_3Fe [111], which are forbidden reflections in γ-NiFe [111] and γ-Fe [111].

HRTEM investigations revealed the presence of γ-NiFe/Ni_3Fe junctions in the encapsulated nanowires, Figure 5.11. The junction is indicated by a black arrow. The inset (A) is the FFT taken from the region within the broken square labelled A of the nanowire along $[1\,\bar{1}0]_{\text{fcc}}$ direction and identified as γ-NiFe with space group ($Fm\bar{3}m$). Inset (B) is the FFT taken from the region within the broken square labelled B along the $[\bar{1}01]$

direction and identified as Ni_3Fe with a space group ($Pm\bar{3}m$).

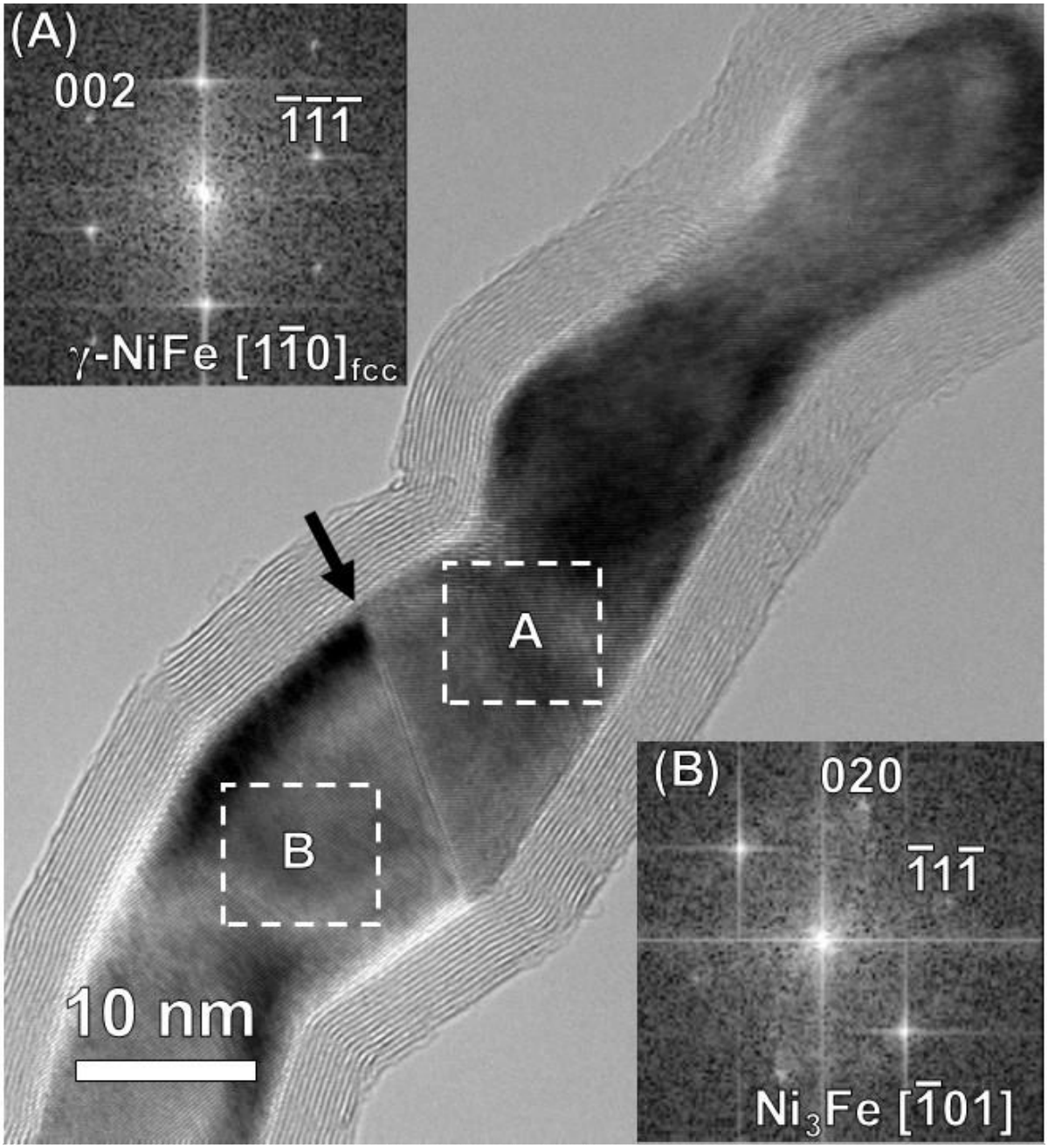

Figure 5.11: HRTEM image of γ-NiFe/Ni_3Fe junction in the NiFe nanowire encapsulated by multiwalled carbon nanotubes, the junction is marked by a black arrow. (A) FFT of the image taken from the region within the broken square-A, (B) FFT of the image taken from the region within the broken square-B.

Figure 5.12 is an HRTEM image of an encapsulated nanowire containing a α-NiFe/γ-NiFe junction. The insets (A) and (B) are the FFTs of the images taken from the areas

within the broken squares labelled A, and that labelled B both along $[111]_{bcc}$ direction and is identified as α-NiFe. Inset (C) is the fast Fourier transform taken from the region within the broken square labelled C along $[\bar{1}01]_{fcc}$ and is identified as γ-NiFe.

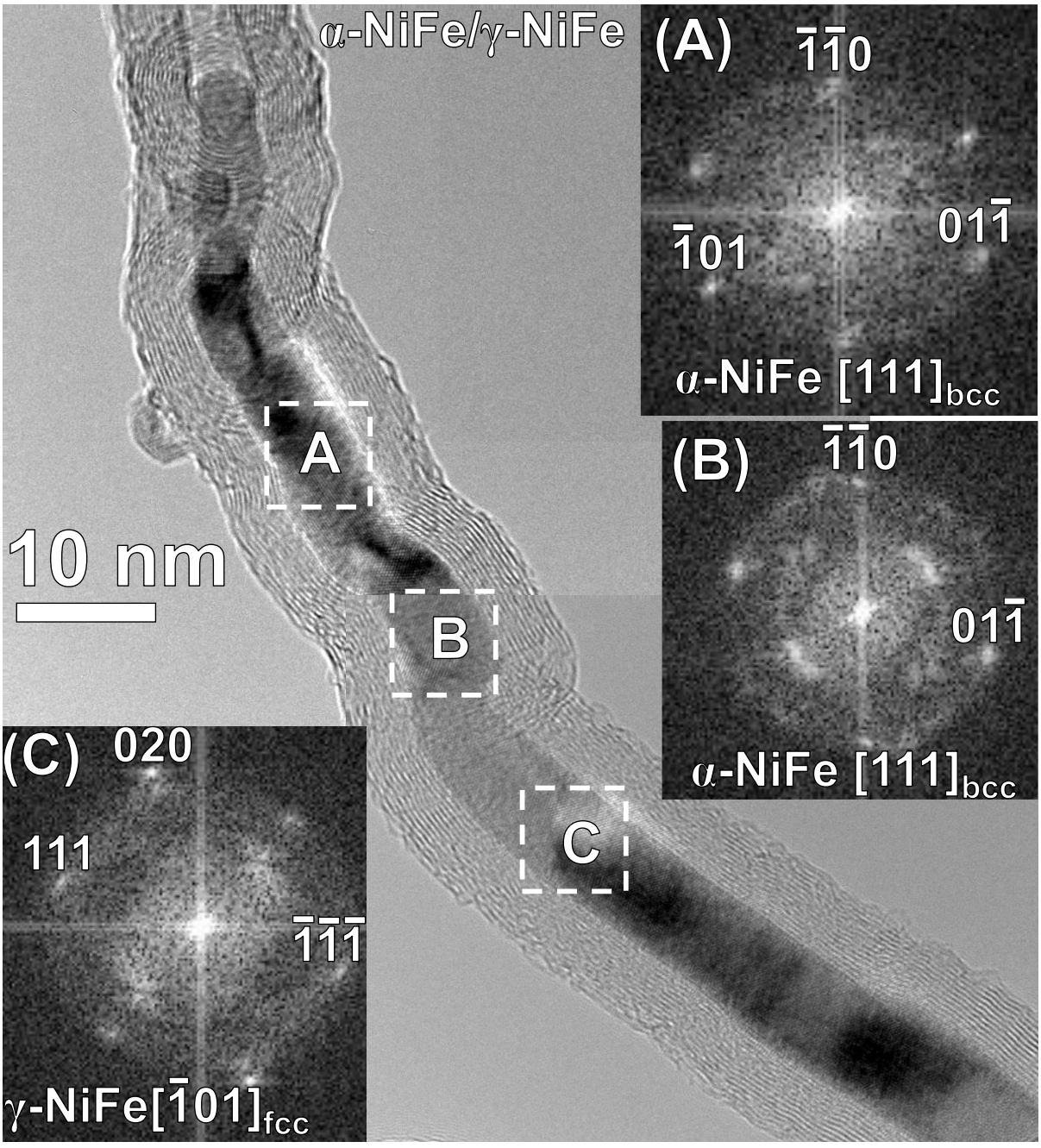

Figure 5.12: HRTEM image of an α-NiFe/γ-NiFe junction in a NiFe-nanowire encapsulated by multiwalled carbon nanotubes, junction is marked by a black arrow. (A) and (B) are the FFTs taken from the region within the broken square-A and B, both indexed as α-NiFe $[111]_{bcc}$. (C) FFT taken from the region within the broken square-C and is indexed as γ-NiFe $[\bar{1}01]_{fcc}$.

5.2 Conclusion

From the microstructural analysis, we have found that NiFe nanowires crystallites are mainly in the α-NiFe phase, γ-NiFe and a low content of Ni_3Fe. The γ-NiFe/ Ni_3Fe and α-NiFe/γ-NiFe junctions are arranged sequentially. We also found an evidence confirming the graphitic layers can grow from the atomic planes of a single-crystal nanowire. The evidence from this study also provides a proof of uniform spatial distribution of Ni into Fe throughout the encapsulated nanowire encapsulated by multiwalled carbon nanotubes. This feature is useful for tuning the magnetic properties of these structures for various applications.

Chapter 6

Conclusion

Boundary layer chemical vapour synthesis has been extensively employed for the production of radial structures comprising of Fe-based and NiFe nanowires encapsulated by multiwalled carbon nanotubes. The work presented in this thesis has shown the production of radial structures with high γ-Fe-content nanowires. Detail microstructural analysis has provided a deeper understanding of the unknown microstructure and concluded the first observation of α-Fe/γ-Fe junctions in the encapsulated nanowires. The degree of substrate roughness was found to be a means of tailoring details of the structure and composition of the encapsulated nanowires. Microstructural analysis of NiFe encapsulated nanowires revealed crystallites of α-NiFe, γ-NiFe and Ni_3Fe exhibiting sequential junctions γ-NiFe/Ni_3Fe and α-NiFe/γ-NiFe of unknown magnetic response.

In the following specific conclusions concerning each chapter of the results are listed:

1. Radial structures with low and high γ-Fe-content nanowires

   (i) Radial structures with high γ-Fe-content nanowires can be synthesised at elevated temperatures.

   (ii) We found that increase in γ-Fe-content of the nanowires increases the probability of formation of α-Fe/γ-Fe junctions.

   (iii) Finally, the approach is useful for producing radial structures with high density

of α-Fe/γ-Fe junctions.

2. First observation of α-Fe/γ-Fe junctions

   (i) By analysis of the local microstructure we concluded that the γ-Fe crystallites in iron-based nanowires encapsulated by multiwalled carbon nanotubes are stabilised by dilute carbon alloying.

   (ii) We also conclude that the first observation of α-Fe/γ-Fe junctions in the nanowires is of the sequential type.

   (iii) The α-Fe/Fe_3C junction exhibit the Bagaryatski orientation relationship: $[110]_{bcc} \parallel [100]_{orth}$.

   (vi) Indirect evidence suggests γ-Fe is in the antiferromagnetic state at low temperature.

3. The role of substrate roughness in the boundary layer synthesis

   (i) We have found that the degree of surface roughness used to produce iron-based nanowires encapsulated by radial carbon nanotubes by boundary layer chemical vapour synthesis can be used to tailor details of the structure and the composition of the nanowires.

   (ii) Lowering of the fractal roughness resulted in fewer radial carbon nanotubes, unencapsulated rather than encapsulated Fe_3C nanocrystals form the central core, and a significant increase in α-Fe content with a corresponding decrease in Fe_3C content, while γ-Fe content remained unaffected.

   (iii) The low-roughness substrate produces weaker, shorter-lived fluctuations in the vapour flow therefore the nucleating particles do not become encapsulated, the core agglomeration is smaller and the fewer instability points result in fewer radial nanotubes. The length of the nanotube is determined by thermophoresis.

4. Microstructure of encapsulated NiFe nanowires

(i) Boundary layer chemical vapour synthesis using multiple metallocene (ferrocene and nickelocene) vapour has been successfully employed to synthesise radial structures comprising NiFe alloy nanowires encapsulated by multiwalled carbon nanotubes departing from central core agglomeration. This result provides an alternative route for production of encapsulated NiFe alloy nanowires.

(ii) From the microstructural analysis, NiFe nanowires have been mainly crystallised in α-NiFe phase and γ-NiFe and a low content of Ni_3Fe has also been observed. The high volume fraction of α-NiFe nanowires encapsulated by MWCNTs exhibit differing crystallographic orientations relative to the nanotube axis.

(iii) The absence of Ni_3C and the presence of the Fe_3C suggest lower catalytic activity exhibited by Ni compared to Fe.

(iv) No elemental peak of Fe and Ni has been observed in X-ray diffractogram and the absence of their respective oxides peaks confirm the absence of post-synthesis non-encapsulated elemental traces of these elements.

(v) The appearance of 2(C) peaks corresponding to 002 graphitic interplaner spacing 0.33 nm, confirm the presence of graphitic shell around the spherical particles in core-agglomeration of the radial structures.

(vi) We have found an evidence confirming the graphitic layers growth from atomic planes of the single-crystal α-NiFe nanowire.

(viii) The observation of sequential type junctions in the encapsulated nanowires; γ-NiFe/ Ni_3Fe and α-NiFe/γ-NiFe are of unknown magnetic response.

(ix) EDX-STEM analysis confirmed uniform spatial distribution of Ni into Fe throughout the nanowire encapsulated by multiwalled carbon nanotubes and this particular feature of NiFe nanowires is useful for tuning the Curie temperature of these alloys through relative concentration of Ni and Fe.

The first observation of sequentially arranged α-Fe/γ-Fe junctions is a new attribute of suitability and usefulness of the revealed microstructure of the encapsulated nanowires for magnetocaloric application in addition to the previously known attributes of the radial structures. Indirect evidence from magnetisation measurements presented in this work suggests that γ-Fe is in the antiferromagnetic state at low temperature. But the exact magnetic state of γ-Fe cannot be confidently determined from this measurement. There is a need to know the exact magnetic state of the γ-Fe, whether it is ferromagnetic, antiferromagnetic or non-magnetic. A useful approach would be to determine the magnetic state of γ-Fe and response of the α-Fe/γ-Fe junction using magnetic force microscopy or electron holography and this is a part of the future work. The junctions γ-NiFe/ Ni_3Fe and α-NiFe/γ-NiFe in NiFe nanowires are also of sequential type, but with unknown magnetic state of the individual phases and the unknown magnetic response of the junctions. These junctions might be useful for future potential applications once the magnetic state of the individual encapsulated phases and the junctions response is unveiled.

Chapter 7

Future work

Magnetic force microscopy measurements would be very useful to detect the magnetic state of various encapsulated phases and in particular the magnetic state of γ-Fe, i.e. whether it is ferromagnetic, antiferromagnetic or nonmagnetic. Using MFM measurements, an individual Fe-based nanowire could be probed. The presence of α-Fe/γ-Fe junctions would be confirmed by an abrupt change in magnetization across the junction provided that the magnetic state of the two phases are different.

Off-axis electron holography can be used to reveal the micromagnetic structure and study the magnetic properties of encapsulated nanowires. The magnetic induction maps need to be recorded from individual nanowires to identify α-Fe/γ-Fe junctions. This technique provides high spatial resolution and quantitative magnetic information that cannot be obtained through MFM and magnetometry [150].

Bibliography

[1] F. S. Boi, R. M. Wilson, G. Mountjoy, M. Ibrar, and M. Baxendale, "Boundary layer chemical vapour synthesis of self-organised ferromagnetically filled radial-carbon-nanotube structures," *Faraday Discussion*, vol. 173, no. 0, pp. 67–77, 2014.

[2] O. Tegus, E. Brück, K. Buschow, and F. De Boer, "Transition-metal-based magnetic refrigerants for room-temperature applications," *Nature*, vol. 415, no. 6868, pp. 150–152, 2002.

[3] `https://www.ugent.be/we/solidstatesciences/dynamat/en/research`.

[4] P. M. Ajayan and O. Z. Zhou, *Applications of carbon nanotubes*. Springer, 2001.

[5] C. Chen and Y. Zhang, *Nanowelded Carbon Nanotubes: From Field-Effect Transistors to Solar Microcells*. Springer Science & Business Media, 2009.

[6] P. Visconti, P. Primiceri, D. Longo, L. Strafella, P. Carlucci, M. Lomascolo, A. Cretì, and G. Mele, "Photo-ignition process of multiwall carbon nanotubes and ferrocene by continuous wave Xe lamp illumination," *Beilstein journal of nanotechnology*, vol. 8, p. 134, 2017.

[7] R. Baker, "Catalytic growth of carbon filaments," *Carbon*, vol. 27, no. 3, pp. 315–323, 1989.

[8] Y. Yan, J. Miao, Z. Yang, F.-X. Xiao, H. B. Yang, B. Liu, and Y. Yang, "Carbon nanotube catalysts: recent advances in synthesis, characterization and applications," *Chemical Society Reviews*, vol. 44, no. 10, pp. 3295–3346, 2015.

[9] U. Weissker, S. Hampel, A. Leonhardt, and B. Büchner, "Carbon nanotubes filled with ferromagnetic materials," *Materials*, vol. 3, no. 8, pp. 4387–4427, 2010.

[10] F. S. Boi, G. Mountjoy, and M. Baxendale, "Boundary layer chemical vapor synthesis of self-organized radial filled-carbon-nanotube structures," *Carbon*, vol. 64, no. 516, 2013.

[11] Z. Basinski, W. Hume-Rothery, and A. Sutton, "The lattice expansion of iron," in *Proceedings of the Royal Society of London A: Mathematical, Physical and Engineering Sciences*, vol. 229, pp. 459–467, The Royal Society, 1955.

[12] W. D. Callister and D. G. Rethwisch, *Materials science and engineering*, vol. 5. John Wiley & Sons NY, 2011.

[13] W. H. Meiklejohn and C. P. Bean, "New magnetic anisotropy," *Physical review*, vol. 102, no. 5, p. 1413, 1956.

[14] C. Müller, D. Golberg, A. Leonhardt, S. Hampel, and B. Büchner, "Growth studies, TEM and XRD investigations of iron-filled carbon nanotubes," *physica status solidi (a)*, vol. 203, no. 6, pp. 1064–1068, 2006.

[15] D. Golberg, M. Mitome, C. Müller, C. Tang, A. Leonhardt, and Y. Bando, "Atomic structures of iron-based single-crystalline nanowires crystallized inside multi-walled carbon nanotubes as revealed by analytical electron microscopy," *Acta materialia*, vol. 54, no. 9, pp. 2567–2576, 2006.

[16] X. Zhang, A. Cao, B. Wei, Y. Li, J. Wei, C. Xu, and D. Wu, "Rapid growth of well-aligned carbon nanotube arrays," *Chemical Physics Letters*, vol. 362, no. 3, pp. 285–290, 2002.

[17] A. Morelos-Gómez, F. López-Urías, E. Muñoz-Sandoval, C. L. Dennis, R. D. Shull, H. Terrones, and M. Terrones, "Controlling high coercivities of ferromagnetic nanowires encapsulated in carbon nanotubes," *Journal of Materials Chemistry*, vol. 20, no. 28, pp. 5906–5914, 2010.

[18] J. R. Davis, "Asm specialty handbook: nickel, cobalt, and their alloys," *ASM International, Member/Customer Service Center, Materials Park, OH 44073-0002, USA, 2000. 442*, 2000.

[19] `https://www.britannica.com/science/Bragg-law`.

[20] `https://encyclopedia2.thefreedictionary.com/x-ray+diffraction`.

[21] Z. Zhang, T. Zhou, M. Lu, A. W. C. Poh, and S. N. Piramanayagam, *Cobalt Nanomaterials: Synthesis and Characterization*. Wiley-VCH Verlag GmbH & Co. KGaA, 2007.

[22] N. Tanaka, *Electron Nano-Imaging: Basics of Imaging and Diffraction for TEM and STEM*. Springer, 2017.

[23] D. B. Williams and C. B. Carter, *Transmission electron microscopy: a textbook for materials science*, vol. III. Springer Science and Business Media, 2009.

[24] M. McElfresh, "Fundamentals of magnetism and magnetic measurements featuring quantum designs magnetic property measurement system," *Quantum Design*, vol. 11578, p. 132, 1994.

[25] E. Mittemeijer, "Fundamentals of materials science: The microstructure-property relationship using metals as model systems," *Heidelberg: Springer-Verlag*, 2010.

[26] S. Iijima and T. Ichihashi, "Single-shell carbon nanotubes of 1-nm diameter," *Nature*, vol. 363, no. 6430, pp. 603–605, 1993.

[27] S. Iijima, "Helical microtubules of graphitic carbon," *Nature*, vol. 354, no. 56, 1991.

[28] G. D. Nessim, "Properties, synthesis, and growth mechanisms of carbon nanotubes with special focus on thermal chemical vapor deposition," *Nanoscale*, vol. 2, no. 8, pp. 1306–1323, 2010.

[29] R. Saito, G. Dresselhaus, and M. S. Dresselhaus, *Physical properties of carbon nanotubes*. World scientific, 1998.

[30] P. Kappen, A. Rider, P. Pigram, and N. Brack, "Long-term stability of metallic iron inside carbon nanotubes," *The Journal of Physical Chemistry C*, vol. 115, no. 43, pp. 21083–21087, 2011.

[31] A. Leonhardt, S. Hampel, C. Mueller, I. Moench, R. Koseva, M. Ritschel, D. Elefant, K. Biedermann, and B. Buechner, "Synthesis, properties, and applications of ferromagnetic-filled carbon nanotubes," *Chemical vapor deposition*, vol. 12, no. 6, pp. 380–387, 2006.

[32] S. Hampel, A. Leonhardt, D. Selbmann, K. Biedermann, D. Elefant, C. Müller, T. Gemming, and B. Büchner, "Growth and characterization of filled carbon nanotubes with ferromagnetic properties," *Carbon*, vol. 44, no. 11, pp. 2316–2322, 2006.

[33] C. Prados, P. Crespo, J. M. González, A. Hernando, J. F. Marco, R. Gancedo, N. Grobert, M. Terrones, R. M. Walton, and H. W. Kroto, "Hysteresis shift in Fe-filled carbon nanotubes due to γ-Fe," *Physical Review B*, vol. 65, no. 11, p. 113405, 2002.

[34] N. Grobert, M. Mayne, M. Terrones, J. Sloan, R. Dunin-Borkowski, R. Kamalakaran, T. Seeger, H. Terrones, M. Rühle, D. Walton, H. Kroto, and J. Hutchison, "Alloy nanowires: Invar inside carbon nanotubes," *Chemical Communications*, no. 5, pp. 471–472, 2001.

[35] S. Karmakar, S. M. Sharma, M. D. Mukadam, S. M. Yusuf, and A. K. Sood, "Magnetic behavior of iron-filled multiwalled carbon nanotubes," *Journal of Applied Physics*, vol. 97, no. 5, p. 054306, 2005.

[36] N. Grobert, W. Hsu, Y. Zhu, J. Hare, H. Kroto, D. Walton, M. Terrones, H. Terrones, P. Redlich, M. Rühle, *et al.*, "Enhanced magnetic coercivities in Fe nanowires," *Applied Physics Letters*, vol. 75, no. 21, pp. 3363–3365, 1999.

[37] A. Leonhardt, M. Ritschel, D. Elefant, N. Mattern, K. Biedermann, S. Hampel, C. Müller, T. Gemming, and B. Büchner, "Enhanced magnetism in Fe-filled carbon nanotubes produced by pyrolysis of ferrocene," *Journal of applied physics*, vol. 98, no. 7, p. 074315, 2005.

[38] R. Lv, A. Cao, F. Kang, W. Wang, J. Wei, J. Gu, K. Wang, and D. Wu, "Single-crystalline permalloy nanowires in carbon nanotubes: Enhanced encapsulation and magnetization," *The Journal of Physical Chemistry C*, vol. 111, no. 30, pp. 11475–11479, 2007.

[39] A. Wu, J. Gao, X. Chen, X. Yang, and H. Yang, "Magnetic properties of carbon-encapsulated Fe-Ni alloy nanocomposites," *Journal of Alloys and Compounds*, vol. 583, pp. 55–59, 2014.

[40] H. Ucar, J. J. Ipus, D. Laughlin, and M. McHenry, "Tuning the curie temperature in γ-FeNi nanoparticles for magnetocaloric applications by controlling the oxidation kinetics," *Journal of Applied Physics*, vol. 113, no. 17, p. 17A918, 2013.

[41] P. Manna and S. Yusuf, "Two interface effects: Exchange bias and magnetic proximity," *Physics Reports*, vol. 535, no. 2, pp. 61–99, 2014.

[42] C. Prados, P. Crespo, J. González, A. Hernando, J. Marco, R. Gancedo, N. Grobert, M. Terrones, R. Walton, and H. Kroto, "Magnetic and hysteretic properties of Fe-filled nanotubes," *IEEE transactions on magnetics*, vol. 37, no. 4, pp. 2117–2119, 2001.

[43] J. Marco, J. Gancedo, A. Hernando, P. Crespo, C. Prados, J. Gonzalez, N. Grobert, M. Terrones, D. Walton, and H. Kroto, "Mössbauer study of iron-containing carbon nanotubes," *Hyperfine Interactions*, vol. 139, no. 1, pp. 535–542, 2002.

[44] T. Ruskov, I. Spirov, M. Ritschel, C. Müller, A. Leonhardt, and R. Ruskov, "Mössbauer morphological analysis of Fe-filled multiwalled carbon nanotube samples," *Journal of applied physics*, vol. 100, no. 8, p. 084326, 2006.

[45] L. Kaufman, E. Clougherty, and R. Weiss, "The lattice stability of metals-III. iron," *Acta metallurgica*, vol. 11, no. 5, pp. 323–335, 1963.

[46] L. Cheng, A. Böttger, T. H. De Keijser, and E. Mittemeijer, "Lattice parameters of iron-carbon and iron-nitrogen martensites and austenites," *Scripta metallurgica et materialia*, vol. 24, no. 3, pp. 509–514, 1990.

[47] N. Ridley and H. Stuart, "Partial molar volumes from high-temperature lattice parameters of iron–carbon austenites," *Metal Science Journal*, vol. 4, no. 1, pp. 219–222, 1970.

[48] I. Lyubutin, K. Frolov, O. Anosova, V. Pokatilov, A. Okotrub, A. Kudashov, Y. V. Shubin, and L. Bulusheva, "Phase states and magnetic properties of iron nanoparticles in carbon nanotube channels," *Journal of Experimental and Theoretical Physics*, vol. 109, no. 2, pp. 254–261, 2009.

[49] H. Kim, M. J. Kaufman, W. M. Sigmund, D. Jacques, and R. Andrews, "Observation and formation mechanism of stable face-centered-cubic Fe nanorods in carbon nanotubes," *Journal of materials research*, vol. 18, no. 05, pp. 1104–1108, 2003.

[50] H. Kim, M. J. Kaufman, and W. M. Sigmund, "Phase transition of iron inside carbon nanotubes under electron irradiation," *Journal of materials research*, vol. 19, no. 06, pp. 1835–1839, 2004.

[51] V. Pecharsky, G. Samolyuk, V. Antropov, A. Pecharsky, and K. Gschneidner, "The effect of varying the crystal structure on the magnetism, electronic structure and thermodynamics in the gd 5 (si x ge 1- x) 4 system near x= 0.5," *Journal of Solid State Chemistry*, vol. 171, no. 1, pp. 57–68, 2003.

[52] V. K. Pecharsky and K. A. Gschneidner Jr, "Magnetocaloric effect and magnetic refrigeration," *Journal of Magnetism and Magnetic Materials*, vol. 200, no. 1, pp. 44–56, 1999.

[53] C. Zimm, A. Jastrab, A. Sternberg, V. Pecharsky, K. Gschneidner Jr, M. Osborne, and I. Anderson, "Description and performance of a near-room temperature magnetic refrigerator," in *Advances in cryogenic engineering*, pp. 1759–1766, Springer, 1998.

[54] V. Pecharsky, K. Gschneidner Jr, A. Pecharsky, and A. Tishin, "Thermodynamics of the magnetocaloric effect," *Physical review B*, vol. 64, no. 14, p. 144406, 2001.

[55] M. Foldeaki, R. Chahine, B. Gopal, T. Bose, X. Liu, and J. Barclay, "Effect of sample preparation on the magnetic and magnetocaloric properties of amorphous gd 70 ni 30," *Journal of applied physics*, vol. 83, no. 5, pp. 2727–2734, 1998.

[56] D. Golberg, C. Gu, Y. Bando, M. Mitome, and C. Tang, "Peculiarities of Fe-Ni alloy crystallization and stability inside C nanotubes as derived through electron microscopy," *Acta materialia*, vol. 53, no. 5, pp. 1583–1593, 2005.

[57] M. Daenen, R. De Fouw, B. Hamers, P. Janssen, K. Schouteden, and M. Veld, "The wondrous world of carbon nanotubes," *Eindhoven University of Technology*, vol. 27, 2003.

[58] Y. Saito, T. Yoshikawa, S. Bandow, M. Tomita, and T. Hayashi, "Interlayer spacings in carbon nanotubes," *Physical Review B*, vol. 48, no. 3, p. 1907, 1993.

[59] M. Winterer, *Nanocrystalline ceramics: synthesis and structure*, vol. 53. Springer Science & Business Media, 2013.

[60] T. Ebbesen and A. P M, "Large-scale synthesis of carbon," *Nature*, vol. 358, p. 16, 1992.

[61] A. Thess, R. Lee, P. Nikolaev, H. Dai, P. Petit, J. Robert, C. Xu, Y. H. Lee, S. G. Kim, A. G. Rinzler, *et al.*, "Crystalline ropes of metallic carbon nanotubes," *Science*, pp. 483–487, 1996.

[62] M. José-Yacamán, M. Miki-Yoshida, L. Rendon, and J. Santiesteban, "Catalytic growth of carbon microtubules with fullerene structure," *Applied physics letters*, vol. 62, no. 6, pp. 657–659, 1993.

[63] S. Amelinckx, X. B. Zhang, D. Bernaerts, X. F. Zhang, V. Ivanov, and J. B. Nagy, "A formation mechanism for catalytically grown helix-shaped graphite nanotubes," *Science*, vol. 265, p. 29, 1994.

[64] A. Leonhardt, M. Ritschel, R. Kozhuharova, A. Graff, T. Mühl, R. Huhle, I. Mönch, D. Elefant, and C. Schneider, "Synthesis and properties of filled carbon nanotubes," *Diamond and related materials*, vol. 12, no. 3, pp. 790–793, 2003.

[65] H. Terrones, F. López-Urías, E. Munoz-Sandoval, J. Rodríguez-Manzo, A. Zamudio, A. Elías, and M. Terrones, "Magnetism in Fe-based and carbon nanostructures: theory and applications," *Solid state sciences*, vol. 8, no. 3, pp. 303–320, 2006.

[66] F. Dillon, A. Bajpai, A. Koos, S. Downes, Z. Aslam, and N. Grobert, "Tuning the magnetic properties of iron-filled carbon nanotubes," *Carbon*, vol. 50, no. 10, pp. 3674–3681, 2012.

[67] J. Cheng, X. Zou, G. Zhu, M. Wang, Y. Su, G. Yang, and X. Lü, "Synthesis of iron-filled carbon nanotubes with a great excess of ferrocene and their magnetic properties," *Solid State Communications*, vol. 149, no. 39, pp. 1619–1622, 2009.

[68] R. Lv, F. Kang, D. Cai, C. Wang, J. Gu, K. Wang, and D. Wu, "Long continuous FeNi nanowires inside carbon nanotubes: Synthesis, property and application," *Journal of Physics and Chemistry of Solids*, vol. 69, no. 5, pp. 1213–1217, 2008.

[69] B. Elliott, J. Host, V. Dravid, M. Teng, and J. Hwang, "A descriptive model linking possible formation mechanisms for graphite-encapsulated nanocrystals to processing parameters," *Journal of materials research*, vol. 12, no. 12, pp. 3328–3344, 1997.

[70] R. Wagner and W. Ellis, "Vapor-liquid-solid mechanism of single crystal growth," *Applied Physics Letters*, vol. 4, no. 5, pp. 89–90, 1964.

[71] A. R. Harutyunyan, O. A. Kuznetsov, C. J. Brooks, E. Mora, and G. Chen, "Thermodynamics behind carbon nanotube growth via endothermic catalytic decomposition reaction," *ACS nano*, vol. 3, no. 2, pp. 379–385, 2009.

[72] A. Moisala, A. G. Nasibulin, and E. I. Kauppinen, "The role of metal nanoparticles in the catalytic production of single-walled carbon nanotubesa review," *Journal of Physics: condensed matter*, vol. 15, no. 42, p. S3011, 2003.

[73] M. Kumar and Y. Ando, "Chemical vapor deposition of carbon nanotubes: a review on growth mechanism and mass production," *Journal of nanoscience and nanotechnology*, vol. 10, no. 6, pp. 3739–3758, 2010.

[74] R. Baker, "The formation of filamentous carbon," *Chemistry and physics of carbon*, vol. 14, pp. 83–164, 1978.

[75] S. Bellucci and A. Malesevic, "Physics of carbon nanostructures, in physical properties of ceramic and carbon nanoscale structures," *Lecture Notes in Nanoscale Science and Technology: Springer*, vol. 11, pp. 155–194, 2011.

[76] M. H. Rümmeli, A. Bachmatiuk, F. Börrnert, F. Schäffel, I. Ibrahim, K. Cendrowski, G. Simha-Martynkova, D. Plachá, E. Borowiak-Palen, G. Cuniberti, *et al.*, "Synthesis of carbon nanotubes with and without catalyst particles," *Nanoscale research letters*, vol. 6, no. 1, p. 303, 2011.

[77] F. S. Boi, G. Mountjoy, R. M. Wilson, Z. Luklinska, L. J. Sawiak, and M. Baxendale, "Multiwall carbon nanotubes continuously filled with micrometre-length ferromagnetic α-Fe nanowires," *Carbon*, vol. 64, pp. 351–358, 2013.

[78] N. Chechenin, P. Chernykh, E. Vorobyeva, M. Dutka, D. Vainshtein, and J. T. M. De Hosson, "Structure phases of Fe nanoparticles in vertically aligned multi-walled carbon nanotubes," *Journal of Surface Investigation. X-ray, Synchrotron and Neutron Techniques*, vol. 9, no. 5, pp. 1044–1055, 2015.

[79] T. Peci and M. Baxendale, "Length and α-Fe content control of self-organised ferromagnetic nanowires encapsulated by multiwalled carbon nanotubes by low flow-rate cvd," *Carbon*, vol. 98, pp. 519–525, 2016.

[80] S. Fan, M. G. Chapline, N. R. Franklin, T. W. Tombler, A. M. Cassell, and H. Dai, "Self-oriented regular arrays of carbon nanotubes and their field emission properties," *Science*, vol. 283, no. 5401, pp. 512–514, 1999.

[81] J. Cambedouzou, P. Landois, S. Rouzière, M. Pinault, C. Mocuta, L. Hennet, D. Thiaudière, M. Mayne-L'Hermite, and P. Launois, "Anomalous thermal expansion of γ-iron nanocrystals inside multiwalled carbon nanotubes," *Physical Review B*, vol. 88, no. 8, p. 081402, 2013.

[82] X. Gui, J. Wei, K. Wang, W. Wang, R. Lv, J. Chang, F. Kang, J. Gu, and D. Wu, "Improved filling rate and enhanced magnetic properties of Fe-filled carbon nanotubes by annealing and magnetic separation," *Materials Research Bulletin*, vol. 43, no. 12, pp. 3441–3446, 2008.

[83] V. Heresanu, C. Castro, J. Cambedouzou, M. Pinault, O. Stephan, C. Reynaud, M. Mayne-L'Hermite, and P. Launois, "Nature of the catalyst particles in CCVD synthesis of multiwalled carbon nanotubes revealed by the cooling step study," *The Journal of Physical Chemistry C*, vol. 112, no. 19, pp. 7371–7378, 2008.

[84] H. Bhadeshia and R. Honeycombe, *Steels: microstructure and properties, Chapter 1 - Iron and its Interstitial Solid Solutions*. Butterworth-Heinemann, 2017.

[85] M. Onink, C. Brakman, F. Tichelaar, E. Mittemeijer, S. Van der Zwaag, J. Root, and N. Konyer, "The lattice parameters of austenite and ferrite in Fe-C alloys as functions of carbon concentration and temperature," *Scripta metallurgica et materialia*, vol. 29, no. 8, pp. 1011–1016, 1993.

[86] W. Pepperhoff and M. Acet, *Constitution and Magnetism of Iron and its Alloys*. Springer Science & Business Media, 2013.

[87] A. Kirilyuk, J. Giergiel, J. Shen, M. Straub, and J. Kirschner, "Growth of stabilized γ-Fe films and their magnetic properties," *Physical Review B*, vol. 54, no. 2, p. 1050, 1996.

[88] J. Heremans, C. Olk, and D. Morelli, "Magnetic susceptibility of carbon structures," *Physical Review B*, vol. 49, no. 21, p. 15122, 1994.

[89] T. Mühl, D. Elefant, A. Graff, R. Kozhuharova, A. Leonhardt, I. Mönch, M. Ritschel, P. Simon, S. Groudeva-Zotova, and C. Schneider, "Magnetic properties of aligned Fe-filled carbon nanotubes," *Journal of applied physics*, vol. 93, no. 10, pp. 7894–7896, 2003.

[90] M. Lutz, U. Weissker, F. Wolny, C. Müller, M. Löffler, T. Mühl, A. Leonhardt, B. Büchner, and R. Klingeler, "Magnetic properties of α-Fe and Fe_3C nanowires," in *Journal of Physics: Conference Series*, vol. 200, p. 072062, IOP Publishing, 2010.

[91] U. Weissker, M. Löffler, F. Wolny, M. U. Lutz, N. Scheerbaum, R. Klingeler, T. Gemming, T. Mühl, A. Leonhardt, and B. Büchner, "Perpendicular magnetization of long iron carbide nanowires inside carbon nanotubes due to magnetocrystalline anisotropy," *Journal of Applied Physics*, vol. 106, no. 5, p. 054909, 2009.

[92] V. Likodimos, S. Glenis, N. Guskos, and C. Lin, "Magnetic and electronic properties of multiwall carbon nanotubes," *Physical Review B*, vol. 68, no. 4, p. 045417, 2003.

[93] R. Lv, S. Tsuge, X. Gui, K. Takai, F. Kang, T. Enoki, J. Wei, J. Gu, K. Wang, and D. Wu, "In situ synthesis and magnetic anisotropy of ferromagnetic buckypaper," *Carbon*, vol. 47, no. 4, pp. 1141–1145, 2009.

[94] R. Kumari, L. Krishnia, V. Kumar, S. Singh, H. Singh, R. Kotnala, R. Juluri, U. Bhatta, P. Satyam, B. S. Yadav, *et al.*, "Fe_3C-filled carbon nanotubes: permanent cylindrical nanomagnets possessing exotic magnetic properties," *Nanoscale*, vol. 8, no. 7, pp. 4299–4310, 2016.

[95] J. Guo, J. Liu, M. Lan, Y. Hu, S. Wang, J. Wen, Y. He, F. Gao, X. Zhang, S. Zhang, *et al.*, "Observation of large coercivities in radial carbon nanotube structures filled with Fe_3C and FeCo single-crystals by viscous boundary layer pyrolysis of ferrocene and cobaltocene," *RSC Advances*, vol. 7, no. 8, pp. 4753–4758, 2017.

[96] M. Kiwi, "Exchange bias theory," *Journal of Magnetism and Magnetic Materials*, vol. 234, no. 3, pp. 584–595, 2001.

[97] J. Nogués, J. Sort, V. Langlais, V. Skumryev, S. Surinach, J. Muñoz, and M. Baró, "Exchange bias in nanostructures," *Physics Reports*, vol. 422, no. 3, pp. 65–117, 2005.

[98] M. P. Fernández-García, P. Gorria, J. A. Blanco, A. B. Fuertes, M. Sevilla, R. Boada, J. Chaboy, D. Schmool, and J.-M. Grenèche, "Microstructure and magnetism of nanoparticles with γ-Fe core surrounded by α-Fe and iron oxide shells," *Physical Review B*, vol. 81, no. 9, p. 094418, 2010.

[99] W. Keune, R. Halbauer, U. Gonser, J. Lauer, and D. Williamson, "Antiferromagnetism of fcc Fe thin films," *Journal of Magnetism and Magnetic Materials*, vol. 6, pp. 192–195, 1977.

[100] C. Wang, B. Klein, and H. Krakauer, "Theory of magnetic and structural ordering in iron," *Physical review letters*, vol. 54, no. 16, p. 1852, 1985.

[101] F. Cardarelli, *Materials handbook: a concise desktop reference*. Springer Science & Business Media, 2008.

[102] H. Ucar, J. J. Ipus, V. Franco, M. McHenry, and D. Laughlin, "Overview of amorphous and nanocrystalline magnetocaloric materials operating near room temperature," *Jom*, vol. 64, no. 7, pp. 782–788, 2012.

[103] H. Ucar, M. Craven, D. Laughlin, and M. McHenry, "Effect of Mo addition on structure and magnetocaloric effect in γ-FeNi nanocrystals," *Journal of Electronic Materials*, vol. 43, no. 1, p. 137, 2014.

[104] K. J. Miller, M. Sofman, K. McNerny, and M. E. McHenry, "Metastable γ-FeNi nanostructures with tunable curie temperature," *Journal of Applied Physics*, vol. 107, no. 9, p. 09A305, 2010.

[105] K. McNerny, Y. Kim, D. E. Laughlin, and M. E. McHenry, "Chemical synthesis of monodisperse γ-Fe-Ni magnetic nanoparticles with tunable curie temperatures for self-regulated hyperthermia," *Journal of Applied Physics*, vol. 107, no. 9, p. 09A312, 2010.

[106] W. C. Leslie and E. Hornbogen, "Physical metallurgy of steels-chapter 17," 1981.

[107] F. Li, Z. Zhao, X. Diao, and D. Xue, "A comparative study of the structural and magnetic properties of γ-$Fe_{1-x}Ni_x$ alloys and their nitrides γ'-$(Fe_{1-x}Ni_x)_4N$," *phys. stat. sol.(a)*, vol. 174, p. 255, 1999.

[108] G. Abellán, H. Prima-García, and E. Coronado, "Graphene enhances the magnetoresistance of $FeNi_3$ nanoparticles in hierarchical $FeNi_3$-graphene nanocomposites," *Journal of Materials Chemistry C*, vol. 4, no. 11, pp. 2252–2258, 2016.

[109] R. Lv, F. Kang, J. Gu, K. Wang, and D. Wu, "Synthesis, field emission and microwave absorption of carbon nanotubes filled with ferromagnetic nanowires," *Science China Technological Sciences*, vol. 53, no. 6, pp. 1453–1459, 2010.

[110] X. Liu, B. Li, D. Geng, W. Cui, F. Yang, Z. Xie, D. Kang, and Z. Zhang, "(Fe, Ni)/C nanocapsules for electromagnetic-wave-absorber in the whole Ku-band," *Carbon*, vol. 47, no. 2, pp. 470–474, 2009.

[111] T. Sohmura and F. Fujita, "The effect of hydrogen on the magnetic properties of Fe-Ni base invar alloys," *Journal of Physics F: Metal Physics*, vol. 10, no. 4, p. 743, 1980.

[112] C. Suryanarayana and M. G. Norton, *X-ray diffraction: a practical approach*. Springer Science & Business Media, 2013.

[113] H. M. Rietveld, "A profile refinement method for nuclear and magnetic structures," *Journal of Applied Crystallography*, vol. 2, pp. 65–71, Jun 1969.

[114] A. Larson and R. V. Dreele, *General Structure Analysis System (GSAS)*. Los Alamos National Laboratory Report, LAUR, 2004.

[115] B. H. Toby, "EXPGUI, a graphical user interface for GSAS," *Journal of Applied Crystallography*, vol. 34, no. 2, pp. 210–213, 2001.

[116] G. Will, *Powder diffraction: The Rietveld method and the two stage method to determine and refine crystal structures from powder diffraction data*. Springer Science & Business Media, 2006.

[117] R. F. Egerton, *Physical principles of electron microscopy*. Springer, 2016.

[118] P. Hawkes and J. C. Spence, *Science of microscopy*. Springer Science & Business Media, 2008.

[119] J. Goldstein, D. E. Newbury, P. Echlin, D. C. Joy, A. D. Romig Jr, C. E. Lyman, C. Fiori, and E. Lifshin, *Scanning electron microscopy and X-ray microanalysis: a text for biologists, materials scientists, and geologists*. Springer Science & Business Media, 2012.

[120] E. Abe, "Atomic-scale characterization of nanostructured metallic materials by haadf/z-contrast stem," *Materials Transactions*, vol. 44, no. 10, pp. 2035–2041, 2003.

[121] A. Genc, L. Kovarik, M. Gu, H. Cheng, P. Plachinda, L. Pullan, B. Freitag, and C. Wang, "Xeds stem tomography for 3d chemical characterization of nanoscale particles," *Ultramicroscopy*, vol. 131, pp. 24–32, 2013.

[122] M. Lin, H. R. Tan, J. P. Y. Tan, C. Boothroyd, Y. L. Foo, and C. B. He, "Transmission electron microscope tomography of nanostructured materials," *Journal of Nanoengineering and Nanomanufacturing*, vol. 1, no. 3, pp. 257–264, 2011.

[123] R. Fagaly, "Superconducting quantum interference device instruments and applications," *Review of scientific instruments*, vol. 77, no. 10, p. 101101, 2006.

[124] R. Sen, A. Govindaraj, and C. Rao, "Carbon nanotubes by the metallocene route," *Chemical Physics Letters*, vol. 267, no. 3-4, pp. 276–280, 1997.

[125] C. Rao and R. Sen, "Large aligned-nanotube bundles from ferrocene pyrolysis," *Chemical Communications*, no. 15, pp. 1525–1526, 1998.

[126] A. Cao, X. Zhang, J. Wei, Y. Li, C. Xu, J. Liang, D. Wu, and B. Wei, "Macroscopic three-dimensional arrays of Fe nanoparticles supported in aligned carbon nanotubes," *The Journal of Physical Chemistry B*, vol. 105, no. 48, pp. 11937–11940, 2001.

[127] W. Wang, K. Wang, R. Lv, J. Wei, X. Zhang, F. Kang, J. Chang, Q. Shu, Y. Wang, and D. Wu, "Synthesis of Fe-filled thin-walled carbon nanotubes with high filling ratio by using dichlorobenzene as precursor," *Carbon*, vol. 45, no. 5, pp. 1127–1129, 2007.

[128] K. Kuwana and K. Saito, "Modeling cvd synthesis of carbon nanotubes: Nanoparticle formation from ferrocene," *Carbon*, vol. 43, no. 10, pp. 2088–2095, 2005.

[129] A. K. Schaper, H. Hou, A. Greiner, and F. Phillipp, "The role of iron carbide in multiwalled carbon nanotube growth," *Journal of Catalysis*, vol. 222, no. 1, pp. 250–254, 2004.

[130] M. A. Ermakova, D. Y. Ermakov, A. L. Chuvilin, and G. G. Kuvshinov, "Decomposition of methane over iron catalysts at the range of moderate temperatures: the influence of structure of the catalytic systems and the reaction conditions on the yield of carbon and morphology of carbon filaments," *Journal of catalysis*, vol. 201, no. 2, pp. 183–197, 2001.

[131] S. Groudeva-Zotova, R. Kozhuharova, D. Elefant, T. Mühl, C. Schneider, and I. Mönch, "Phase composition and magnetic characteristics of Fe-filled multi-walled carbon nanotubes," *Journal of magnetism and magnetic materials*, vol. 306, no. 1, pp. 40–50, 2006.

[132] O. A. Louchev, H. Kanda, A. Rosén, and K. Bolton, "Thermal physics in carbon nanotube growth kinetics," *The Journal of chemical physics*, vol. 121, no. 1, pp. 446–456, 2004.

[133] W. Ren, F. Li, and H.-M. Cheng, "Evidence for, and an understanding of, the initial nucleation of carbon nanotubes produced by a floating catalyst method," *The Journal of Physical Chemistry B*, vol. 110, no. 34, pp. 16941–16946, 2006.

[134] J.-Y. Raty, F. Gygi, and G. Galli, "Growth of carbon nanotubes on metal nanoparticles: a microscopic mechanism from ab initio molecular dynamics simulations," *Physical review letters*, vol. 95, no. 9, p. 096103, 2005.

[135] S. Helveg, C. López-Cartes, J. Sehested, P. L. Hansen, *et al.*, "Atomic-scale imaging of carbon nanofibre growth," *Nature*, vol. 427, no. 6973, p. 426, 2004.

[136] A. Schneider, "Iron layer formation during cementite decomposition in carburising atmospheres," *Corrosion science*, vol. 44, no. 10, pp. 2353–2365, 2002.

[137] H. Aurich, A. Baumgartner, F. Freitag, A. Eichler, J. Trbovic, and C. Schönenberger, "Permalloy-based carbon nanotube spin-valve," *Applied physics letters*, vol. 97, no. 15, p. 153116, 2010.

[138] J. Wang, Z. Dong, J. Huang, J. Li, X. Jin, J. Niu, J. Sun, J. Jin, and J. Ma, "Filling carbon nanotubes with Ni-Fe alloys via methylbenzene-oriented constant current electrodeposition for hydrazine electrocatalysis," *Applied Surface Science*, vol. 270, pp. 128–132, 2013.

[139] R. Lv, F. Kang, W. Wang, J. Wei, J. Gu, K. Wang, and D. Wu, "Effect of using chlorine-containing precursors in the synthesis of FeNi-filled carbon nanotubes," *Carbon*, vol. 45, no. 7, pp. 1433–1438, 2007.

[140] H. Kim and W. Sigmund, "Iron nanoparticles in carbon nanotubes at various temperatures," *Journal of crystal growth*, vol. 276, no. 3, pp. 594–605, 2005.

[141] L. Sun, F. Banhart, A. Krasheninnikov, J. Rodriguez-Manzo, M. Terrones, and P. Ajayan, "Carbon nanotubes as high-pressure cylinders and nanoextruders," *Science*, vol. 312, no. 5777, pp. 1199–1202, 2006.

[142] F. Banhart, J. Li, and A. Krasheninnikov, "Carbon nanotubes under electron irradiation: stability of the tubes and their action as pipes for atom transport," *Physical Review B*, vol. 71, no. 24, p. 241408, 2005.

[143] Y. Bagaryatski, "Wierojatnyj machanizm raspada martiensita," *Dokl. Acad. Nauk. SSSR*, vol. 73, 1950.

[144] C. D. Tebble S, *Magnetic materials*. Wiley New York, 1966.

[145] J. Häglund, G. Grimvall, and T. Jarlborg, "Electronic structure, x-ray photoemission spectra, and transport properties of Fe_3C (cementite)," *Physical Review B*, vol. 44, no. 7, p. 2914, 1991.

[146] V. Z. Mordkovich, D. Kharitonov, I. Maslov, and E. Mitberg, "Ni-Fe competition in the catalytic growth of carbon nanotubes," *MRS Online Proceedings Library Archive*, vol. 963, 2006.

[147] J. A. Rodríguez-Manzo, M. Terrones, H. Terrones, H. W. Kroto, L. Sun, and F. Banhart, "In situ nucleation of carbon nanotubes by the injection of carbon atoms into metal particles," *Nature nanotechnology*, vol. 2, no. 5, pp. 307–311, 2007.

[148] M. Kumar, *Carbon nanotube synthesis and growth mechanism*. InTech, 2011.

[149] J.-L. Maurice, D. Pribat, Z. He, G. Patriarche, and C. Cojocaru, "Catalyst faceting during graphene layer crystallization in the course of carbon nanofiber growth," *Carbon*, vol. 79, pp. 93–102, 2014.

[150] K. K. Koziol, T. Kasama, R. E. Dunin-Borkowski, P. Barpanda, and A. H. Windle, "Electron holography of ferromagnetic nanoparticles encapsulated in three-dimensional arrays of aligned carbon nanotubes," *MRS Online Proceedings Library Archive*, vol. 962, 2006.